Mechanisms for Nanoparticle Synthesis and Charging in Nonthermal Plasmas

A THESIS
SUBMITTED TO THE FACULTY OF THE GRADUATE SCHOOL
OF THE UNIVERSITY OF MINNESOTA
BY

Romain Le Picard

IN PARTIAL FULFILLMENT OF THE REQUIREMENTS
FOR THE DEGREE OF
DOCTOR OF PHILOSOPHY

Steven L. Girshick

July, 2016

© Romain Le Picard 2016
ALL RIGHTS RESERVED

Acknowledgments

I would like to express my sincere gratitude to my adviser Prof. Steven L. Girshick for giving me the opportunity to work under his guidance. His continuous support and patience have been very appreciated. I am really thankful to the opportunity I had to present my work in many conferences. I would also like to thank Dr. Bruggeman, Dr. Ernie, and Dr. Hogan for serving as my committee members. This thesis has been supported by the National Science Foundation and the Department of Energy.

My main research project was done in collaboration with Prof. Mark J. Kushner at University of Michigan. I would like to thank him for his continuous guidance and consistency while working on the HPEM. I also want to thank Dr. Aram H. Markosyan and Dr. Sang-Heon Song for their great contribution to the project. I would like to thank Dr. Meenakshi Mamunuru and Dr. Yukinori Sakiyama at Lam Research Corporation for the discussions on particle charging. I want to thank David H. Porter at Minnesota Supercomputing Institute for his great help on developing a post-processing tool to analyze the data.

I would like to thank Dr. Boufendi at GREMI (Orléans, France) for giving me the opportunity to visit his laboratory to conduct experiments on dusty plasmas. I would also like to thank Dr. Roca i Cabarrocas at Ecole Polytechnique (Paris, France) for having me in his group to work on particle formation and growth in plasmas.

I had the chance to meet amazing people when I first came to Minneapolis as a visiting student. I want to thank Maki Kii, Mathieu Pythoud, and Annie Sukowatey for their help and all great memories, as they contributed to my decision to stay in the US. I want to thank Pulkit Agarwal for his friendship and his unforgettable help and support since I came to Minneapolis. I cannot be more thankful to him and his wife Esha for welcoming me at their wedding in India. I want to thank my past office mates and

friends, Vijay, Venkat, Ching-Sung, Xuewang, Biswa, Parth, Vivek, and Arjun for their help, support, and friendship during good and difficult times. Special thanks are due to Ana Lucia Prieto–*ojalá*. I would like to thank Elodie, Mohamed, Rami, Cristina, and Céline for the pleasure I had to meet them every time I went back to France. I also want to thank my *Balgencienne* friend Jeanne for her support from Louisiana. I want to thank Carole Destribats for endless conversations that motivated me until the very end of this PhD.

Finally, I want to thank my parents Isabelle and Beaudoin for believing in me and motivating me despite the long distance. I want to thank Audrey, Guillaume, and Chloé for being such great siblings.

Dedication

To my grandfather, Claude Clémensat

Abstract

Nanoparticle formation, charging, and transport in plasmas have been extensively studied due to increasing interest. In the semiconductor industry, dust particles are considered as defects and are therefore unwanted as they can damage electronic devices during plasma etching or chemical vapor deposition. Potential applications are emerging, including biomedicine or photovoltaics, and require unique particle size and material properties. With the advancement of new technologies, along with a better understanding of particle formation, it is possible to experimentally tailor particle properties as small as 1 nm in diameter. The aim of this thesis is to contribute to the understanding of the mechanisms underlying the formation of nanoparticles in plasmas.

A two-dimensional model is developed to self-consistently examine nanoparticle formation, growth, charging, and transport in low-pressure, capacitively-coupled RF flowing plasmas. The experimental set-up modeled is a narrow quartz tube in which a gas mixture of Ar/He/SiH_4 flows. The silane dissociation is mostly produced by electron impact due to highly energetic electrons. The nanoparticle cloud is coupled to the plasma. The spatial evolution of the particle size distribution and charge distribution is presented. We show that nanoparticles are mostly negatively charged and pushed along the centerline of the discharge due the ambipolar electric field. However, particles are not trapped in the axial direction, which allows nanoparticles to grow as they flow through the tube. The model predicts the possibility of producing crystalline nanoparticles due to exothermic reactions (e.g., electron-ion recombination and hydrogen reactions) on nanoparticle surfaces.

The charging of nanoparticles in plasmas plays a significant role in their growth mechanisms and transport. In a typical parallel plate plasma system, nanoparticles get negatively charged due to collisions with electrons and are trapped at the center of the discharge due to the ambipolar electric field. At small nanoparticle sizes (< 10 nm), the number of electrons that can coexist on a single particle is limited− referred to as particle charge limit. We studied the effect of particle charge limits on charge distributions in low-pressure nonthermal plasmas, by developing an analytical expression for the charge distribution and comparing it with a stochastic charging model.

Particle charging plays a significant role in particle transport since charged particles respond to the electric field. Under typical plasma-enhanced chemical vapor deposition conditions, a certain fraction of particles can be neutral or positive and escape the plasma and deposit on the wafer. To better understand and control particle deposition, we studied the effects of ion collisionality with the background neutral gas, electron emission processes, electronegativity, and charge limit on charge distributions.

Tailoring particle size and flux to a substrate is possible while using a pulsed plasma. Because particles are mostly negatively charged, they can be accelerated to the substrate when applying a positive DC bias when the plasma is OFF. Silicon particle formation, growth, and transport are discussed for the case of a parallel-plate capacitively-coupled RF pulsed plasma in H_2/SiH_4. The transport of such particles in the afterglow is discussed, based on preliminary work exploring system behavior during the first cycle of such a pulsed plasma.

Contents

Acknowledgments **i**

Dedication **iii**

Abstract **iv**

List of Tables **x**

List of Figures **xi**

Nomenclature **xviii**

1 Introduction **1**

1.1 General Introduction 1

1.2 Silicon Nanoparticle Synthesis in Plasmas 3

1.3 Numerical Plasma Modeling 4

1.4 Motivation 6

1.5 Content of this Thesis 8

2 Governing Equations of Dusty Plasmas **10**

2.1 The Boltzmann Equation 10

2.2 The Fluid Model 12

2.3 Maxwell's Equations and Poisson's Equation 13

2.4 Nanoparticle Growth Mechanisms 14

2.4.1 Nanoparticle Size Distribution 14

2.4.2 Aerosol Sectional Model 15

2.4.3 Coagulation 17
2.4.4 Surface Growth 19
2.5 Nanoparticle Charging 20
2.5.1 Charging Mechanisms 20
2.5.2 Particle Charge Distributions 21

3 Synthesis of Silicon Nanoparticles in Nonthermal Flowing Plasmas 23
3.1 Introduction 24
3.2 Description of The Model 26
3.2.1 Hybrid Plasma Equipment Model (HPEM) 26
3.2.2 Aerosol Sectional Module 29
3.2.3 Plasma Chemical Kinetics 33
3.3 Computational Challenges 37
3.4 Particle Synthesis in RF Discharges: Base Case 38
3.4.1 Model Schematic 38
3.4.2 Plasma Properties 42
3.4.3 Plasma Chemical Kinetics 44
3.4.4 Nanoparticle Growth Mechanisms 49
3.5 Nanoparticle Temperature and Crystallization 55
3.6 Concluding Remarks 58

4 The Effect of Single-Particle Charge Limits on Charge Distributions in Dusty Plasmas 61
4.1 Introduction 62
4.2 Review of Single-Particle Charge Limits 63
4.3 Analytical Expression for Stationary Particle Charge Distribution Accounting for Existence of Charge Limits 65
4.4 Test of Validity of Analytical Expression 70
4.5 Effect of Electron Depletion 73
4.6 Effect of Ion Mass 77
4.7 Effect of Charge Limits on Temporal Evolution of Charge Distribution . 77
4.7.1 Effect of Charge Limits on Time Required to Reach Steady-State Charge Distribution 79

4.7.2 Effect of Charge Limits on Power Spectrum of Charge Fluctuations 79
4.8 Conclusion 81

5 Stochastic Charging: Non-Negatively Charged Dust in Cold Plasmas 84
5.1 Introduction 85
5.2 Particle Charging Mechanisms 86
5.2.1 Pressure Effect on Positive Ion Current to a Particle 87
5.2.2 Secondary Electron Emission 88
5.2.3 Photoemission 89
5.2.4 Single-Particle Charge Limits 90
5.3 Description of the Monte Carlo Charging Model 90
5.4 The Existence of Neutral and Positive Particles 91
5.4.1 Reduction in Particle Charge 91
5.4.2 Electron Emission Processes 97
5.5 Conclusion 103

6 Silicon Nanoparticle Transport to a Substrate in Hydrogen-Silane Pulsed Plasma Discharges 104
6.1 Introduction 105
6.2 Description of the Model 106
6.2.1 Plasma-Aerosol Code 106
6.2.2 Plasma Module 108
6.2.3 Aerosol Module 109
6.2.4 Chemistry Module 111
6.3 Charged Particle Transport in Pulsed Plasmas 112
6.3.1 Model Schematic 112
6.3.2 Plasma ON: Particle Growth and Transport 114
6.3.3 Plasma OFF: Particle Dynamics in the Afterglow 118
6.3.4 Particle Impact Energy on Substrate 122
6.4 Conclusion 124

7 Conclusion 127

References **131**

Appendix A. List of Integrals **145**

List of Tables

3.1 Species included in the plasma chemistry model 30

3.2 Nucleation reactions included in the model 31

3.3 Change in Gibb's free energy, ΔG (in kcal/mol) as computed at the G3sX(MP3)// M06-L/MG3S level of theory for each reagent at a partial pressure of 1 bar. The unimolecular reagents are assumed to be fully equilibrated (i.e., to be in the high-pressure limit). 35

5.1 Secondary electron emission coefficients for different bulk materials [1]. . 88

6.1 Hydrogen and silicon hydride species included in the chemistry model for silicon particle formation in H_2/SiH_4 plasmas. 111

6.2 Electron impact and hydrogen species reactions included in the chemistry model for silicon particle formation in H_2/SiH_4 plasmas. Reaction rate constants are expressed in the Arrhenius form: $AT^{\beta}\exp(-E_a/T)$. 112

6.3 Electron impact reactions, silicon hydride species reactions, and nucleation reactions included in the chemistry model for silicon particle formation in H_2/SiH_4 plasmas. Reaction rate constants are expressed in the Arrhenius form: $AT^{\beta}\exp(-E_a/T)$. 113

List of Figures

1.1 Sensitivity and tunable color capability of NC imaging in live animals.(a,b) Sensitivity and spectral comparison between NC-tagged and traditional protein transfected cancer cells [2] 2
1.2 Silicon nanoparticle synthesis has been achieved under atmospheric plasma conditions. (a) Schematic of a plasma reactor, (b) photo of a microplasma generated inside a quartz capillary, and (c) representative transmission electron microscopy images of the silicon nanoparticles synthesized in microplasma [3] 5
2.1 Comparison of electron energy distribution functions for pristine and dusty plasmas in argon [4] 11
2.2 Schematic of a sectional modal: nucleation occurs in the first section and particles grow to higher sections by coagulation and radical deposition on nanoparticle surfaces [5] 16
3.1 Schematic of the Hybrid Plasma Equipment Model (HPEM). Each module returns a set of variables that can be used by other modules [6]. . . 28
3.2 Schematics of the geometry used in our model. (a) Radius expanded by a factor of 4. (b) Actual geometry. 39
3.3 Plasma properties for the base case conditions ($Ar/He/SiH_4 = 50/4.75/0.25$, 1.5 Torr, 3 W, 50 sccm). (a) Densities of power deposition and Ar^+ source by electron impact, (b) electron temperature and electric potential. Log-scale plots have number of decades noted. 41

3.4 Charged particle densities for the base case conditions ($Ar/He/SiH_4$= 50/4.75/0.25, 1.5 Torr, 3 W, 50 sccm). (a) Electron and total negative ions, (b) total positive ions and total negative nanoparticles. Log-scale plots have number of decades noted. 43
3.5 Silicon hydride densities for the base case conditions ($Ar/He/SiH_4$ = 50/4.75/0.25, 1.5 Torr, 3 W, 50 sccm). (a) SiH_4 and SiH_3, (b) Si_2H_5 and SiH_2. Log-scale plots have number of decades noted. 45
3.6 Rate of SiH_4 conversion to products by electron impact and hydrogen abstraction reactions along the centerline. 46
3.7 Atomic and molecular hydrogen densities for the base case conditions ($Ar/He/SiH_4$= 50/4.75/0.25, 1.5 Torr, 3 W, 50 sccm). (a) H and H_2, (b) H^- and H^+. Log-scale plots have number of decades noted. 48
3.8 Nanoparticle growth mechanisms. (a) Nucleation rate and surface growth rate, (b) coagulation rate and total nanoparticle density. Log-scale plots have number of decades noted. 50
3.9 (a) Nucleation reaction rates for reactions involving $Si_2H_5^-$ species and (b) relative contribution of radical deposition on nanoparticle surfaces during surface growth. 52
3.10 Nanoparticle size distributions on the centerline of the reactor (r=0). (a) Nanoparticle size distribution (cm^{-3} nm^{-1}) over 4 decades as a function of distance from the inlet, and (b) size distribution at 7, 9, 11, 12 cm from the inlet. 53
3.11 Size distributions for negatively charged and neutral nanoparticles at 11 cm from the inlet on the centerline. 54
3.12 Temperatures for the base case conditions: (left) Gas temperature (325 K - 445 K) and (right) internal temperature (325 K - 866 K) for 2-nm diameter nanoparticles. 57
3.13 Particle temperature calculated from Monte Carlo simulations, and hydrogen and argon ion densities as function of power. Results are at 4 cm from the outlet on the centerline which is near where the particle temperature peaks. 59

4.1 Charge limits for bare silicon nanoparticles based on electron field emission, Eq. (4.1), and particle electron affinity given by either Eq. (4.3) or [7], all shown in integer form. 66
4.2 Comparison of analytical expression, Eq. (4.15) (solid lines), with Monte Carlo simulations (histograms) for three different values of charge limit, for argon plasma with $n_e/n_i = 1$, T_e =3 eV, and T_i =300 K. Particle diameter = 5 nm. 71
4.3 Comparison of analytical expression, Eq. (4.15) (solid lines), with Monte Carlo simulations (histograms) for three different values of charge limit, for argon plasma with $n_e/n_i = 1$, T_e =3 eV, and T_i =300 K. Particle diameter = 10 nm. 72
4.4 Charge distribution as a function of charge limit for 10-nm-diameter particles in an argon plasma with $n_e/n_i = 1$, T_e =3 eV, and T_i =300 K. (Top) average charge, (bottom) standard deviation. 74
4.5 Results of Monte Carlo simulations for 10 nm-diameter silicon particles, with or without charge limits, for the same plasma conditions as in Fig. 4.2 except that n_e/n_i is varied. The solid line in the bottom graph shows Gaussian distribution predicted without charge limits, Eq. (4.7). 76
4.6 Particle charge distributions for 10 nm-diameter silicon particles (q_{lim} = 14), with either Ar^+ or H^+ as the positive ion. Conditions: $n_e/n_i = 1$, T_e =3 eV, and T_i =300 K. 78
4.7 Temporal evolution of average charge for 10 nm-diameter particles in an argon with $n_e/n_i = 1$, T_e =3 eV, and T_i =300 K. 80
4.8 Power spectrum of charge fluctuations for 5 nm-diameter particles in an argon plasma with $n_e/n_i = 1$, T_e =3 eV, and T_i =300 K. (top) Without charge limits, (bottom) with a charge limit of -5. 82
5.1 Flow chart of the Monte Carlo charging code: t is the instantaneous time, ϕ_p is the particle potential, ν_e is the electron collision frequency, ν_i is the ion collision frequency, ν_{see} is the frequency of secondary electron emission, ν_{ph} is the frequency of photoemission, t_{coll} is the next time a collision/emission event occurs, Q is the instantaneous particle charge, Δt is the time step of the simulation, and t_{end} is the total simulation time. 92

5.2 Particle charge distribution obtained by MC simulations for different electron-to-ion density ratio (left) $n_e/n_i = 0.1$, (middle) $n_e/n_i = 0.01$, and (right) $n_e/n_i = 0.001$, for a 10-nm-diameter particle at T_e =2 eV, T_i =300 K, O_2^+ ion, n_i=10^9 cm^{-3}, and the ion current is given by OML theory [8]. Charge limits and emission processes are not included. The electron energy distribution is assumed to be Maxwellian. 93

5.3 Average particle charge obtained by MC simulations for pressures 0.1−100 Torr for a (left) 10-nm and (right) 100-nm-diameter particle, T_e =2 eV, T_i =300 K, Ar^+ ion, and $n_e = n_i$=10^9 cm^{-3}. The capture radius Knudsen number is given in Ref. [9] and the ion current is given by Eq. (5.1). Charge limits and emission processes are not included. The electron energy distribution is assumed to be Maxwellian. 95

5.4 Average particle charge obtained by MC simulations for pressures 0.1−100 Torr and electron-to-ion density ratio $n_e/n_i = 0.01 - 1$ for a (left) 10-nm and (right) 100-nm-diameter particle, T_e =2 eV, T_i =300 K, Ar^+ ion, and n_i=10^9 cm^{-3}. The capture radius Knudsen number is given in Ref. [9] and the ion current is given by Eq. (5.1). Charge limits and emission processes are not included. The electron energy distribution is assumed to be Maxwellian. 96

5.5 Fraction of non-negatively charged particles obtained by MC simulations for a 10-nm-diameter particle (left) as function of pressure and (right) as function of electron-to-ion density ratio at T_e =2 eV, T_i =300 K, Ar^+ ion, n_i=10^9 cm^{-3}. Particle charge limit is included−for 10 nm SiO_2 particle, q_{lim}=3. Emission processes are not included. The electron energy distribution is assumed to be Maxwellian. 97

5.6 Results are obtained by MC simulations. (Left) Particle charge distribution for SiO_2 particles using different values for secondary electron emission coefficients, δ_M=2.1−4 and E_M=400 eV [1], (right) fraction of non-negatively charged particles for SiO_2 of 1−100 nm in diameter, T_e =2 eV, T_i =300 K, p = 10 Torr, Ar^+ ion, n_i=10^9 cm^{-3} and $n_e/n_i = 0.1$. Charge limits and photoemission are not included. The electron energy distribution is assumed to be Maxwellian. 98

5.7 (Left) Maxwellian and non-Maxwellian electron energy distribution functions (EEDFs) at the same effective electron temperature, $T_e = 4$ eV. The non-Maxwellian distribution was calculated using Bolsig+ [10]. (Right) Charge distribution obtained by MC simulations using Maxwellian and non-Maxwellian EEDFs to calculate the electron current to particle for a 80 nm diameter particle at $T_i = 300$ K, $p = 5$ Torr, $n_e/n_i = 0.1$, and $n_i = 10^9$ cm^{-3}. Charge limits and photoemission are not included. . . . 100

5.8 (Left) Effective secondary electron emission yield for the Maxwellian and non-Maxwellian distributions from Fig. 5.7(left) and charge distribution for a 80-nm-diameter particle without accounting for secondary electron emission. (Right) Charge distributions that account for secondary electron emission and using Maxwellian and non-Maxwellian EEDFs to calculate the electron current to particle for a 80 nm diameter particle at $T_i = 300$ K, $p = 5$ Torr, $n_e/n_i = 0.1$, and $n_i = 10^9$ cm^{-3}. Charge limits and photoemission are not included. 101

5.9 Particle charge distribution obtained by MC simulations for different photon fluxes to a 100-nm-diameter particle at T_e =2 eV, T_i =300 K, Ar^+ ion, n_i=10^9 cm^{-3}, $n_e/n_i = 0.1$, and $p = 10$ Torr. Charge limits and secondary electron emission are not included. The electron energy distribution is assumed to be Maxwellian. 102

6.1 Schematic of the Plasma-Aerosol code developed by Girshick and coworkers [5, 11, 12, 13, 14]. Each module calculates and returns some set of variables that are used by the other modules. R_{surf} is the surface growth rate, R_{nuc} is the nucleation rate, Q_p is the dust particle space charge, N_p is the dust particle density, E is the electric field, N_e is the electron density, N_i is the density of the species i, and T_e is the electron temperature. The code uses a time slicing method, meaning that the time step in each module is different, and depends on the plasma conditions. 107

6.2 Schematic of the parallel-plate capacitively-coupled RF plasma system. When the plasma is ON, the electric field traps the negatively charged particles at the center of the discharge. When the plasma is turned OFF, a positive DC bias V_B is applied at the substrate to accelerate the negative nanoparticles. By changing the plasma conditions and V_B, the nanoparticle flux and impact energy can be tuned. 115
6.3 Species densities just before turning off the plasma for (left) electron, positive and negative ions, (right) neutrals. 116
6.4 Nanoparticle spatial distribution just before turning off the plasma for (left) nanoparticle size distribution, (right) positive, negative, and neutral nanoparticles. 118
6.5 Spatiotemporal evolution of positive and negative ions and nanoparticles in the plasma OFF phase when the DC bias is applied at the substrate with V_B=400V. The time 0 μs corresponds to the moment V_B is applied. 120
6.6 Spatiotemporal (0−5 μs) evolution of (left) electron density and (right) electron temperature in the plasma OFF phase when the DC bias is applied at the substrate with V_B=400V. The time 0 μs corresponds to the moment V_B is applied. 121
6.7 Spatiotemporal (0−5 μs) evolution of (left) negative and (right) positive ions in the plasma OFF phase when the DC bias is applied at the substrate with V_B=400V. The time 0 μs corresponds to the moment V_B is applied. 122
6.8 Spatiotemporal (0−50 μs) evolution of (left) plasma potential and (right) electric field in the plasma OFF phase when the DC bias is applied at the substrate with V_B=400V. The time 0 μs corresponds to the moment V_B is applied. 123
6.9 Temporal evolution at the substrate of (left) instantaneous and effective electric fields and (right) effective electric field and negative nanoparticle flux in the plasma OFF phase for a 1.27-nm-diameter particle when the DC bias is applied at the substrate with V_B=+400V. The time 0 μs corresponds to the moment V_B is applied. 124

6.10 Impact energy distribution (atom/eV) at the substrate when the DC bias is applied at the substrate with V_B=400V. The distribution is averaged over the entire plasma OFF phase period. 125

Nomenclature

α	Polarizability
ΔG	Change in free Gibbs energy
ΔH_k	Change in enthalpy of reaction k
ε	Energy or material dielectric constant
ε_0	Vacuum permittivity
ε_p	Nanoparticle relative dielectric constant
$\mathbf{\Gamma}$	Flux vector
Γ_i	Flux of radical i
Γ_T	Total nanoparticle flux at the substrate during the afterglow period
κ_i	Thermal conductivity of species i
λ_L	Linearized Debye length
μ	Electric mobility
μ_0	Vacuum permeability
∇	Gradient operator in space
∇_r	Gradient operator in space
∇_v	Gradient operator in velocity
$\bar{\bar{\nu}}_i$	Viscosity tensor of neutral species i
ν_{ij}	Collision frequency between species i and j
ν_k	Stochiometric coefficient of species k in a reaction
π	Mathematical constant
ϕ	Electric potential
ϕ_{Si}	Flux of charged species i incident onto surface S
Φ	Inter-particle potential
ρ_c	Electrostatic charge density
ρ_p	Nanoparticle mass density
ρ_S	Charge density in or on non-plasma materials
σ	Cross section
σ^2	Variance for nanoparticle charge distribution
σ_0	Orbit momentum cross section for the cut off Coulomb potential
σ_{ed}^e	Electron-dust momentum transfer cross section
σ_M	Material conductivity

Symbol	Description
A	Constant for Arrhenius-like reaction
$\bar{A}_i$	Average value of section i
b_c	Collection impact parameter for the ion drag force
$b_{\pi/2}$	Impact parameter for ions whose asymptotic orbit angle is $\pi/2$ for the ion drag force
$\boldsymbol{B}$	Magnetic field vector
C	Constant for nanoparticle charging
C_p	Nanoparticle heat capacity
D	Diffusion coefficient
d_p	Nanoparticle diameter
e	Elementary charge
$\boldsymbol{E}$	Electric field vector
$\tilde{E}$	Effective electric field
$\tilde{E}_s$	Surface effective electric field at the substrate
E_A	Energy of activation
E_{image}	Nanoparticle coagulation enhancement factor due to image potential
f	Electron energy distribution function
$f_{i,k}$	Fraction of the change in enthalpy of reaction k that is partitioned to species i
f_s	Spacing factor in the sectional model
F_{ID}	Ion drag force
F_{ND}	Neutral drag force
F_{np}	Energy impact distribution of nanoparticle to a substrate
G	Rate of heating due to all surface processes
G_1, G_2, and G_3	Coefficients for change Gibbs free energy
$\dot{G}_{surf}$	Growth rate in unit length per unit time
$\boldsymbol{F}$	External forces acting on a particle
$\boldsymbol{I}$	Identity tensor
$\boldsymbol{J}$	Electric current density
$I_e(q)$	Electron current to a nanoparticle of charge q
$I_i(q)$	Ion current to a nanoparticle of charge q
k or k_B	Boltzmann constant
k_e	Electron impact rate constant
k_f	Forward rate constant of reaction
k_L	Langevin rate constant
k_n	Rate constant for neutral-neutral reaction
k_r	Reverse rate constant of reaction
K	Equilibrium constant of reaction
L	Rate of cooling by thermal conduction to the gas
m	Mass
m_e	Electron mass

n	Number density
n_d	Continuous nanoparticle size distribution
n_i	Number density of radical i
n_q	Nanoparticle charge distribution
N	Number density
$N_{j,k}$	Number density of nanoparticle in section j and charge k
p	Pressure
p_m	Induced dipole
$\boldsymbol{P}$	Pressure tensor
P_{atm}	Pressure of 1 atm
P_i	Partial pressure of species i
q	Electric charge
$\bar{q}$	Nanoparticle average charge
q_u	Charge of nanoparticle u
q_v	Charge of nanoparticle v
$\boldsymbol{q}$	Energy flux vector
$\boldsymbol{Q}$	Heat flow vector
$\dot{Q}_{surf}$	Growth rate in unit volume of gas per unit time
$\dot{Q}_{intra}$	Intra-sectional growth rate in unit volume of gas per unit time
$\boldsymbol{r}$	Position vector
$\bar{r}_i$	Average nanoparticle radius of section i
r_u	Radius equivalent to a nanoparticle of volume u
r_v	Radius equivalent to a nanoparticle of volume v
R	Nanoparticle radius
R_k	Source term for exothermic and endothermic processes k
R_n	Reaction rate of nucleation reaction n
$\boldsymbol{R_\varepsilon}$	Net rate of change in energy by elastic and inelastic collisions
$\boldsymbol{R_m}$	Net rate of change in momentum by elastic and inelastic collisions
$\bar{s}_i$	Average nanoparticle surface of section i
s_i	Sticking coefficient of radical i with a nanoparticle
S	Net source term
$S_{charging}$	Source term due to nanoparticle charging
S_{coag}	Source term due to coagulation
S_{growth}	Source term due to surface growth
S_j	Source term for surface growth in a section j
S_{nuc}	Source term due to nucleation
t	Time
T_e	Electron temperature
T_i	Ion temperature
u	Logarithm of nanoparticle volume or nanoparticle velocity
u_i	Logarithm of nanoparticle volume of section i

v	Velocity
v_i	Volume of radical i
$\bar{v}_i$	Average nanoparticle volume of section i
$\bar{v}_j$	Average nanoparticle volume of section j
$v_{i,l}$	Lower volume limit of section i
$v_{i,u}$	Upper volume limit of section i
v_p	Nanoparticle volume
$v_{th,i}$	Thermal velocity of radical i
$\boldsymbol{v}$	Velocity vector
V_B	DC bias potential applied at the substrate
V_{RF}	RF potential applied at the powered electrode
$\dot{V}_{surf}$	Growth rate in unit volume per unit time

Chapter 1

Introduction

1.1 General Introduction

Plasma is an ionized gas that contains free electrons, positive and negative ions, and neutral particles in their ground and excited states. Laboratory plasmas are mostly weakly ionized, meaning that their degree of ionization is typically less than 10^{-4}. Such plasmas produce highly reactive radicals with densities much greater than those of usual neutral gases, leading the way to new possible reaction pathways. In thermal plasma (thermal equilibrium), electrons and heavy particles have the same temperature, usually over 1000 K. Such plasmas can be used for welding [15], cutting [16], and low voltage circuit breakers [17]. In nonthermal plasmas, the electron temperature is much greater than that of heavy particles, which remains near room temperature. These plasmas are widely used in industry for material processing, such as thin-film deposition by plasma-enhanced chemical vapor deposition (PECVD), etching, and ion implementation. Plasmas containing solid or liquid particulates, ranging from nanometer to micrometer in size, are called *dusty plasmas*. The presence of such particles strongly affects plasma properties, especially when their densities approach electron and ion densities. Many efforts have been made to understand particle formation mechanisms and the physics of such plasmas [18], along with their industrial applications.

Semiconductor materials are widely used in microelectronics and optical devices. While various semiconductor materials exist (groups IV, III-V, and II-VI), silicon is by far the most used element, mostly due its abundance on Earth, low cost, and low toxicity.

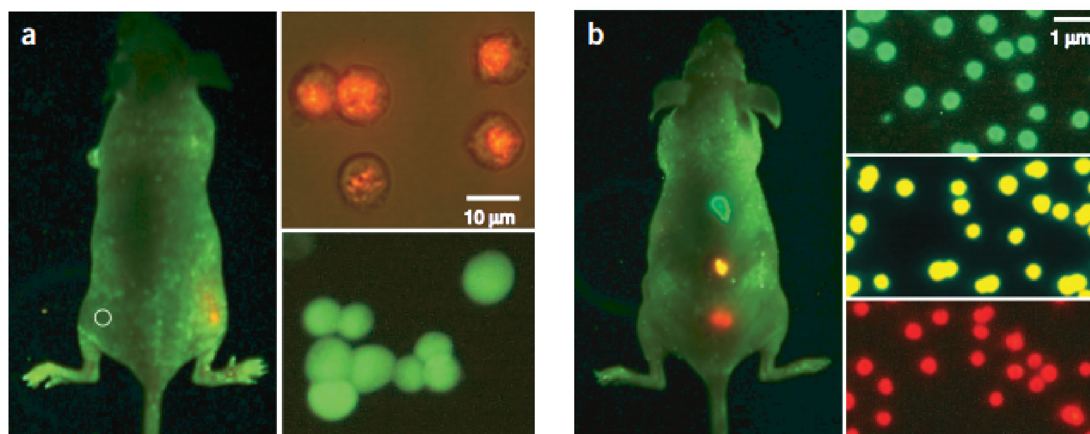

Figure 1.1: Sensitivity and tunable color capability of NC imaging in live animals.(a,b) Sensitivity and spectral comparison between NC-tagged and traditional protein transfected cancer cells [2]

Silicon is a major component in chips, which are used for a variety of applications (e.g. mobile phones, computers, and automobiles). The production of such semiconductor devices requires hundreds of different steps, such as lithography, thin layer deposition, and etching. Because plasmas have unique properties, they are used in many of these steps, which has helped in reducing the size of these devices. In the early 1990s, the deposition of large solid particles (nano- to micrometers) was observed on wafers [19]. Such particles are considered to be contaminants when they are similar in size to the feature size of the device.

Apart from their contaminant effects in the semiconductor industry, nanoparticle properties can strongly differ from their bulk properties as size decreases. At small sizes (< 10 nm), crystalline nanoparticles, also known as nanocrystals or quantum dots, have the property of emitting light at a wavelength that depends on their size. This property is shown to be beneficial in biomedicine, where nanocrystals can be used as emitting biosensors for *in vivo* cancer targeting imaging [2]. Fig. 1.1 compares light emission from traditional emitting proteins (weak green light) with nanocrystals (yellow to red light) on rats, demonstrating that contrast and tunable color capability can be significantly improved using nanocrystals.

Nanocrystals can also be used for their absorption property in photovoltaics. The

electricity generated in solar cells results from the absorption of photons that will create electron-hole pairs and enable a net current. The rate of photon absorption is most efficient when the photon energy matches the band gap. Solar cells with unique band gap cannot be very efficient as most photons would not be absorbed, since they exhibit an energy distribution. Nanocrystals of different sizes can be deposited on multi-layer solar cells, hence increasing the overall photon absorption. Recently, new techniques for nanocrytal deposition on solar cells and electronics have been developed. A promising technique is the use of nanocrystal inks (stable nanocrystal solution in a solvent) [20].

Because size-tunable nanoparticles have potential applications in electronics, sensors, medicine, and renewable energy, it is important to have reliable synthesis methods. The next section presents such techniques and provides some key features of synthesis by nonthermal plasmas.

1.2 Silicon Nanoparticle Synthesis in Plasmas

Silicon nanoparticles can be produced in the liquid phase [21], or in the gas phase including high temperature thermal reactions in furnace flow reactors [22], precursor dissociation through laser light irradiation [23], and laser pyrolysis using high power infrared lasers [24]. Using such techniques, it is rather difficult to produce narrow size distributions since there is no force that opposes interparticle interactions, leading to agglomeration. As discussed in the following, plasma offers an alternative method for particle synthesis with unique beneficial properties. It is a well-known technique that has been used in a wide range of plasma conditions: low- and high-pressure, and generated in capacitively- and inductively-coupled modes.

Plasma characteristics depend on many factors including plasma generation, pressure, gas mixture, and degree of ionization. Nanoparticle synthesis in nonthermal plasmas can overcome some limitations that occur in other synthesis technique. Nanoparticle synthesis in nonthermal plasma offer unique advantages compared to other plasma conditions. In nonthermal plasmas, the electron temperature is high ($>$1 eV) while the background gas remains near room temperature. Therefore, the dissociation of the precursor gas is achieved by electron impact reactions rather than gas heating. Compared to a neutral gas, a plasma contains positive and negative species that can attach to

nanoparticles, leading to charged nanoparticles that respond to electromagnetic fields. Because electron mobility is much greater than ion mobility, nanoparticles tend to be negatively charged, reducing agglomeration and hence producing smaller particle sizes [25] and narrower size distributions. In a plasma reactor, the wall electric potential is usually less than the plasma potential in order to balance positive and negative fluxes to the wall. This induces a confinement of negative nanoparticles, increasing their residence time, which leads to more time for particles to grow. Finally, selective nanoparticle heating can elevate nanoparticle temperature hundreds of Kelvin higher than the gas temperature, and above the size-dependent crystallization temperature. This is explained by exothermic reactions on nanoparticle surfaces, including ion recombination and hydrogen surface reactions, such as H passivation of a dangling bond releasing 3.1 eV (binding of the Si-H bond). Experimental and numerical evidence of such phenomena has been shown [26, 27].

While nonthermal effects are easily achieved in low-pressure plasmas, it would be suitable to achieve nanoparticle synthesis at atmospheric pressure to avoid the cost associated with vacuum equipment. At higher pressures, gas heating becomes important because of the increase in energy transfer from electrons to neutral species. The gas temperature can go over 1000 K, which is not always suitable for nanofabrication. Microdischarges help to preserve nonthermal plasma effects at atmospheric pressure by increasing power loss to the wall [28]. Also, because of the smaller reactor, the residence time of the gas is reduced, which helps in achieving smaller sizes. Silicon nanoparticle synthesis with narrow size distributions has been achieved [29]. Fig. 1.2 shows a typical microdischarge reactor, along with particle images obtained from electron transmission microscopy.

1.3 Numerical Plasma Modeling

Many important plasma quantities can be found experimentally, such as electron density and temperature, electron energy distribution function (EEDF), and gas composition. Some techniques are invasive (e.g. probe measurement) and can affect plasma properties. Other techniques are non-invasive (e.g. spectroscopy, laser light scattering) and give information on gas composition. However, some reactors do not have easy optical access,

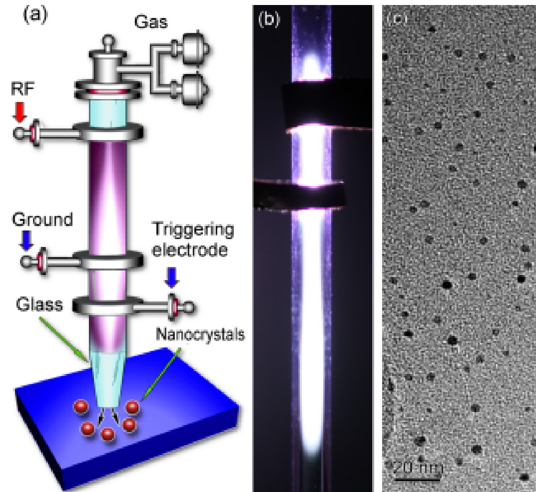

Figure 1.2: Silicon nanoparticle synthesis has been achieved under atmospheric plasma conditions. (a) Schematic of a plasma reactor, (b) photo of a microplasma generated inside a quartz capillary, and (c) representative transmission electron microscopy images of the silicon nanoparticles synthesized in microplasma [3]

.

which imposes severe limitations for the use of such techniques. Finally, experiments can be costly and time consuming. Therefore, numerical modeling can be used to overcome experimental limitations. Plasma modeling is widely used in academia and industry.

Commercial and academic software has been developed to investigate plasma characteristics and behavior for a wide range of conditions. COMSOL Multiphysics [30] and ANSYS [31] developed modules for low- to atmospheric-pressure plasmas. Academic software has been developed for low-temperature plasmas (e.g. PLASIMO [32], HPEM [6]) and high-pressure and liquid plasmas (e.g. nonPDPSIM [33]). Plasma enhanced chemical vapor deposition (PECVD) is a widely used technique for growing films for various applications. Therefore, understanding plasma surface interactions at the microscopic level is crucial and can be done using Molecular Dynamics simulation tools (e.g. LAMMPS [34]). Plasmas are reactive gases due to the high concentration of radicals. Depending on plasma conditions, including pressure, flow rate, and temperature, reaction mechanisms may vary strongly. There are available tools for sensitivity analysis in chemical kinetics to find the main reaction pathways, along with finding significant species depending on plasma parameters. Recently, PUMPKIN (pathway reduction

method for plasma kinetic models) is a tool that has been developed for that purpose [35]. Highly detailed plasma reaction mechanisms can include hundreds to thousands of reactions. Sets of reactions can be solved using commercial and free software (e.g. CHEMKIN [36], ZDPLASKIN [37]). In low-pressure plasmas, gas dissociation mostly occurs by electron impact reactions, so that reaction rates strongly depend on the EEDF that can be calculated using codes such as BOLSIG+ [10] and ELENDIF [38].

Computational time is reducing with the advancement of technology, supercomputers (e.g. Minnesota Supercomputing Institute [39]), the development of new powerful algorithms, and the use of parallel processing. Most common is open multi-processing (OpenMP) [40], used for programming multi-core machines with shared memory systems, and message passing interface (MPI) [41], used for parallel computers with distributed memory. This enables modelers to develop more sophisticated models, including more physics, making results more reliable.

1.4 Motivation

As shown in Section 1.2, plasmas represent a good alternative for nanoparticle synthesis with respect to other techniques. This thesis focuses on numerical modeling of silicon particle synthesis in low-pressure, nonthermal plasmas. This section gives an overview of previous work that have been done in the field and how this thesis contributes to the understanding of particle growth, charging, and transport.

Boufendi and Bouchoule first described the mechanisms of nanoparticle growth [42]. Along with experimental evidence, they divided particle growth into three phases: (1) formation of very small nanoparticles (nucleation), (2) growth by coagulation while decreasing particle density, and (3) growth by radical deposition on particle surfaces (surface growth) at constant particle density. This fundamental finding led the way to many numerical studies in order to understand each phase more accurately, along with transport effects, and nanoparticle cloud coupling to plasma.

Silane (SiH_4) is widely used as feedstock gas for radical production responsible for Si particle formation through nucleation and deposition on particle surfaces. Under nonthermal plasma conditions, nanoparticle nucleation occurs from chemical reactions leading to large molecules, over tens of silicon atoms (clusters). It is therefore crucial to

find out what the main species present in the system are, and the reaction chain leading to cluster formation. Swihart and Girshick calculated thermodynamic properties of silicon hydride species [43]. Bhandarkar *et al.* developed a zero-dimensional model to study silicon nanoparticle clustering, using over 8000 reactions and 300 species [44]. They found that the main pathway was through negative ions due to their longer residence time in plasmas, given that they tend to be trapped by the electric field. Recently, reaction mechanisms at an atomistic level of anion-neutral silicon hydride reactions responsible for nucleation were studied by means of *ab initio* calculations [45]. The same authors have used a similar approach to determine the kinetic rate constants of such reactions.

Because charged particles respond to electromagnetic fields, understanding nanoparticle charging mechanisms in plasmas is important. As particle size decreases, the stochastic nature of charging becomes significant, and looking at charge distributions rather than average charge is important. Indeed, even though particles can be mostly negative, a high fraction of neutrals can be present in the plasma. Because neutral particles are not trapped in the plasma, the overall particle growth mechanisms can be strongly affected. Matsoukas and Russell derived an expression for charge distributions in low-pressure plasmas accounting for electron and ion attachment only [46]. Gallagher studied Si particle growth in silane discharges and including particle charge limit for small particle sizes ($<$2 nm) [7].

De Bleecker *et al.* developed a one-dimensional capacitively-coupled plasma model to study nanoparticle formation and growth in a parallel-plate system [47]. The nucleation rate was found from a chemistry based on [44]. Electron impact rate constants were calculated using a Boltzmann solver for the electron energy distribution function. They implemented a sectional model to follow particle size in the range 1 to 100 nm. In their work, they assume a particle average charge for transport, but neglected nanoparticle charging for coagulation. A more detailed model was developed by Warthesen and Girshick [5], who included the effects of charge distribution on particle growth and transport. While their code is computationally intensive, it provides more insight in particle growth and transport mechanisms. In this model, Ravi and Girshick added nanoparticle charging effects in coagulation and found that it was an important contribution to particle growth due to the induced dipole between large highly charged

particles and smaller neutral ones [12]. Agarwal and Girshick improved the model by adding a detailed silicon hydride chemistry [13], and studying nanoparticle formation and growth in pulsed plasmas [48].

The aim of this thesis is to contribute to the understanding of nanoparticle formation in nonthermal plasmas. This work reports numerical models for two types of plasma systems. Nanoparticle charging is studied analytically and numerically over a wide range of plasma conditions.

1.5 Content of this Thesis

As demonstrated in this chapter, silicon nanoparticles can be used for many applications, depending on their size and material properties. Crystallinity plays an important role since small nanocrystals have a tunable wavelength of emission. Nanoparticle synthesis using nonthermal plasmas is a well-known technique and the fundamental processes leading to particle formation, growth, transport, and charging have been extensively studied. This thesis aims to provide new insight on these mechanisms by combining them in highly detailed self-consistent models.

In Chapter 2, the governing equations of dusty plasmas are presented. Starting from the Boltzmann equation, the set of fluid equations is presented for any particle in plasmas. Since charged particles respond to electromagnetic fields, Maxwell's and Poisson's equations are presented. A nanoparticle cloud is usually not monodisperse so that nanoparticles exhibit a size distribution. To numerically follow nanoparticle growth over a large range of sizes, a sectional model is implemented to considerably reduce the number of equations to solve. Models for growth mechanisms, including coagulation (two particles colliding to form a larger particle) and surface growth (radical deposition on nanoparticle surfaces) are presented in a sectional model framework. Finally, the governing equations for nanoparticle charging in low-pressure nonthermal plasmas are presented.

In Chapter 3, a two-dimensional model of a narrow quartz tube capacitively-coupled radio-frequency flowing plasma used for silicon nanoparticle synthesis is presented. The model is based on an actual experimental set-up that produces 1 to 5-nm-diameter particles [49]. A detailed description of the model includes governing equations for plasma

and nanoparticle mechanisms, i.e., growth, charging, and transport. Since particle formation results from silicon hydride reactions, a description of the chemical mechanisms is presented. The result section presents nanoparticle growth mechanisms and transport based on plasma properties (e.g. plasma potential and chemical reactions). Finally, scaling with power is shown to understand its effects on particle crystallization.

In Chapter 4, stochastic charging and particle charge distributions are discussed. Specifically, the effects of single-particle charge limits−maximum number of electron that can coexist on a single particle−on particle charge distribution are presented. An analytical expression for charge distribution accounting for particle charge limit is derived and compared with a Monte Carlo charging model. The effects of charge limits on temporal evolution of charge distribution is also discussed.

In Chapter 5, particle charging is studied under typical plasma-enhanced chemical vapor deposition (PECVD) conditions, since there is an interest in the semiconductor industry. The effects of electronegativity, ion collisions with the neutral background (pressure), charge limits, and electron emission processes on charge distributions are discussed. More importantly, we present the range of plasma conditions that favors the existence of neutral and positive particles, since they can escape the plasma and deposit on the substrate in typical parallel-plate systems.

In Chapter 6, a one-dimensional model of a parallel-plate system is improved to study Si particle flux and impact energy to a substrate in H_2/SiH_4 pulsed plasma at moderate pressure (2 Torr). The description of the model is presented along with the set of chemical reactions implemented. Particle transport in afterglow is discussed, as well as the temporal evolution of the electric field at the substrate.

Chapter 2

Governing Equations of Dusty Plasmas

2.1 The Boltzmann Equation

The behavior of any particle in a plasma can be described by its distribution function $f(\mathbf{v}, \mathbf{r}, t)$ in the six-dimensional phase space of particle positions $\mathbf{r}$ and velocities $\mathbf{v}$ at a given time t. The evolution of the distribution is represented by the Boltzmann equation:

$$\frac{\partial f}{\partial t} + \mathbf{v} \cdot \nabla_r f + \frac{\mathbf{F}}{m} \cdot \nabla_v f = \left(\frac{\partial f}{\partial t} \right)_{coll}. \tag{2.1}$$

On the left-hand side, the operators ∇_r and ∇_v denote gradients in space and velocity respectively, $\mathbf{v}$ is the particle velocity, and $\mathbf{F}$ represents the external forces acting on a particle of mass m. The term on the right-hand side represents the change in the distribution function due to elastic and inelastic processes such as ionization, excitation, and interactions with dust particles. For charged particles, external forces are represented by the Lorentz force, $\mathbf{F} = q(\mathbf{E} + \mathbf{v} \times \mathbf{B})$ where q is the particle charge, $\mathbf{E}$ is the electric field and $\mathbf{B}$ is the magnetic field. While the Boltzmann equation can be used for any particles in a plasma, the equation is highly non-linear and there is no analytical solution available. Due to computational limitations, the Boltzmann equation is mostly used to calculate the electron energy distribution function (EEDF). It is also used for the ion energy distribution function (IEDF) in certain systems such as the

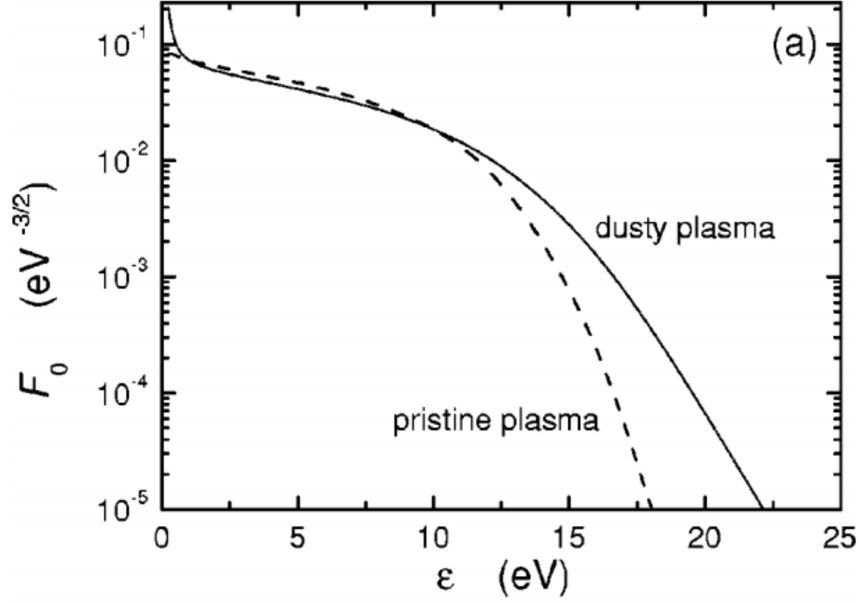

Figure 2.1: Comparison of electron energy distribution functions for pristine and dusty plasmas in argon [4]

.

etching reactor, in which surface interaction processes are strongly guided by the ion energy (e.g. ion chemical reaction and ion sputtering). The EEDF has strong effects on plasma properties since electron transport coefficients and electron impact rates depend on it. The rate constant for an electron impact reaction is

$$k_e = \int_0^\infty \left(\frac{2\varepsilon}{m_e}\right)^{1/2} f(\varepsilon)\sigma(\varepsilon)d\varepsilon, \tag{2.2}$$

where ε is the electron kinetic energy and $\sigma(\varepsilon)$ is the cross section. Inelastic and elastic cross sections can be found in the literature and online databases (e.g. LXcat [50]). The presence of dust particles in plasma can strongly affect the EEDF, as shown in figure 2.1.

The electron Boltzmann equation can be solved by direct Monte Carlo methods as shown by Boeuf and Marode [51]. While this method gives an accurate description of the EEDF, it is computationally demanding and therefore often difficult to implement in multi-dimensional systems. Alternative methods exist to solve the electron Boltzmann equation under certain assumptions: provided that the electric field is not too high and

that the rate of elastic collisions is much greater than the rate of inelastic collisions, the EEDF can be expanded in terms of spherical harmonics. The two-term approximation truncates the expansion after the second term, so that the distribution becomes [52]

$$f(\mathbf{v},\mathbf{r},t) \approx f_0(\mathbf{v},\mathbf{r},t) + \frac{\mathbf{v}}{v} \cdot f_1(\mathbf{v},\mathbf{r},t), \tag{2.3}$$

where $f_0(\mathbf{v},\mathbf{r},t)$ and $f_1(\mathbf{v},\mathbf{r},t)$ are the isotropic and anisotropic parts respectively. Inserting Eq. (2.3) into (2.1) gives a set of equations that can be solved numerically and relatively fast. This approach is widely used and has been investigated in numerous studies [53], including dusty plasmas [54]. Solvers can be found in the literature, including ELENDIF[38] and BOLSIG+[10].

Macroscopic quantities can be found from the first moments of the Boltzmann equation, leading to the *fluid model*. This is shown in the next section.

2.2 The Fluid Model

The Boltzmann equation is challenging to solve without a certain number of assumptions. For many plasmas, macroscopic quantities are enough information to understand and predict plasma behavior. The fluid model is widely used for a broad range of plasma conditions, when the electron mean free path is smaller than the reactor length scale. Fluid equations can be derived by taking the first few moments of the Boltzmann equation. This is done by multiplying Eq. (2.1) by $A \equiv A(v)$ and integrating over the velocity space: $A = 1, m\mathbf{v}$, and $\frac{1}{2}mv^2$ for zeroth, first, and second moments respectively. A detailed derivation can be found in Ref. [55]. The zeroth moment is the continuity equation,

$$\frac{\partial n}{\partial t} + \nabla \cdot \mathbf{\Gamma} = S, \tag{2.4}$$

where n, $\mathbf{\Gamma}$, and S are the density, flux, and net source term. The first moment is the momentum equation and is expressed as

$$mn\left(\frac{\partial}{\partial t} + \mathbf{v} \cdot \nabla_r\right)\mathbf{v} + m\mathbf{v}S + \nabla_r \cdot \mathbf{P} - nq\mathbf{E} = \mathbf{R}_m, \tag{2.5}$$

where m is the mass, $\mathbf{P}$ is the pressure tensor, q is the charge, and $\mathbf{R}_m$ is the net of rate change in momentum by elastic and inelastic collisions. The second moment is the

energy equation, given by

$$\frac{\partial}{\partial t}(n\varepsilon) + \nabla_r \cdot \mathbf{q} + \frac{\partial}{\partial t}\left(\frac{1}{2}mnv^2\right) - n\mathbf{v} \cdot q\mathbf{E} = R_\varepsilon, \tag{2.6}$$

where R_ε is the net rate of change in energy by inelastic collision. The heat flux is

$$\mathbf{q} = \varepsilon n\mathbf{v} + \frac{1}{2}mv^2 n\mathbf{v} + \mathbf{v} + \mathbf{v} \cdot \mathbf{P} + \mathbf{Q}, \tag{2.7}$$

where $\mathbf{Q}$ is the thermal heat flow vector. To close the system of equations, it is assumed that the pressure tensor reduces to a scalar, $\mathbf{P} = p\mathbf{I}$. $\mathbf{I}$ is the identity tensor and $p = nkT$, where k is the Boltzmann constant and T is the temperature. The thermal heat flow follows Fick's law, $\mathbf{Q} = -K\nabla T$, where K is the thermal conductivity. The first term of Eq. (2.5) can be neglected when it does not significantly change particle momentum compared to other terms. The equation can be rearranged to give the flux, using the drift-diffusion approximation, as

$$\mathbf{\Gamma} = -\mu n\mathbf{E} - D\nabla_r n, \tag{2.8}$$

where are μ and D are respectively the mobility and diffusion transport coefficients. This assumption is particularly valid for electrons, where transport coefficients can be derived from the EEDF.

Finally, it is worth mentioning that while it is common to use continuity, momentum, and energy equations only, higher-order fluid models have been developed, e.g. in a streamer discharge [56].

2.3 Maxwell's Equations and Poisson's Equation

Charged particles in plasmas respond to electromagnetic fields that are governed by Maxwell's equations:

$$\nabla \cdot \mathbf{E} = \frac{\rho_c}{\varepsilon_0}, \tag{2.9}$$

$$\nabla \cdot \mathbf{B} = 0, \tag{2.10}$$

$$\nabla \times \mathbf{E} = -\frac{\partial \mathbf{B}}{\partial t}, \tag{2.11}$$

$$\nabla \times \mathbf{B} = \mu_0 \mathbf{J} + \mu_0 \varepsilon_0 \frac{\partial \mathbf{E}}{\partial t}, \tag{2.12}$$

where $\mathbf{E}$, $\mathbf{B}$, and $\mathbf{J}$ are the electric field, the magnetic field, and the electric current density respectively, ρ_c is the electrostatic charge density, and ε_0 and μ_0 and are the permittivity and permeability of free space respectively. This thesis focuses on capacitively-coupled RF plasmas in which magnetic fields can be neglected. Also, at such frequency, the time varying electric field is low and can be neglected. It is worth mentioning that this approximation is valid for DC and RF plasmas, but not at microwave frequency. Because $\nabla \times \mathbf{E} = 0$, and using a vector calculus identity, the electric field derives from a scalar electric potential ϕ:

$$\mathbf{E} = -\nabla \phi. \tag{2.13}$$

Inserting Eq. (2.13) into (2.9) gives

$$\nabla^2 \phi = \frac{\rho_c}{\varepsilon_0}, \tag{2.14}$$

which is known as Poisson's equation. Poisson's equation is an elliptic equation, meaning that the electric potential has to be solved on the entire numerical domain at once, with correct boundary conditions. Poisson's equation is therefore challenging to solve, limiting the number of points in a mesh and the computational time.

2.4 Nanoparticle Growth Mechanisms

2.4.1 Nanoparticle Size Distribution

The number of particles per unit volume dN at a given position and at a given time in the particle diameter range d_p to $d_p + d(d_p)$ is

$$dN = n_d(d_p, \mathbf{r}, t) d(d_p) \tag{2.15}$$

where $n_d(d_p, \mathbf{r}, t)$ is the continuous nanoparticle size distribution function and has units of cm^{-3} nm^{-1} (as a convention in this thesis). Similarly, in terms of particle volume, the size distribution is $n_d(v_p, \mathbf{r}, t)$. In the rest of this thesis, and for clarity reasons, we will refer to size distributions by $n_d(d)$ and $n_d(v)$, where $d \equiv d_p$, $v \equiv v_p$, and omitting space and time dependencies $(\mathbf{r}, t)$.

Under the plasma conditions used in this work, the formation of the smallest nanoparticle size occurs through a polymerization chain of reactions. The rate of formation of these small nanoparticles is called the nucleation rate. Nucleated particles will grow by coagulation (two nanoparticles colliding to form a larger nanoparticle) and surface growth (gas-phase radical deposition on nanoparticle surfaces). In plasmas, nanoparticle charging plays a significant role in nanoparticle transport and growth. It is discussed in Chapters 4 and 5.

Following the spatiotemporal evolution of the nanoparticle size distribution can be very important to understand the mechanisms leading to nanoparticle growth and transport. For that matter, several methods have been developed: modal [57], discrete, moments [58], and sectional [59]. The method of moments has been used in thermal plasmas [60, 61, 62]. The method relies on using the first few moments of the size distribution, Eq. (2.15), and does not account for particle charging. Coagulation and surface growth can be expressed in terms of moments. However, to close the system of equations, assumptions have to be made. It is usually done by assuming the form of the size distribution as a log-normal distribution, which can be described in terms of moments too. This method is computationally efficient since it requires only three equations. However, not all nanoparticle size distributions are log-normal, and using other techniques may be more relevant.

In this thesis, we used a sectional model (schematic in figure 2.2) that is described in the next section.

2.4.2 Aerosol Sectional Model

The size range 0.5 to 5-nm-diameter particle corresponds to about 3−3000 silicon atoms per particle, assuming the mass density of bulk silicon (ρ_p=2.33 g cm^{-3}). Under typical plasma conditions, nanoparticles of these sizes may carry a few electrons only. As a result, there is a large number of discrete possible size-charge combinations and it would not be computationally tractable to solve continuity, momentum and energy equations for every possible species having a unique charge and number of Si atoms. A sectional model was introduced by Gelbard *et al.* [59] and has been used in many studies where particle size distribution matters. Sectional modeling provides a compromise between accuracy and computational efficiency [63]. In a sectional model, each section

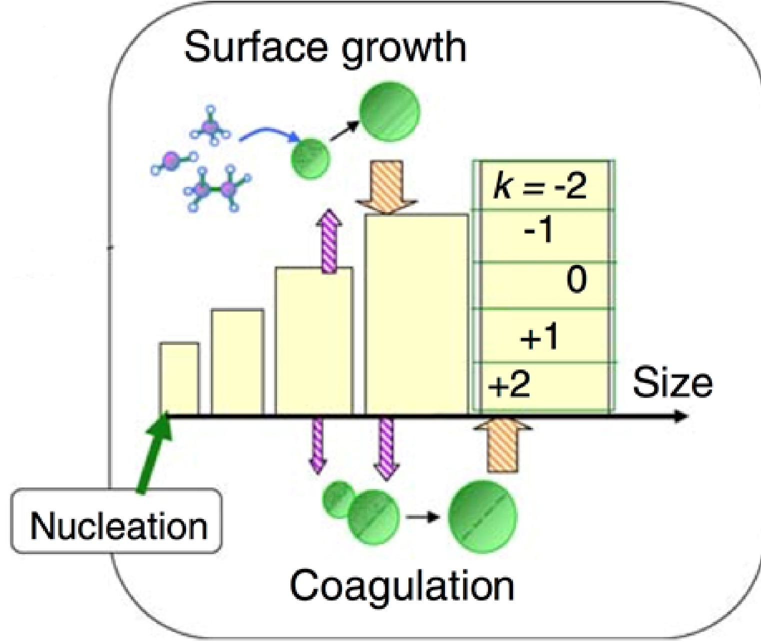

Figure 2.2: Schematic of a sectional modal: nucleation occurs in the first section and particles grow to higher sections by coagulation and radical deposition on nanoparticle surfaces [5]

.

corresponds to a range of particle sizes, which is represented by an average size, surface area, and volume of the particle. The size of each section size logarithmically varies, so that the smaller particle volume of each section depends on the previous section as

$$v_{i,u} = f_s v_{i,l}, \tag{2.16}$$

where $v_{i,u}$ and $v_{i,l}$ represent the upper and lower volume limit of section i, and f_s is the spacing factor of the sectional model. The spacing factor is a critical parameter for simulation−it needs to be small enough to avoid numerical diffusion but large enough to effectively reduce the number of equations and to reduce the computational burden. The average value of any quantity $A(u)$ in section i, where $u \equiv \ln v$, is given by

$$\bar{A}_i = \frac{\int_{u_{i-1}}^{u_i} A(u)n(u)du}{\int_{u_{i-1}}^{u_i} n(u)du}, \tag{2.17}$$

where $n(u)$ is the size distribution within section i. Assuming a uniform size distribution $n(u)$, Eq. (2.17) becomes

$$\bar{A}_i = \frac{\int_{u_{i-1}}^{u_i} A(u)du}{u_i - u_{i-1}}. \tag{2.18}$$

Using this expression, the average radius $\bar{r}_i$, surface area $\bar{s}_i$, and volume $\bar{v}_i$ in section i are given by

$$\bar{r}_i = 3\left(\frac{2}{4\pi}\right)^{1/3}\left(\frac{v_{i,u}^{1/3} - v_{i,l}^{1/3}}{\ln(v_{i,u}/v_{i,l})}\right), \tag{2.19}$$

$$\bar{s}_i = 1.5(3)^{2/3}(4\pi)^{1/3}\left(\frac{v_{i,u}^{1/3} - v_{i,l}^{1/3}}{\ln(v_{i,u}/v_{i,l})}\right), \tag{2.20}$$

$$\bar{v}_i = \frac{v_{i,u}^{1/3} - v_{i,l}^{1/3}}{\ln(v_{i,u}/v_{i,l})}. \tag{2.21}$$

The continuity equation (2.4) and the momentum equation (2.5) for each section can be solved using these averaged quantities. The energy equation (2.6) for nanoparticle is usually not solved since it is assumed that nanoparticles are in thermal equilibrium with the background gas. On the right-hand side of the continuity equation, source terms include nucleation (for the smaller sections), coagulation, surface growth, and charging. In the following sections, source terms in a sectional model are detailed.

2.4.3 Coagulation

Coagulation is a growth mechanism in which two particles collide to form a particle of larger size, conserving total volume. The time evolution of $n_d(v)$, the particle number density in a volume range between v and $v + dv$, accounting for coagulation only is [64]

$$\frac{\partial n_d(v)}{\partial t} = \frac{1}{2}\int_0^v \beta(u, v-u)n_d(u)n_d(v-u)du - \int_0^\infty \beta(u,v)n_d(u)n_d(v)du. \tag{2.22}$$

The first term on the right hand side represents the gain of particles in the volume range $[v, v + dv]$ with smaller particles. The second term represents the loss of particles in the same range due to coagulation with any other particles. In the free molecular regime, the coagulation rate constant between two particles of volume u and v is

$$\beta(u,v) = f(u,v,q_u,q_v) \times \left(\frac{3}{4\pi}\right)^{1/6}\left(\frac{6kT}{\rho_p}\right)^{1/2}\left(\frac{1}{u}+\frac{1}{v}\right)^{1/2}\left(u^{1/3}+v^{1/3}\right)^2, \tag{2.23}$$

where ρ_d is the particle mass density. The factor $f(u, v, q_u, q_v)$ accounts for the effects of charged-charged, charged-neutral, and neutral-neutral interactions, and is defined as

$$f(u, v, q_u, q_v) = \left\{ \begin{array}{ccc} 1 & \text{if} & q_u = q_v = 0, \\ 0 & \text{if} & q_u q_v < 0, \\ 1 - \dfrac{q_u q_v e^2}{4\pi\varepsilon_0 (r_u + r_v) kT} & \text{if} & q_u q_v > 0, \\ E_{image} & \text{if} & q_u \neq 0, q_v = 0, \end{array} \right\} \tag{2.24}$$

where r_u, r_v, q_u, and q_v are the radii and charges of particles of volumes u and v. The term E_{image} corresponds to the enhancement in collision frequency between charged and neutral nanoparticles due to the induced image potential. Ravi and Girshick [12] showed that the enhancement in coagulation could have significant effects, and could increase the overall coagulation rate by two orders of magnitude compared to neutral-neutral coagulation. The value of E_{image} was derived by Huang *et al.* [65] and is given as follows

$$\begin{aligned} E_{image} = \frac{1}{2} \int_0^1 \frac{1}{x^2} \frac{d}{dx} \left(x \frac{d\Phi(x)}{dx} \right) \times \exp\left(\frac{x}{2} \frac{d\Phi(x)}{dx} - \Phi(x) \right) dx + \\ \exp\left(\frac{1}{2} \frac{d\Phi(x)}{dx} \bigg|_{x=1} - \Phi(1) \right), \end{aligned} \tag{2.25}$$

with

$$x = \frac{r_u + r_v}{r}, \tag{2.26}$$

where r is the distance between the particles, and $\Phi(x)$ is the inter-particle potential approximated by the following expression,

$$\Phi(x) = \frac{aMx^2}{2(1 - bx^2)}, \tag{2.27}$$

$$M = \frac{e^2}{4\pi\varepsilon_0 kT (r_u + r_v)}, \tag{2.28}$$

$$a = \frac{\varepsilon_p - 1}{\varepsilon_p + 1} q_u^2 \left(1 - \frac{r_u}{r_u + r_v} \right), \tag{2.29}$$

$$b = \left(\frac{\varepsilon_p - 1}{\varepsilon_p + 1} \right) \left(\frac{r_u}{r_u + r_v} \right) \left(1 - \frac{r_u}{r_u + r_v} \right), \tag{2.30}$$

where ε_p is the dielectric constant of the particle material, e.g. 11.7 (silicon) and 16 (germanium).

Implementing coagulation in a sectional model has to be done with caution. It would be incorrect to use the average particle size and volume, Eqs. (2.19) and (2.21), in the equation for coagulation coefficient (2.23). Since a section corresponds to a range of sizes, and not discrete sizes, two particles of the same section could coagulate to form a larger particle, while remaining in the same section. Coagulation rate constants in a sectional model are lengthy and can be found in [59].

2.4.4 Surface Growth

In plasmas, high energy electrons dissociate the background gas, producing large concentrations of highly reactive radicals. Surface growth is defined as the growth in particle size due to the deposition of radicals on particle surfaces. The flux of radicals i to a nanoparticle surface is given by

$$\Gamma_i = s_i n_i v_{th,i}, \tag{2.31}$$

where n_i is the radical density and s_i is the sticking coefficient accounting for charging and surface material properties. The thermal velocity $v_{th,i} = \sqrt{\frac{8kT_i}{\pi m_i}}$ assumes a Maxwellian velocity distribution for radicals, where T_i is the radical temperature and m_i is the radical mass.

Growth rates can be expressed as

$$\dot{G}_{surf} = \sum_i \Gamma_i v_i, \tag{2.32}$$

$$\dot{V}_{surf,j} = A_j \sum_i \Gamma_i v_i, \tag{2.33}$$

$$\dot{Q}_{surf,j} = A_j N_j \sum_i \Gamma_i v_i, \tag{2.34}$$

where v_i is the volume of radical i. A_j and N_j are the surface area and number density of a nanoparticle of size j respectively. $\dot{G}_{surf}$ is in units of length per unit time, $\dot{V}_{surf}$ is in units of volume per unit time, and $\dot{Q}_{surf}$ is in units of volume per unit time per unit volume of gas.

A surface growth mechanism can be included in a sectional model, as previously done in Refs. [66, 11]. The source term for surface growth in a section j is expressed as

$$S_j = \frac{1}{\bar{v}_j}(\dot{Q}_{intra,j} + \dot{Q}_{surf,j-1} - \dot{Q}_{surf,j}), \tag{2.35}$$

with

$$\dot{Q}_{surf,j} = \frac{\bar{v}_{j+1}}{\bar{v}_{j+1} - \bar{v}_j}\dot{Q}_{intra,j}. \tag{2.36}$$

Because the sectional model assumes a uniform particle density within a section, surface growth tends to produce numerical diffusion (overestimation of nanoparticle growth). Numerical diffusion effects can be reduced by decreasing the spacing factor f_s.

2.5 Nanoparticle Charging

2.5.1 Charging Mechanisms

A nanoparticle in a plasma collides with electrons, positive ions, and negative ions. As a result, nanoparticles get charged and respond to electromagnetic fields. When particles are large enough to accumulate many charges, or when their density becomes similar to electron or ion densities, the nanoparticle cloud can strongly affect plasma properties. Therefore, understanding the charging mechanisms is crucial to predict nanoparticle growth and transport. Nanoparticle charging is discussed in Chapters 4 and 5. In this section, we present the basics of nanoparticle charging that will be used in the rest of the thesis.

Since charging comes from charged species collisions, it is important to know electron and ion currents to nanoparticles. Under typical low-pressure plasma conditions, the electron temperature is much greater than the negative ion temperature so that negative charging is mostly due to electrons. Neglecting electron and ion collisions with the neutral background gas in the vicinity of the particle surface, the Orbital Motion Limited (OML) theory [8] is applicable and continuous expressions can be derived for electron (I_e) and ion (I_i) attachment currents to particles as a function of particle charge q. For

Maxwellian velocity distributions, these currents are given by

$$I_x(q) = \left\{ \begin{array}{ll} I_{x0}\exp\left(\frac{q_x e^2}{4\pi\varepsilon_0 RkT_e}q\right), & q_x q \geq 0 \\ I_{x0}\left(1 - \frac{q_x e^2}{4\pi\varepsilon_0 RkT_e}q\right), & q_x q < 0 \end{array} \right\}, \quad (2.37)$$

where

$$I_{x0} = \pi R^2 s_x n_x \sqrt{\frac{8kT_x}{\pi m_x}}. \quad (2.38)$$

Here $x \equiv e, i$ for electrons and ions, respectively, with q_x representing the charge ($q_e = -1$, $q_i = +1$), s_x is the sticking coefficient, T_x the temperature, m_x the mass, n_x the number density, k the Boltzmann constant, e the elementary charge, and ε_0 the vacuum permittivity. Currents can be strongly affected by other charging mechanisms such as photoemission [67], ion trapping [68], secondary electron emission [69], and single-particle charge limits [70]. When pressure increases, the effect of ion-neutral collisions in the vicinity of the particle strongly affects particle charging [9].

2.5.2 Particle Charge Distributions

The stochastic nature of particle charging in plasmas causes a population of nanoparticles of a given size to exhibit a distribution of charge states. A number of previous studies analyzed the form of this distribution [46, 71]. Charge fluctuations for a particle of a given size can be formulated as a one-step Markov process whose probability density is governed by the following equation:

$$\frac{\partial n_q}{\partial t} = I_i(q-1)n_{q-1} + I_e(q+1)n_{q+1} - [I_e(q) + I_i(q)]n(q), \quad (2.39)$$

where n_q is the probability density for a particle to carry q charges. This equation only considers electron and ion attachment, but adding currents for other phenomena is straightforward. Based on electron and ion current expressions, Eq. (2.37), Matsoukas and Russell derived an analytical solution for the stationary particle charge distribution under the assumptions that $4\pi\varepsilon_0 R^2/e^2 \ll 1$ and that the average particle charge is not too small [46]. They showed that the probability distribution for particle charge can be approximated by a normalized Gaussian distribution

$$n(q) = \frac{1}{\sigma\sqrt{2\pi}}\exp\left[-\frac{1}{2}\left(\frac{q-\bar{q}}{\sigma}\right)^2\right], \quad (2.40)$$

where $\bar{q}$ is the average particle charge, σ is the standard deviation of the distribution, and

$$\int_{-\infty}^{\infty} n(q)dq = 1. \tag{2.41}$$

For Maxwellian electron and ion velocity distributions,

$$\bar{q} = C\frac{4\pi\varepsilon_0 RkT_e}{e^2}\ln\left[-\frac{s_i n_i}{s_e n_e}\left(\frac{m_e T_e}{m_i T_i}\right)^{1/2}\right] \tag{2.42}$$

and

$$\sigma^2 = \frac{4\pi\varepsilon_0 RkT_e}{e^2}\left(1 - \frac{T_e}{T_e + T_i - \frac{e^2}{4\pi\varepsilon_0 Rk}\bar{q}}\right), \tag{2.43}$$

where σ^2 is the variance of the distribution. In Eq. (2.42), C is a constant that is weakly dependent on plasma parameters and independent of particle size. For argon plasmas over a wide range of temperatures, $C = 0.73$.

The charge distribution in Eq. (2.40) does not account for single-particle charge limits. An analytical expression for the charge distribution accounting for particle charge limits is derived and discussed in Chapter 4.

Chapter 3

Synthesis of Silicon Nanoparticles in Nonthermal Flowing Plasmas

This chapter is based on R. Le Picard, A. H. Markosyan, D. H. Porter, S. L. Girshick, and M. J. Kushner, "Synthesis of silicon nanoparticles in nonthermal capacitively-coupled flowing plasmas: processes and transport," *Plasma Chemistry and Plasma Processing*, 36(4):941-972, 2016 [72].

The main objective of this work was to develop a self-consistent two-dimensional model to simulate silicon nanoparticle formation, growth, charging, and transport in a capacitively-coupled RF flowing plasma in a narrow quartz tube as observed in existing experiments. The work was done in collaboration with the group of Prof. Kushner at University of Michigan, who developed the Hybrid Plasma Equipment Model (HPEM), a two-dimensional plasma hydrodynamics model. My work was to implement a new module into the HPEM−the Aerosol Sectional Module (ASM) follows the spatial evolution of nanoparticle size and charge distributions. The module solves continuity and momentum equations for all size-charge possible combinations. I implemented nanoparticle charging and nanoparticle growth by coagulation and radical deposition on nanoparticle surface. The nanoparticle cloud is self-consistently coupled to plasma. Because the formation of small nanoparticles comes from chemical reactions, I implemented a relevant set of reactions for argon, helium, and silicon hydride species.

3.1 Introduction

The formation and growth of silicon nanoparticles (diameter < 10 nm) in plasmas have been extensively investigated since the early 1990s due to many potential applications in light emission devices, electronics, sensors, catalysis, photovoltaics, biomedical imaging, cell biology, medicine and renewable energy [73, 74, 75, 76, 2, 77]. While a variety of nanoparticle materials have been explored, there is particular interest in Si nanoparticles due to an already existing technological knowledge base for Si-based materials. Si nanoparticle synthesis in the gas phase is a well established technique. However, nanoparticle agglomeration makes the size of the nanoparticles, or their monodisperse nature, difficult to control. Nanoparticle synthesis using nonthermal plasmas has unique features in terms of cleanliness, and control of size and crystallinity [78]. For example, the charging of nanoparticles in nonthermal plasmas tends to reduce the likelihood of mutual coagulation and so produces narrower size distributions. In parallel-plate systems, negatively charged nanoparticles can be confined by electric fields in the plasma, which increases their residence time and promotes growth. Nonthermal plasmas can be sustained at low and atmospheric pressures which extends the operational window for nanoparticle synthesis [49, 29, 79].

Nonthermal plasmas can also selectively heat nanoparticles significantly above the gas temperature which in turn aids in their crystallization. The crystallization temperature of amorphous silicon nanoparticles in the range of $4-10$ nm in size is about $700-1200$ K [80], which is typically much higher than the gas temperature in nonthermal plasmas. Monte Carlo models have shown that the nanoparticle temperature in these plasmas can fluctuate above the crystallization temperature due to hydrogen reactions and electron-ion recombination on the surface [26].

In typical low-pressure plasma conditions, the formation of nanoparticles occurs through a polymerization chain of reactions producing small clusters. Nanoparticle formation and growth mechanisms have been experimentally investigated by Boufendi and Bouchoule [42]. They found that nanoparticle formation in argon-silane discharges occurred in three steps (1) rapid nucleation, (2) coagulation and reduction of total

nanoparticle density, followed by (3) surface deposition of radicals on nanoparticle surfaces while the nanoparticle density remains nearly constant. There are limited experimental techniques that provide the fundamental parameters needed to determine the growth mechanisms of nanoparticles in nonthermal plasmas. The time evolution of particle size and concentration can be found from electrical measurements [81] or laser light scattering [42]. The consequences of nanoparticles on plasma properties has been investigated by Langmuir probe measurements of electron energy distribution functions [82, 54]. It is difficult to directly measure growth of particles following their nucleation. To date, there are few direct experimental measurements of chemical reaction pathways, the spatial distribution of plasma potential, nanoparticle charge fluctuations, and other processes that may influence particle growth. This situation motivates use of numerical modeling to help understand the mechanisms leading to nanoparticle synthesis.

As mentioned, silicon nanoparticles in plasmas are thought to nucleate through a polymerization chain in which small radicals are added to a larger growing silicon hydride cluster. Detailed plasma chemistry models have been developed whose results suggest that anionic pathways (that is, reactions involving negative ions) are responsible for particle nucleation due to the trapping of negatively charged particles in electropositive plasmas, which causes them to have a longer residence time than neutral and positive species in parallel-plate systems [44, 83]. Recently, *ab initio* calculations were used to understand the mechanisms of nucleation reactions at a molecular level [45]. Due to the larger rate coefficients of ion-molecule reactions compared to neutral-neutral reactions, and the trapping of negative particles by the electric field in the plasma, nanoparticle transport and growth are strongly coupled to nanoparticle charging. Under typical low-pressure plasma conditions, nanoparticles are mostly negatively charged. However, for particles that are only a few nanometers or less in diameter, the stochastic nature of charging results in charge distributions that strongly affect nanoparticle growth and transport [46, 71, 70].

Although the kinetics of nanoparticle growth in plasmas involves additional processes compared to non-plasma systems, the basic techniques of investigating nucleation and growth developed in the aerosol community still apply. One such technique is the sectional representation of the particle size distribution. The range of nanoparticle sizes is divided into smaller individual ranges called sections. Each section corresponds to a

range of sizes represented by an average diameter, surface area, and volume. Recently, a one-dimensional self-consistent model of a parallel plate capacitively-coupled radio frequency (RF) plasma was developed using a sectional model to investigate nanoparticle nucleation, transport, charging, and growth [5, 11]. For each size in the sectional model, a distribution of particle charge was determined based on local plasma properties. These studies found that coagulation can make a significant contribution to nanoparticle growth due to the high collision rate between negatively-charged and neutral nanoparticles, enhanced by the occurrence of image potentials in the neutral particle [65].

To provide insight into the fundamental processes and mechanisms of nanoparticle synthesis in low-pressure, nonthermal plasmas, in the present work, nanoparticle formation kinetics based on a sectional model were embedded into a two-dimensional plasma hydrodynamics model. The model was applied to the investigation of Si particle synthesis in a capacitively-coupled RF plasma sustained in Ar/He/SiH_4 mixtures flowing through a narrow quartz tube. The geometry is based on the experiments of Kortshagen and coworkers [49, 84, 27]. We found that nanoparticles, which are mostly negatively charged, are trapped radially in the plasma but not in the axial direction. Therefore, their size can be tuned by varying the background gas flow, as proposed experimentally. Due to the high neutral nanoparticle density, coagulation plays a significant role in particle growth.

3.2 Description of The Model

In this section, we describe the model we developed to simulate a capacitively-coupled RF plasma reactor for the synthesis of silicon nanoparticles. The basic model consists of a two-dimensional plasma-hydrodynamics simulation into which algorithms for particle nucleation, growth, transport and charging have been embedded in a self-consistent manner. Particle growth is described by a sectional model.

3.2.1 Hybrid Plasma Equipment Model (HPEM)

The basic plasma model into which the sectional model was embedded is the two-dimensional computational framework Hybrid Plasma Equipment Model (HPEM) [6].

The HPEM combines different modules that address different physical phenomena in low-temperature plasmas, as shown in Fig. 3.1. The electron energy transport module (EETM) and the fluid kinetics-Poisson module (FKPM) were used in this work. Continuity, momentum, and energy equations are separately solved for heavy species in the FKPM with collisional exchange terms for transfer of momentum and energy between particles. Electron fluxes are provided by a drift-diffusion approximation. Diffusion and mobility coefficients, as well as all electron impact rate coefficients, are derived from electron energy distribution functions (EEDFs) obtained by solving Boltzmann's equation using a two-term approximation. Poisson's equation is solved for the electric potential. A full description of the HPEM is contained in Ref. [6]. The set of equations for any species i, integrated in time simultaneously with Poisson's equations in a semi-implicit manner are

$$\frac{\partial N_i}{\partial t} = -\nabla \cdot \vec{\phi_i} + S_i, \tag{3.1}$$

$$\begin{aligned}\frac{\partial \vec{\phi_i}}{\partial t} = -\frac{1}{m_i}\nabla(N_i k_B T_i) - \nabla \cdot (N_i \bar{v_i} \bar{v_i}) + \frac{q_i}{m_i} N_i \vec{E} - \nabla \cdot \bar{\bar{\nu_i}} - \\ \sum_j \frac{m_j}{m_i + m_j} N_i N_j (\bar{v_i} - \bar{v_j}) \nu_{ij},\end{aligned} \tag{3.2}$$

$$\begin{aligned}\frac{\partial (N_i c_i T_i)}{\partial t} = \nabla \cdot \kappa \nabla T_i - P_i \nabla \cdot \vec{v_i} - \nabla \cdot (N_i \vec{v_i} \epsilon_i) + + \frac{N_i q_i^2}{m_i v_i} \vec{E_S}^{\,2} + \\ \sum_j 3 \frac{m_{ij}}{m_i + m_j} N_i N_j \nu_{ij} k_B (T_j - T_i) - \sum_k R_k f_{ik} \Delta H_k,\end{aligned} \tag{3.3}$$

where N_i, T_i, $\vec{\phi_i}$, and S_i are the density, temperature, mass, flux, and source for species i, and $\vec{E_S}$ is the electrostatic field produced by solving Poisson's equation. $\bar{v_i}$ is the velocity, $\bar{\bar{v_i}}$ is the viscosity tensor (used only for neutral species), ν_{ij} is the collision frequency between species i and species j, and ϵ_i is the internal energy. k_B is Boltzmann's constant, c_i is the heat capacity, κ_i is the thermal conductivity, q_i is the charge, and P_i is the partial pressure. The last term in Eq. (3.3) is a sum over reactions which accounts for exo- and endothermic processes where R_k is the source term for reaction k having change in enthalpy ΔH_k and f_{ik} is the fraction of that enthalpy that is partitioned to species i.

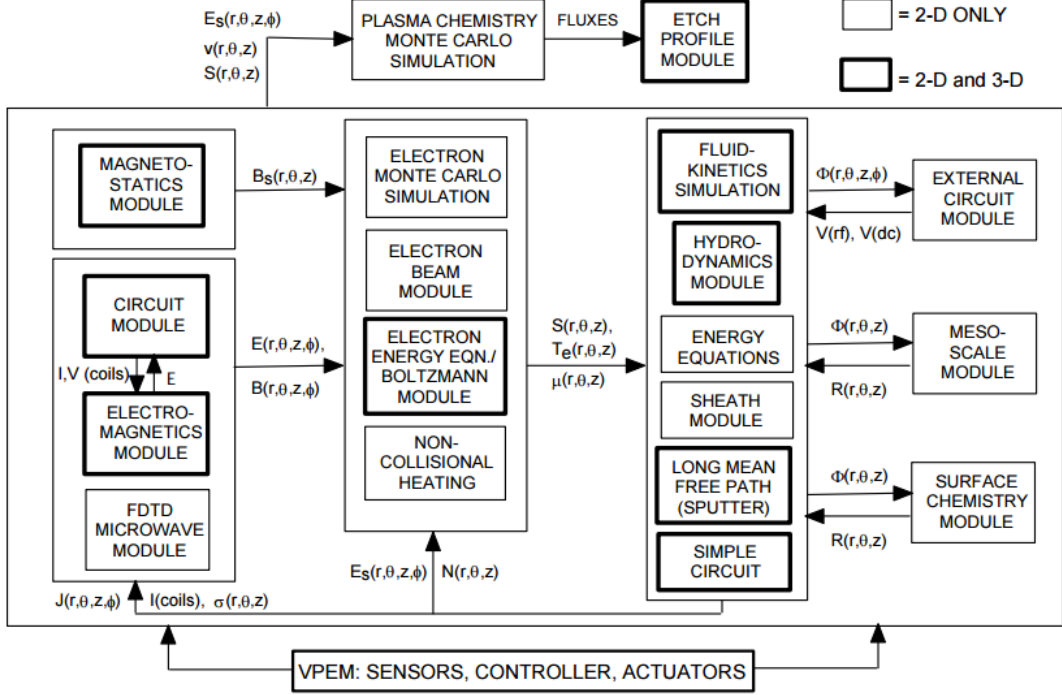

Figure 3.1: Schematic of the Hybrid Plasma Equipment Model (HPEM). Each module returns a set of variables that can be used by other modules [6].

Poisson's equation for the electric field is solved in the plasma and surrounding materials. To gain in computational time, the HPEM uses a semi-implicit method, so that Poisson's equation at a time $t + \Delta t$ is

$$\begin{aligned} -\nabla\varepsilon \cdot \nabla\Phi_S(t+\Delta t) = \\ \sum_i q_i(N_i(t) - \Delta t\nabla \cdot \phi_i(\Phi_S(t+\Delta t)) + S_i(t)) \\ +\rho_S(t) - \Delta t\nabla \cdot (\sum_i q_i\phi_{Si}(\Phi_S(t+\Delta t)) - \sigma_M \nabla\Phi_S(t+\Delta t)), \end{aligned} \tag{3.4}$$

where ε is the material dielectric constant, ρ_S is the charge density in or on non-plasma materials, ϕ_{Si} is the flux of charged species i incident onto surfaces in contact with the plasma, and σ_M is the material conductivity.

In this work, we implemented an Aerosol Sectional Module (ASM) to follow the spatial evolution of nanoparticle size and charge distributions. The module solves for nanoparticle formation, growth, transport, and charging. The module capabilities are

detailed in the following sections.

3.2.2 Aerosol Sectional Module

An Aerosol Sectional Module (ASM) is implemented in the HPEM to study the spatial evolution of nanoparticle growth. The detailed sectional model is presented in Section 2.4.2. Nanoparticles nucleate in the smallest sections and grow to higher sections by coagulation and surface growth. Coagulation is the collision between particles from different (or the same) sections to make larger particles. Surface growth is the deposition of silicon hydride radicals on the nanoparticle surface. The continuity equation for a unique charge state in a given section is

$$\frac{dN_{j,k}}{dt} = -\nabla \cdot \vec{\phi}_{j,k} + S_{nuc} + S_{coag} + S_{growth} + S_{charging}, \tag{3.5}$$

where j and k refer to section and charge respectively, $N_{j,k}$ is the nanoparticle density, $\vec{\phi}_{j,k}$ is the flux, and the source terms S are for nucleation, coagulation, surface growth, and charging. Summaries and discussions of each term in Eq. (3.5) are given below while a detailed description can be found in Section 2.4 and Refs. [5, 48] .

Due to their small size, gravity is not important in the transport of nanoparticles whereas gravity can be important to the transport of particles exceeding a few microns in diameter. The neutral and ion drag terms that are included in modeling the transport of macroscopic particles are naturally accounted for in the exchange terms of Eqs. (3.2) and (3.3).

The species included in the model are listed in Table 3.1. The nucleation rate is defined as the rate of formation of small clusters of some specified size in the first sections of the sectional model. Under similar plasma conditions, Bhandarkar *et al.* concluded that clusters are formed by a polymerization chain starting from the anionic silylene ($Si_2H_4^-$) and silyl ($Si_2H_5^-$) species [44]. The dominance of the anionic pathways in the formation of clusters is due to the trapping of negative species that leads to longer residence time in the plasma compared to positive and neutral species, as well as to the faster kinetics of ion-neutral reactions compared to most reactions between neutral molecules. The nucleation rate is taken as the sum of the rates of reactions that involve $Si_2H_4^-$ and $Si_2H_5^-$ species as a reactant and that add one Si atom to the anion

Table 3.1: Species included in the plasma chemistry model

Argon species	
Ar(3s)	Ar^{+}
$Ar(1s_5)$	Ar^{2+}
$Ar(1s_4)$	
$Ar(1s_3)$	
$Ar(1s_2)$	
Ar(4p)	
Ar(4d)	
Ar_2*	
Helium species	
He	
He*	
He^{+}	
Hydrogen species	
H	H^{-}
H_2	H_2^{+}
H_2*	H^{+}
H*	
Silicon hydride species	
Si	SiH^{-}
Si_2	SiH_2^{-}
SiH	SiH_3^{-}
SiH_2	$Si_2H_3^{-}$
SiH_3	$Si_2H_4B^{-}$
SiH_4	$Si_2H_5^{-}$
Si_2H_2	SiH_3^{+}
Si_2H_3	
Si_2H_4B (B for silylene)	
Si_2H_5	
Si_2H_6	

Table 3.2: Nucleation reactions included in the model

Nucleation reaction*	Rate constant (cm^3 s^{-1})**
$Si_2H_4B^-$ + SiH_4 → NP + H_2	4.83×10^{-11}
$Si_2H_4B^-$ + Si_2H_6 → NP + H_2	8.95×10^{-11}
$Si_2H_4B^-$ + SiH_2 → NP + H_2	4.95×10^{-11}
$Si_2H_5^-$ + Si_2H_4B → NP + H_2	9.02×10^{-11}
$Si_2H_5^-$ + SiH_4 → NP + H_2	4.83×10^{-11}
$Si_2H_5^-$ + Si_2H_6 → NP + H_2	8.92×10^{-11}
$Si_2H_5^-$ + SiH_2 → NP + H_2	4.93×10^{-11}
$Si_2H_5^-$ + SiH_3 → NP + H_2	4.88×10^{-11}
$Si_2H_5^-$ + Si_2H_3 → NP + H_2	9.02×10^{-11}
$Si_2H_5^-$ + Si_2H_5 → NP + H_2	8.95×10^{-11}

* NP represents a nanoparticle

** Rate coefficients are estimated to be 0.1 of the Langevin rate. (See text)

cluster−10 reactions in our mechanism, listed in Table 3.2:

$$S_{nuc} = \sum_n R_n, \tag{3.6}$$

where R_n is the reaction rate of reaction n. Note that the nucleation rate is a source term for the negatively charged states of the smallest sections, depending on the size of the nucleated particles−Si_3 or Si_4−which corresponds to a diameter ∼0.5 nm.

The rate constants for coagulation between two nanoparticles are derived assuming that all nanoparticles lie in the free molecular regime, and strongly depend on the charge state of the nanoparticles, since two particles of the same charge will normally not coagulate due to Coulomb repulsion. The coagulation rates between charged and neutral particles are enhanced compared to neutral-neutral rates due to the induced image potential [12]. Due to computational limitations, particle charge states are allowed to be neutral and negatively charged only. This assumption is reasonable under these plasma conditions, where the electron temperature is high, ∼3 eV, and the electron-to-ion density ratio is close to unity.

Surface growth occurs due to deposition of small radicals on the nanoparticle surface. We consider all monomer and dimer silicon hydride species as radicals in the surface growth model. The sticking coefficient on the nanoparticle surface is assumed to equal unity for all species except SiH (0.95), SiH_2 (0.8), SiH_3 (0.045), SiH_4 (10^{-5}), and Si_2H_6

(10^{-5}), as described in Refs. [85, 86]. Since two particles of the same charge do not collide at the temperature of interest (< 1000 K), negatively charged radicals can only deposit on neutral nanoparticles, while positive ions (SiH_3^+) can deposit on both neutral and negative nanoparticles. To simplify the surface reaction mechanism, we assumed silicon nanoparticles to be bare silicon. In reality, a large fraction of the surface sites of nanoparticles may be occupied by hydrogen, which can affect sticking coefficients of radicals and nanoparticle growth. Molecular dynamics has been used to study the effects of hydrogen passivation of silicon nanoparticles (2−6 nm) on coagulation [87].

The distributions of charge within each size section are individually computed as different species. Only electron and ion attachment processes are taken into account in particle charging. We do not consider secondary processes such as photo-electron emission or electron field emission. The charging probability density is defined as a one-step Markov process, where particle charge can only vary by ±1 charge at a time. the source term for particle charging for each size-charge combination is

$$S_{charging} = \sum_i I_i(k-1)N_{j,k-1} + I_e(k+1)N_{j,k+1} - \Big[\sum_i I_i(k) + I_e(k)\Big]N_{j,k}, \qquad (3.7)$$

where I_i is the current to the nanoparticle of ion species i and I_e is the electron current. Ion and electron currents to the particles are calculated from local plasma properties using orbital motion limited theory [8]. The thermal velocity distribution of ions is assumed to be Maxwellian. The electron current of electrons with nanoparticles is self-consistently calculated using rate coefficients provided by local solutions of Boltzmann's equation for the EED. The electron attachment current is given by

$$I_e = -\pi R^2 e n_e \int_{-e\phi_s}^{\infty} \Big(1 + \frac{e\phi_s}{u}\Big)\sqrt{\frac{2u}{m_e}} f(u)\sqrt{u}du, \qquad (3.8)$$

where n_e is the bulk electron density, u is the electron kinetic energy, and $f(u)$ is the EEDF. The EEDF is also affected by electron-dust momentum transfer where the cross section is [88]

$$\sigma_{ed}^e(u) = \pi a^2 \Big(\frac{-e\phi_s}{u}\Big)^2 e^{2a/\lambda_L} \ln\Lambda, \qquad (3.9)$$

with

$$\ln\Lambda \cong \ln\Big(\frac{\lambda_L T_e}{R(-e\phi_s)}\Big). \qquad (3.10)$$

Since the nanoparticles are included in the HPEM hierarchy in the same manner as other atoms and molecules in the plasma, their electron interactions are naturally included in the calculation of EEDFs.

3.2.3 Plasma Chemical Kinetics

Nucleation and surface growth in this system occur via reactions among silicon hydrides. Bhandarkar *et al.* developed a zero-dimensional low-pressure model of silicon hydride plasma chemistry consisting of 300 species, Si_nH_m (n<10), encompassing more than 6000 reactions [44]. Although that approach is insightful and may be more accurate from a kinetics perspective, including this large number of species and reactions in a 2-dimensional, plasma hydrodynamics model would be computationally prohibitive. In this model, we include 10 argon species, 3 helium species, 7 hydrogen species, and 18 silicon hydride species, Si_nH_m for $n \leq 2$, as listed in Table 3.1. The resulting hydrogen, argon, and helium chemistry is addressed with 165 reactions. Silicon hydride chemistry consists of 100 reactions.

The general form of rate constants for electron reactions is given by

$$k_e = \int_0^\infty \left(\frac{2\varepsilon}{m_e}\right)^{1/2} f(\varepsilon)\sigma(\varepsilon)d\varepsilon, \tag{3.11}$$

where $\sigma(\varepsilon)$ is the cross section for ionization, excitation, or dissociation. Most cross sections were found in the HPEM cross section database. When cross sections were unavailable, an Arrhenius rate constant was used.

Neutral-neutral reaction rate constants are expressed in the Arrhenius form

$$k_n(T) = A\Big(\frac{T}{298}\Big)^m \exp\Big(-\frac{E_A}{T}\Big), \tag{3.12}$$

where A and m are constants, T is the temperature, and E_A is the activation energy of the reaction.

Small cluster formation typically occurs by anion-neutral reactions because of their greater rate constants compared to neutral-neutral reactions. When a charged particle approaches a neutral particle, it induces a dipole that will attract the particles together. The hard sphere model for reaction rate constant is therefore not suitable, and an alternative expression has to be used. The dipole induced in a neutral particle, induced

by an electric field E, is expressed as

$$p_m = \alpha \varepsilon_0 E = \alpha \frac{e}{4\pi r^2}, \tag{3.13}$$

where α is the polarizability of the neutral particle and r is the distance between the two particles. Further calculation leads to the *Langevin rate constant*

$$k_L = \sqrt{\frac{\pi \alpha e^2}{\varepsilon \mu_r}}, \tag{3.14}$$

where μ_r is the reduced mass. The polarizability of silicon hydride molecules is assumed to follow [85]

$$\alpha(Si_n H_{2n+1}) \approx \alpha(SiH_4)[1 + 0.8(n-1)] = 4.64(0.2 + 0.8n)(\mathring{A}^3). \tag{3.15}$$

In the silicon hydride chemistry used in the model, charged-neutral reaction rate constants are given by the Langevin rate constant of Eq. (3.14) lowered by a factor of 10 [44]. Some comments need to be made regarding the Langevin approximation: it assumes that the reaction is a one-step process and that the reaction is barrierless. Recent computational *ab initio* calculations have shown that the barrier could be significant, such as for reactions $\mathrm{Si}_{n+1}\mathrm{H}_{2n+2}^- + \mathrm{SiH}_4 \rightarrow Si_{n+2}\mathrm{H}_{2n+4}^- + \mathrm{H}_2$, suggesting that Langevin rates could significantly overestimate some reaction rates. Other nucleation pathways could be possible, such as via excited vibrational states [89].

The favorable direction of a reaction changes with plasma conditions, therefore the reverse reaction rate constant is determined from the equilibrium constant

$$K(T) = \frac{k_f}{k_r}, \tag{3.16}$$

where k_f and k_r are the forward and reverse reaction rate constants. The equilibrium constant is

$$K(T) = \exp\Big(\frac{\Delta G(T)}{T}\Big)\Big(\frac{P_{atm}}{k_B T}\Big)^{\sum_{k=1}^{N} \nu_k}, \tag{3.17}$$

where $\Delta G(T)$ is the change in Gibb's free energy and ν_k are the stochiometric coefficients. The change in Gibb's free energy is defined in the following form in the HPEM,

$$\Delta G(T) = G_1(1 + G_2(T - 300) + G_3(T - 300)^2), \tag{3.18}$$

where G_1, G_2, and G_3 are constants calculated by Seal and Truhlar using *ab initio* methods [90]. Table 3.3 presents constants G_1, G_2, and G_3 for the reactions considered in this work.

Table 3.3: Change in Gibb's free energy, ΔG (in kcal/mol) as computed at the G3sX(MP3)// M06-L/MG3S level of theory for each reagent at a partial pressure of 1 bar. The unimolecular reagents are assumed to be fully equilibrated (i.e., to be in the high-pressure limit).

Reaction	Temperature (K)							
	300	400	500	600	700	800	900	1000
SiH_4 (+M) → SiH_2 + H_2 (+M)	44.7	41.45	38.11	34.72	31.32	27.91	24.5	21.11
Si_2H_6 (+M) → SiH_4 + SiH_2 (+M)	43.36	40.1	36.89	33.73	30.62	27.55	24.53	21.55
Si_2H_6 (+M) → H_2 + Si_2H_4B (+M)	42.72	39.09	35.39	31.66	27.91	24.16	20.42	16.69
Si_2H_4B (+M) → Si + SiH_4 (+M)	37.11	35.45	33.83	32.24	30.69	29.16	27.65	26.16
Si + Si_2H_6 → SiH_2 + Si_2H_4B	6.25	4.65	3.06	1.48	−0.07	−1.61	−3.12	−4.61
SiH_2 (+M) → Si + H_2	36.47	34.44	32.34	30.18	27.98	25.77	23.53	21.29
H + SiH_4 → H_2 + SiH_3	−15.38	−16.07	−16.77	−17.46	−18.15	−18.82	−19.47	−20.1
SiH_2 + SiH_2 → Si_2H_2 + H_2	−19.15	−18.6	−18.15	−17.76	−17.43	−17.13	−16.86	−16.6
H + Si_2H_6 → SiH_4 + SiH_3	−16.73	−17.42	−17.99	−18.46	−18.85	−19.17	−19.44	−19.65
H + Si_2H_6 → Si_2H_5 + H_2	−18.58	−19.39	−20.2	−21	−21.79	−22.56	−23.31	−24.03
SiH_3 + SiH_3 → SiH_2 + SiH_4	−23.01	−22.48	−21.93	−21.37	−20.8	−20.23	−19.66	−19.09
SiH_4 + SiH_3 → Si_2H_5 + H_2	−1.85	−1.96	−2.2	−2.54	−2.94	−3.39	−3.87	−4.38
SiH_4 + SiH → Si_2H_3 + H_2	−2.02	−2.47	−3.05	−3.7	−4.4	−5.15	−5.92	−6.71
SiH_2 + H → SiH + H_2	−28.44	−28.47	−28.5	−28.53	−28.555	−28.562	−28.557	−28.53
SiH_3 (+M) → SiH + H_2 (+M)	31.64	29.05	26.37	23.66	20.91	18.17	15.41	12.67
SiH + SiH_4 → Si_2H_4B + H	27.81	27.47	27.01	26.46	25.84	25.17	24.44	23.67
SiH_3 + H → SiH_2 + H_2	−38.39	−38.54	−38.69	−38.83	−38.95	−39.05	−39.13	−39.19
Si_2H_2 → Si_2 + H_2	35.16	32.92	30.66	28.38	26.11	23.85	21.59	19.36
Si_2H_4B → Si_2H_2 + H_2	32.26	29.37	26.42	23.45	20.47	17.5	14.54	11.6
SiH_3 + SiH_3 → Si_2H_6	−66.36	−62.57	−58.81	−55.09	−51.42	−47.79	−44.2	−40.64
SiH_2^- + SiH_4 → $Si_2H_4B^-$ + H_2	−12.78	−12.8	−12.92	−13.13	−13.41	−13.72	−14.07	−14.45
SiH_2^- + SiH → SiH_2 + SiH^-	9.29	9.57	9.86	10.15	10.44	10.74	11.03	11.33
SiH_2^- + SiH_3 → SiH_2 + SiH_3^-	−8.81	−8.53	−8.25	−7.97	−7.69	−7.41	−7.13	−6.85
SiH_2^- + Si_2H_3 → SiH_2 + $Si_2H_3^-$	−30.74	−30.22	−29.69	−29.15	−28.6	−28.05	−27.5	−26.94

continued

Reaction	Temperature (K)							
	300	400	500	600	700	800	900	1000
$SiH_2^- + Si_2H_5 \rightarrow SiH_2 + Si_2H_5^-$	−19.3	−18.96	−18.62	−18.27	−17.92	−17.58	−17.24	−16.89
$Si_2H_4B^- + SiH \rightarrow Si_2H_4B + SiH^-$	21.43	21.36	21.29	21.21	21.14	21.06	20.99	20.92
$Si_2H_4B^- + SiH_3 \rightarrow Si_2H_4B + SiH_3^-$	3.34	3.26	3.18	3.09	3.01	2.92	2.83	2.73
$Si_2H_4B^- + Si_2H_3 \rightarrow Si_2H_4B + Si_2H_3^-$	−18.59	−18.43	−18.26	−18.09	−17.91	−17.73	−17.54	−17.36
$Si_2H_4B^- + Si_2H_5 \rightarrow Si_2H_4B + Si_2H_5^-$	−7.15	−7.17	−7.19	−7.21	−7.23	−7.25	−7.28	−7.31
$SiH_3^- + SiH_4 \rightarrow Si_2H_5^- + H_2$	−12.34	−12.39	−12.57	−12.84	−13.18	−13.56	−13.98	−14.42
$SiH_3^- + SiH_2 \rightarrow Si_2H_3^- + H_2$	−37.01	−36.57	−36.22	−35.95	−35.73	−35.54	−35.38	−35.23
$SiH_3^- + SiH_3 \rightarrow Si_2H_4^- + H_2$	−26.99	−26.74	−26.6	−26.53	−26.52	−26.55	−26.61	−26.69

The unimolecular reagents are assumed to be fully equilibrated (i.e., to be in the high-pressure limit)

3.3 Computational Challenges

The motivation for this work was to develop a detailed multi-dimensional model for particle formation and transport while coupling the nanoparticle cloud to plasma. Because of the different time scales and the large number of equations to solve simultaneously, the model developed here is computationally intensive. The model solves for plasma and neutral transport, temperatures, and Poisson's equation using a combination of explicit, semi-implicit and implicit methods with time steps calculated based on instantaneous plasma properties or a fraction of the RF period. A typical time step used to maintain numerical stability and resolve the RF period is 10^{-10} s. Noting that the residence time for gas flow through the tube is $5-10$ ms, we would expect to reach full convergence after over 10 ms of integration.

Since we expect the experimental set-up to run in quasi-steady state, the rate of convergence is improved by better estimates for the initial conditions of nanoparticle densities. Estimating initial conditions for the spatial distribution of the section densities is made difficult by the complexity of the reaction mechanism and the lack of experimental evidence. Since it takes significant time for nanoparticles to grow to higher sections by surface growth and coagulation, we introduced a *boost* option which establishes better initial conditions than other estimation methods. When boosting is enabled, nucleation and surface growth rate coefficients are artificially increased by a factor F_b for a time T_b, after which the option is disabled and rate coefficients are returned to their normal values. For the conditions of this study, we used F_b=50 and T_b=20 μs.

A significant amount of computational time is consumed by the exchange terms for momentum and energy in Eqs. (3.2) and (3.3). These exchange terms for each species are sums over all other species at every mesh point, and so scale as n^2, where n is the number of species. From a practical matter, in a fluid simulation momentum transfer collision terms are only important between species for which at least one of the partners has a mole fraction larger than a specified value. After a sensitivity study, we found that an optimum value with respect to speed-up and accuracy is a mole fraction of 10^{-3}.

In order to benefit from multicore architectures, algorithms in the HPEM were parallelized using OpenMP directives [40]. Since the HPEM consists of many different

modules each having separate algorithms which are executed sequentially for relatively short times, it is difficult to amortize the computational overhead in launching parallel threads.

3.4 Particle Synthesis in RF Discharges: Base Case

In this section, we present base case results under typical plasma conditions. Plasma properties, chemical compositions, and silicon nanoparticle growth mechanisms are discussed in detail.

3.4.1 Model Schematic

The geometry used in this model is shown in Fig. 3.2a and represents the experimental set-up reported in Ref. [49]. Due to the high aspect ratio of the reactor, the radial dimension in all two-dimensional figures is scaled by a factor of four, shown in Fig. 3.2b, to enable details to be visually resolved. The plasma consists of a narrow quartz tube that starts at 0.8 cm inner diameter and 1 cm outer diameter (wall thickness of 0.1 cm). Gas is injected from the top and pumped out from the bottom. The tube expands to 1.4 cm inner and 1.6 cm outer diameter 2 cm below the electrodes. The upper electrode is powered at an RF frequency of 25 MHz and deposits a specified 1−5 W power in the plasma. In experiments, the power generator is typically set at 10−50 W and is connected to the quartz tube through a matching network. Some power is reflected to the generator, while some power is dissipated in the matching network and the dielectric tube. It is estimated than the power dissipated in the plasma is 3−5 times less than the power set by the generator. The voltage amplitude applied to the powered electrode is self-consistently adjusted to deliver the desired power. The inlet gas is a mixture of argon, helium, and silane, where argon has the dominant mole fraction. The silane used in this work was diluted in helium. The inclusion of He was merely to follow experimental conditions. Since the threshold energies for exciting and ionizing He are larger than for Ar and SiH_4, very little power is used in producing excited states and ions of He. Experiments have shown that varying the flow rate, which varies the residence time in the reactor, produces different nanoparticle sizes [27]: the higher the flow rate, the smaller the nanoparticle. In this investigation, the typical argon flow rate

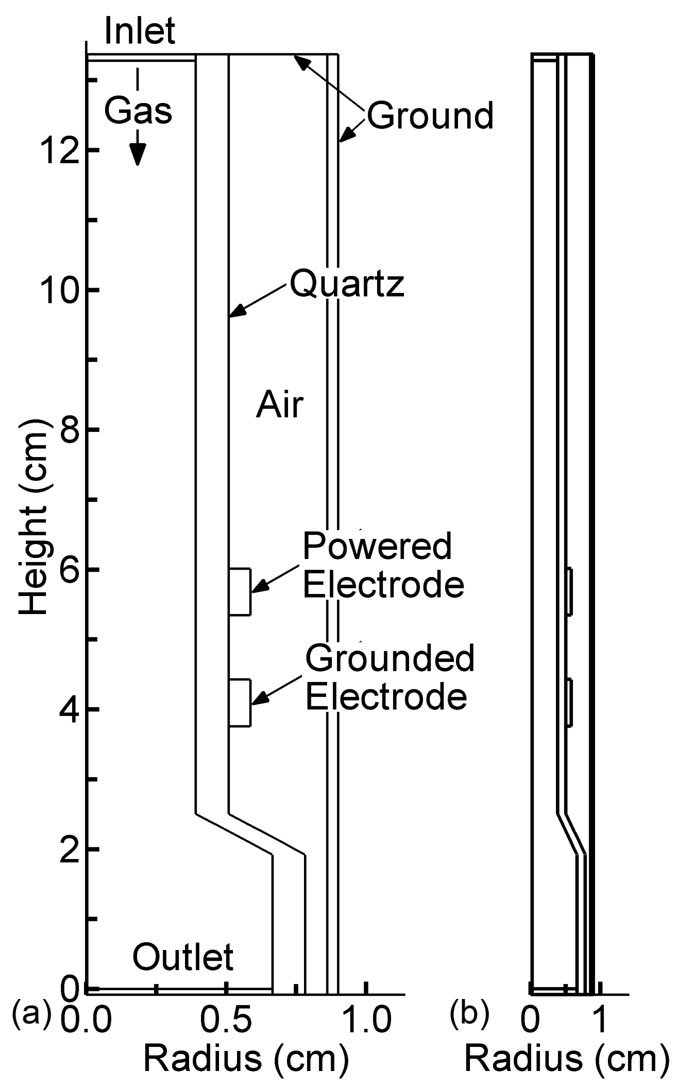

Figure 3.2: Schematics of the geometry used in our model. (a) Radius expanded by a factor of 4. (b) Actual geometry.

was 25-100 sccm. Nanoparticle deposition sticking coefficients with the wall are set to unity.

This geometry represents challenges in solving Poisson's equation consistent with the experimental apparatus and the observation that particles flow out of the reactor. The actual reactor has a large diffusion zone at the bottom of the geometry shown in Fig. 3.2, and this large volume could not be addressed by the model. A larger diffusion zone means more computational demand. This boundary condition is typically of the Dirichlet type, specifying the electric potential on the boundary. Doing so artificially traps negatively charged particles in the computational domain near the pump port where gas flow pushes particles into the electrostatic repulsion produced by the sheaths formed at the boundary. To address this issue, a Neumann boundary condition was implemented at the pump port for Poisson's equation and charged particle fluxes to enable their flow out of the system.

Under plasma conditions corresponding to these simulations, experiments produce particles up to $2-3$ nm [27]. The sectional model here uses up to 55 sections with a spacing factor, defined in Eq. (2.16), of f_s=1.15 [48]. The lower nanoparticle diameter of the first section is 0.49 nm, which corresponds to 3 Si atoms assuming the mass density of bulk silicon. Due to the particle charge limit, only one electron can be attached to a Si particle up to 2.4 nm in diameter [7, 70]. The total number of charge-size species within the sectional model therefore equals 90. The base case conditions were based on typical experiments [27]. The input gas mixture was Ar/He/SiH_4 = 50/4.75/0.25 sccm at the inlet. The pressure was kept constant at 1.5 Torr by adjusting the flow out of the reactor. The wall temperatures were held constant at 325 K and the power deposited in the plasma was 3W.

The results presented in the following sections are for 6 ms simulations and took over 4 months of computational time. The steady-state solution is not fully reached, as the densities of the higher sections are still increasing. However, if we were to run the code for longer, we would not expect significant qualitative differences in the spatial distributions of variables with the current results, while their magnitudes (e.g., species and nanoparticle densities) may change.

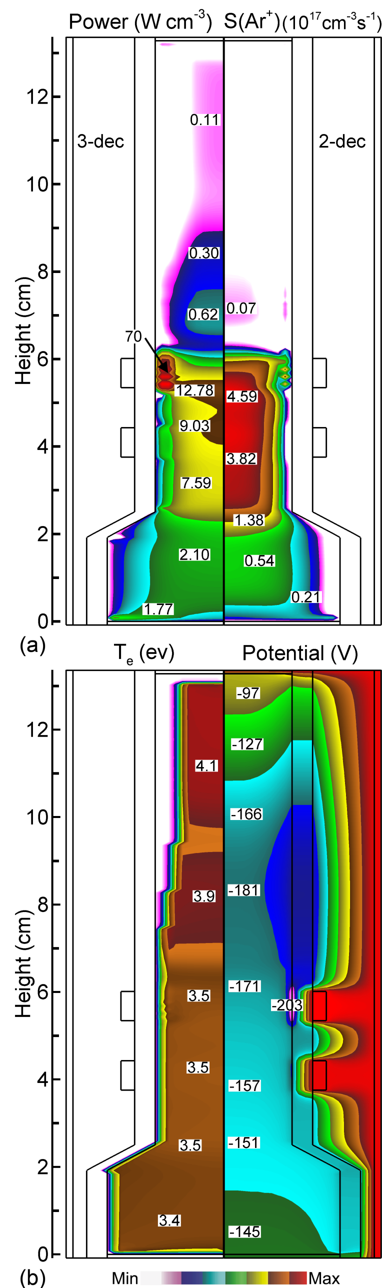

Figure 3.3: Plasma properties for the base case conditions (Ar/He/SiH_4 = 50/4.75/0.25, 1.5 Torr, 3 W, 50 sccm). (a) Densities of power deposition and Ar^+ source by electron impact, (b) electron temperature and electric potential. Log-scale plots have number of decades noted.

3.4.2 Plasma Properties

Results for spatial profiles of the densities of power deposition and the electron impact ionization source for Ar^+ are shown in Fig. 3.3. At the frequencies and pressures of interest, power deposition is largely into electrons by the oscillating electric field of the sheath. Most of the power is deposited within 1 mm of the boundary in the vicinity of the powered (top) electrode, with a maximum value of 70 W cm^{-3}. Two minor peaks in power deposition, about 10 W cm^{-3} between axial locations at 4 and 6 cm. are caused by Joule heating in the bulk plasma, and result from the positioning of the electrodes and division of the conduction and displacement currents. Electron impact ionization of argon is the dominant ionization source in the plasma, due to the large overall mole fraction of argon in the gas mixture. The double peaks in the ionization rate correspond to that of the power deposition.

The densities of electrons, negative ions, positive ions and total negative nanoparticles are shown in Fig. 3.4. The electron density peaks at 2.0×10^{12} cm^{-3} along the centerline between the two electrodes. Total positive and negative ion densities peak at 1.9×10^{12} cm^{-3} and 1.8×10^{12} cm^{-3}, respectively. The spatial extent of the electron density is largely confined to between the electrodes where the power deposition is large. Downstream of the electrodes, the balance between positive ions and negative charge is largely maintained by negative ions and negatively charged nanoparticles. Note that the lighter negative ions extend to a larger radius than the heavier nanoparticles. Due to the lower mobility and diffusivity of the nanoparticles, they tend to respond to the time-averaged potentials, which, in this case, have a maximum on axis. Electron depletion is not significant here due to the small size of the nanoparticles that typically hold only one negative charge or are neutral. In dusty plasmas that contain larger particles, the electron density can be significantly depleted by charging of the nanoparticles [11]. The dense plasma region extends to 2 cm below the electrodes as observed experimentally [49]. However, experimental electrostatic probe measurements report ion densities in the range 10^{10}-10^{11}, which is less that we find from our model. This discrepancy may be due to uncertainties in actual power deposition into the plasma due to matching issues from the power supply. The electron temperature is near 3.5 eV throughout the plasma region, as shown in Fig. 3.4b. This somewhat high electron temperature results from the consumption of electrons due to charging of nanoparticles, which then requires more

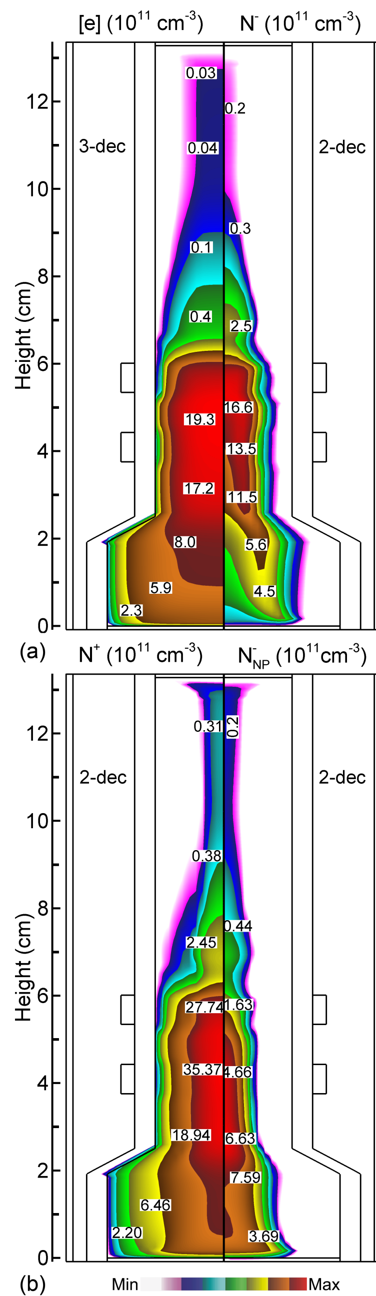

Figure 3.4: Charged particle densities for the base case conditions ($Ar/He/SiH_4$= 50/4.75/0.25, 1.5 Torr, 3 W, 50 sccm). (a) Electron and total negative ions, (b) total positive ions and total negative nanoparticles. Log-scale plots have number of decades noted.

ionization (produced by a higher electron temperature) to compensate.

With the voltage being applied to one electrode, the second electrode being grounded and the discharge surrounded by electrical ground, the discharge is asymmetric and a dc bias forms to balance the RF currents. In the model, there is a 20 nF blocking capacitor in series between the power supply and the discharge tube. Between the blocking capacitor and the plasma, there is the additional series capacitance of the electrode-tube-plasma sandwich, which is about 5 pF. Since the blocking capacitor is much larger than the capacitance of the electrode, the dc bias appears dominantly across the discharge tube under the powered electrode (see Fig. 3.4b). Since the blocking capacitance in most impedance matching networks is typically much larger than 5 pF, we expect the same distribution of dc bias voltage in the experiments.

Since overall the plasma is electropositive on an RF-period average, we expect negatively charged particles to be radially confined along the centerline. However, the electric potential monotonically increases in the axial direction from the electrode region to the outlet which, experimentally, is afforded by the large diffusion chamber downstream (and is approximated by our boundary conditions at the pump port). This overall gradient in potential works against trapping of negative nanoparticles in the axial direction and enables them to flow out of the reactor. The lifetime of negative nanoparticles is still lengthened compared to those of neutral nanoparticles due to their electrostatic trapping in the radial direction, preventing their deposition on the tube walls. However, since nanoparticles are not trapped in the axial direction, their residence time is close to the background gas residence time. This observation agrees with experiments, in which the sizes of nanoparticles are tuned by varying the background gas flow rate which translates into residence time [27].

3.4.3 Plasma Chemical Kinetics

The densities of silicon hydride species that are important for nanoparticle formation and growth are shown in Fig. 3.5. The density of SiH_4 is 2.2×10^{14} cm^{-3} at the inlet before its density is reduced by electron impact dissociation and hydrogen abstraction reactions while flowing though the tube. The rates of silane conversion to products and hence radical production along the centerline due to electron impact and hydrogen abstraction are shown in Fig. 3.6. Hydrogen abstraction reactions are more important

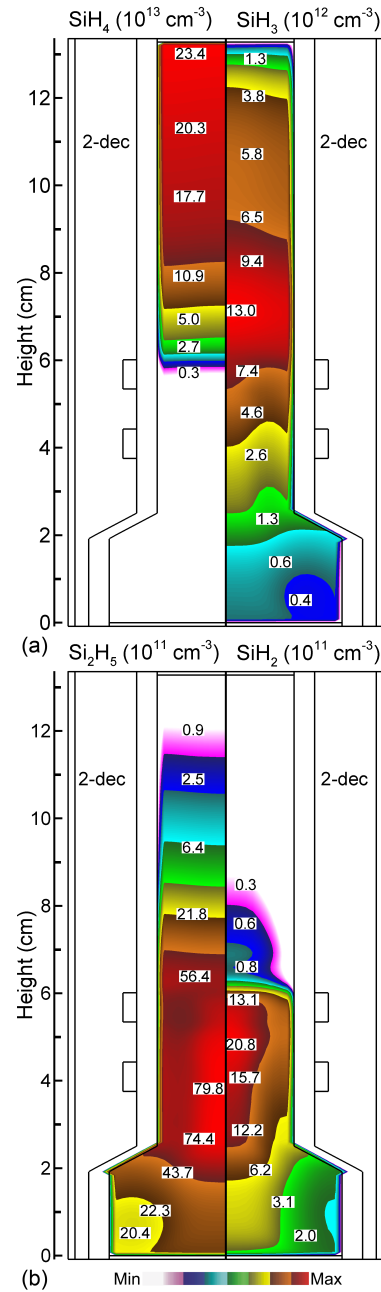

Figure 3.5: Silicon hydride densities for the base case conditions (Ar/He/SiH_4 = 50/4.75/0.25, 1.5 Torr, 3 W, 50 sccm). (a) SiH_4 and SiH_3, (b) Si_2H_5 and SiH_2. Log-scale plots have number of decades noted.

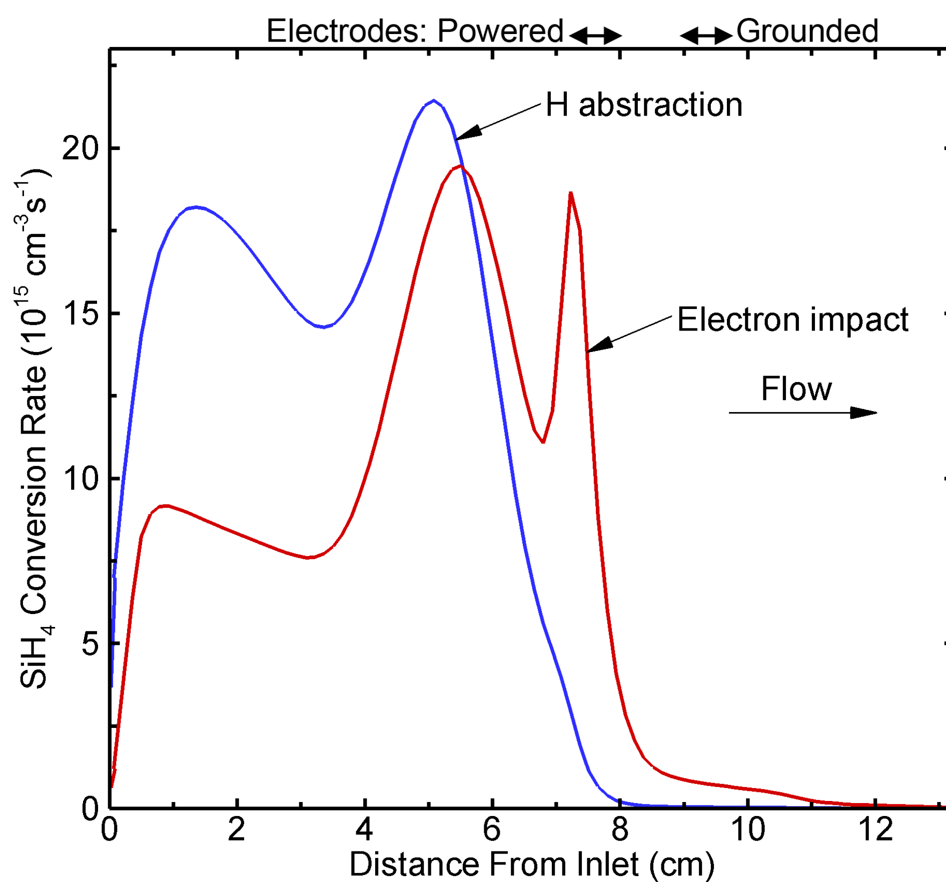

Figure 3.6: Rate of SiH_4 conversion to products by electron impact and hydrogen abstraction reactions along the centerline.

than electron impact dissociation in the upstream part of the tube, where the H density is three orders of magnitude greater than the electron density. Between the two electrodes, the SiH_4 density is four orders of magnitude smaller than at the inlet. The majority of this decrease is by dissociation though some is also due to rarefaction by gas heating. The densities of SiH_2, SiH_3, and Si_2H_5 peak at 1.9×10^{12} cm^{-3}, 1.2×10^{13} cm^{-3}, and 6.4×10^{12} cm^{-3} respectively, increasing in density downstream as the SiH_4 is dissociated while flowing from the inlet. The advective speed of gas flowing through the tube is 1.8 m/s along the centerline, and so there is some back diffusion of species towards the inlet.

Electron impact dissociation of SiH_4 produces both SiH_2 (silylene) and SiH_3 (silyl) in reactions that also produce atomic H. The H atoms can then abstract H from SiH_4 to produce another SiH_3. At low pressure, the rate of reaction of SiH_3 with other species is fairly low, and so silyl persists in the discharge. SiH_2 rapidly inserts into the SiH_4 to produce disilane, Si_2H_6, and so silylene is quickly consumed in regions where the SiH_4 density is high. The rate of consumption is $>10^{15}$ cm^{-3} s^{-1} in the vicinity of the powered electrode. SiH_2 will also rapidly insert into other saturated silanes, Si_nH_{2n+2}, to produce the next higher silane, $Si_{(n+1)}H_{2(n+1)+2}$. H atom abstraction from Si_2H_6 produces Si_2H_5 ($<10^{15}$ cm^{-3} s^{-1} in the electrode region). These differences in reactivity in large part explain the different spatial distributions of SiH_2 (small where the density of SiH_4 is still large), SiH_3 (extending to the inlet nozzle where SiH_4 is initially dissociated), and Si_2H_5 (large around the electrodes where the SiH_4 density is low).

The densities of H, H_2, H^-, and H^+ are shown in Fig. 3.7. The densities of H and H_2 have maximum values of 2.3×10^{13} cm^{-3} and 8.8×10^{13} cm^{-3}, respectively. H is predominantly produced through electron impact dissociation of SiH_4 while H_2 is largely produced by hydrogen abstraction from SiH_4. Both sources rely on SiH_4 and so the associated production rates are largest upstream of the electrodes prior to SiH_4 being fully dissociated. The H_2 density is larger than that of H due to the propensity of H atoms to participate in the H abstraction reactions (which decreases the H density) that produce H_2. The experimental H density was estimated from measurements of optical emission from plasma and is $\approx10^{13}$ cm^{-3} [49, 26]. H^- and H^+ densities peak along the centerline at the expansion of the tube, with values of 2.2×10^9 cm^{-3} and 2.8×10^{10} cm^{-3}, respectively. Both of these ions are produced by electron impact. H^+ is predominantly

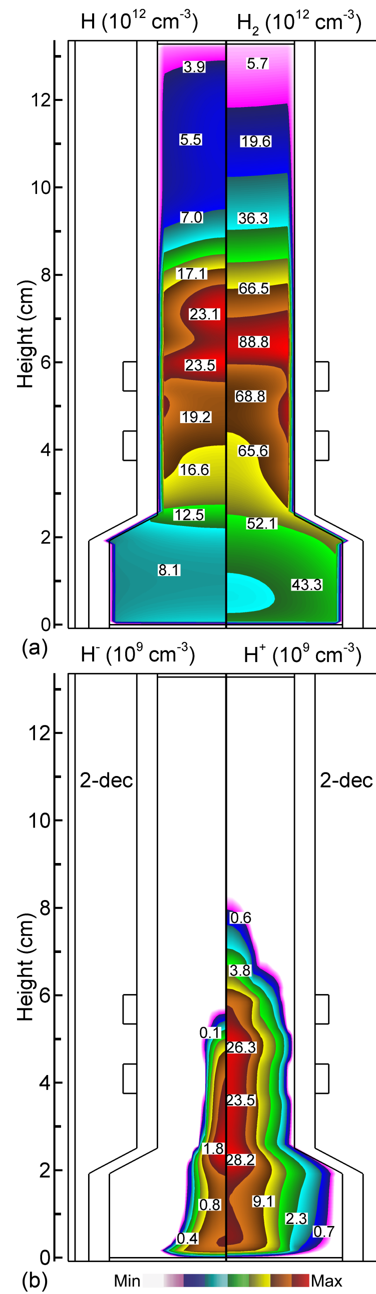

Figure 3.7: Atomic and molecular hydrogen densities for the base case conditions ($Ar/He/SiH_4$= 50/4.75/0.25, 1.5 Torr, 3 W, 50 sccm). (a) H and H_2, (b) H^- and H^+. Log-scale plots have number of decades noted.

produced by ionization of H, while H^- comes from dissociative attachment of H_2^+ (e + H_2^+ $\rightarrow H^-$ + H^+) [91]. Since atomic H is abundant in this system, the density of H^+ is greater than that of H^-. The H^- density peaks in the expansion zone, while H^+ is more spread between the electrodes due to the ambipolar electric field which accelerate positive ions towards the walls while confining the negative ions.

3.4.4 Nanoparticle Growth Mechanisms

All silicon hydride radicals play a role in the nucleation and surface growth of nanoparticles. However, based on the hierarchy of sticking coefficients, we expect SiH_2 and Si_2H_5 to be the dominant radicals contributing to surface growth, with SiH_3 playing a less important role. The density of $Si_2H_4^-$ peaks at 3.3×10^{10} cm^{-3} below the bottom electrode, while the $Si_2H_5^-$ density peaks at 8.0×10^{11} cm^{-3} between the two electrodes. Therefore, nucleation mostly occurs through the $Si_2H_5^-$ pathway. SiH_3^+, the only positive silicon hydride species we consider in the reaction mechanism, has a maximum density of 7.3×10^{10} cm^{-3} between the two electrodes.

The nucleation rate, surface growth rate, coagulation rate, and total nanoparticle density are shown in Fig. 3.8. The nucleation rate (defined as the rate of formation of silicon hydride anions containing 3 or more Si atoms) peaks at 4.5×10^{15} cm^{-3} s^{-1} between the two electrodes. $Si_2H_5^-$ is the dominant species for nucleation as its density is significantly higher than that of $Si_2H_4^-$. Nucleation in this mechanism is dominated by negative ion-molecule reactions, and the net axial electric field produces a drift of negative ions downward. Therefore, the local nucleation at the top of the tube must result from negative ions formed locally. The dominant reactions leading to particle nucleation are shown in Fig. 3.9a. $Si_2H_5^-$ reacts with SiH_4 in the upstream portion of the tube prior to SiH_4 being dissociated. As the density of Si_2H_6 increases, largely due to the consumption of SiH_4 through SiH_2 insertion, the reaction of Si_2H_6 then dominates. The nucleation and surface growth rates are both maximum near the center of the electrodes. The nucleation and surface growth are both closely coupled to electron impact collisions−either forming ions or radicals through dissociation. Since the electron density is maximum near the center of the electrodes, the nucleation and surface growth rates also peak at near the same location.

The overall surface growth rate average over all size-charge nanoparticles peaks at

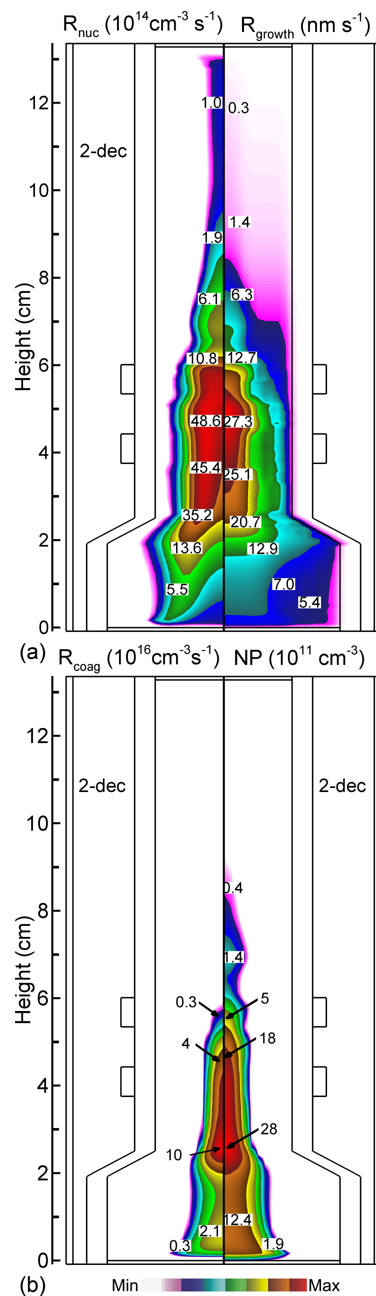

Figure 3.8: Nanoparticle growth mechanisms. (a) Nucleation rate and surface growth rate, (b) coagulation rate and total nanoparticle density. Log-scale plots have number of decades noted.

29.3 nm s^{-1} between the electrodes where the densities of radicals are maximum. The relative contribution of radical species to surface growth are shown in Fig. 3.9b. The dominant species contributing to surface growth is Si_2H_5 even though the densities of SiH_3 and SiH_2 are comparable to Si_2H_5. The sticking coefficient of SiH_3 is estimated to be 0.045, compared to a value of unity for Si_2H_5. But even for equal sticking probabilities, Si_2H_5 is assumed to add two Si atoms to particle surface and so will have a proportionately larger contribution compared to SiH_x. The rate of surface growth remains relatively high below and downstream of the bottom electrode in large part due to the convection of radicals produced in the more intense plasma between the electrodes. Based only on the surface growth rate, particles of a few nm would require many tens of ms to form, which considerably exceeds the gas residence time. Therefore, coagulation must play an important role in particle growth.

The total nanoparticle density is the sum of all nanoparticles regardless of size or charge and has a maximum value of 2.3×10^{12} cm^{-3} where the tube starts to expand. The total density is dominated by the larger density of the smallest particles. The particle size distribution along the centerline of the tube is shown in Fig. 3.10a. Nucleation predominantly occurs between the electrodes and particles grow while flowing towards the outlet. The evolution of the particle distribution along the centerline as a function of distance from the inlet is shown in Fig. 3.10b. The density of the smallest nanoparticles increases from 7 to 9 cm from the inlet as particles nucleate and flow through the tube. Their densities decrease from 9 to 11 cm from the inlet because of the expansion of the tube which leads to a spreading of the nanoparticle cloud by radial diffusion. (See Fig. 3.8b). From 11 to 12 cm from the inlet, the size distribution shifts to larger sizes as the nucleation rate drops (Fig. 3.8a) and particles grow.

Particle size distributions for negatively charged and neutral nanoparticles at the outlet on the centerline are shown in Fig. 3.11. The total density of negative nanoparticles is approximately one order of magnitude larger than for neutral nanoparticles over the range of particle sizes. The total coagulation rate is the sum of rates of coagulation between all possible combinations of particle charge and size, and is shown in Fig. 3.8b. This rate peaks at 1.2×10^{17} cm^{-3} s^{-1} on the centerline at the beginning of the expansion zone where the negative and neutral nanoparticle densities are the highest. By far the largest contribution to the coagulation rate is due to coagulation

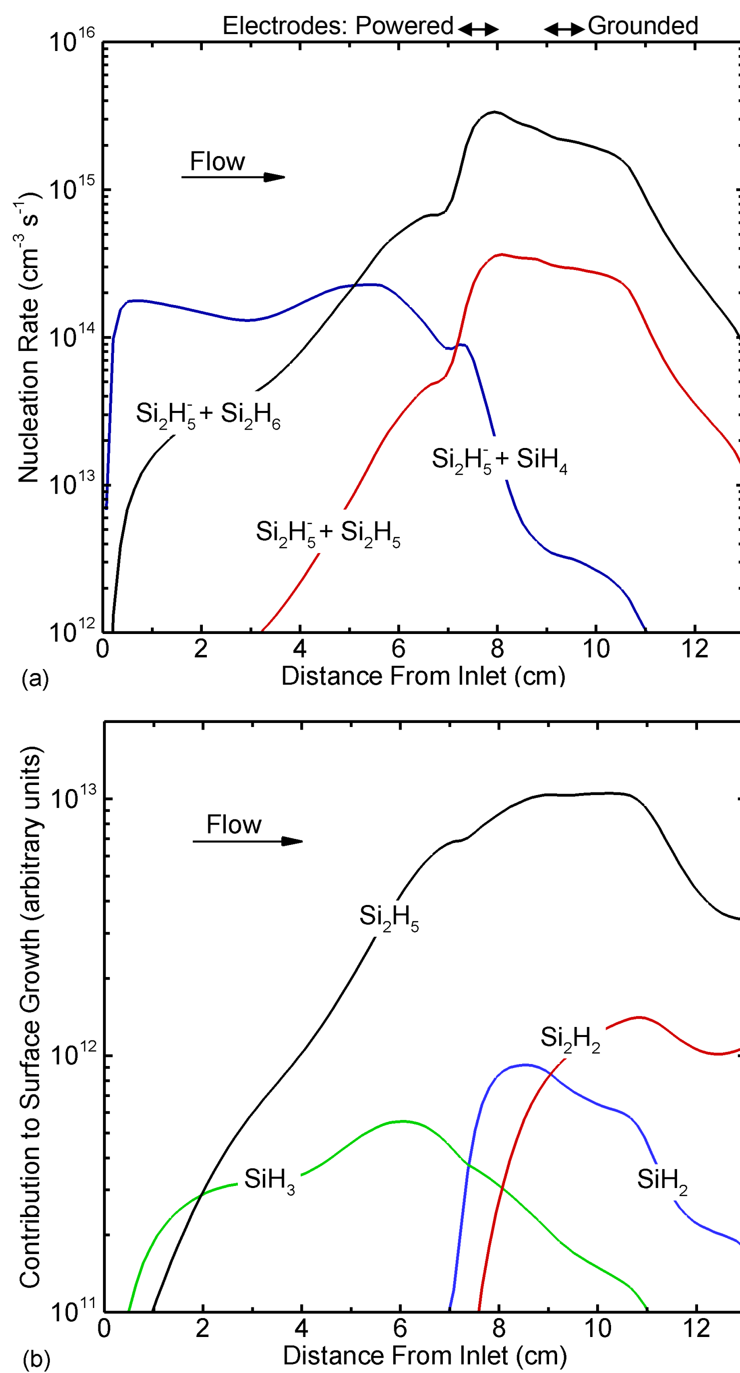

Figure 3.9: (a) Nucleation reaction rates for reactions involving $Si_2H_5^-$ species and (b) relative contribution of radical deposition on nanoparticle surfaces during surface growth.

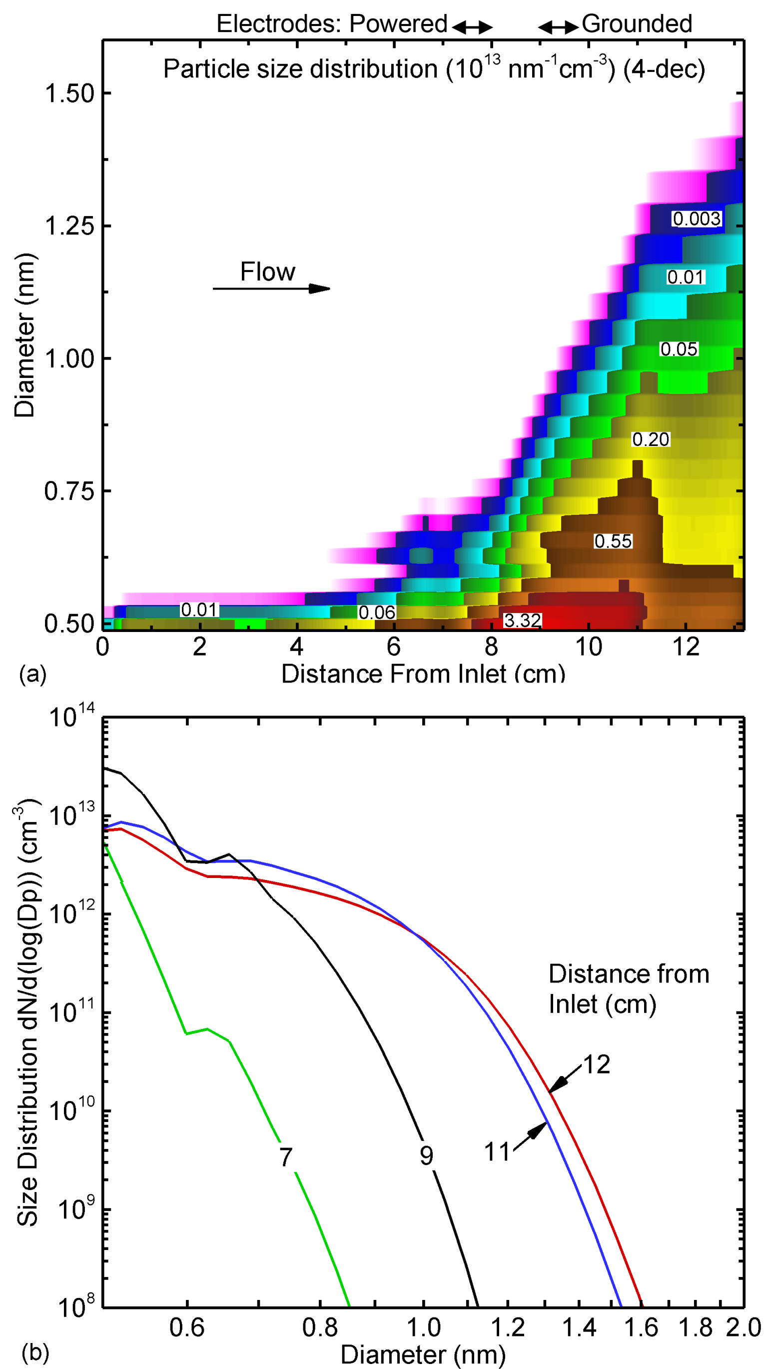

Figure 3.10: Nanoparticle size distributions on the centerline of the reactor (r=0). (a) Nanoparticle size distribution (cm^{-3} nm^{-1}) over 4 decades as a function of distance from the inlet, and (b) size distribution at 7, 9, 11, 12 cm from the inlet.

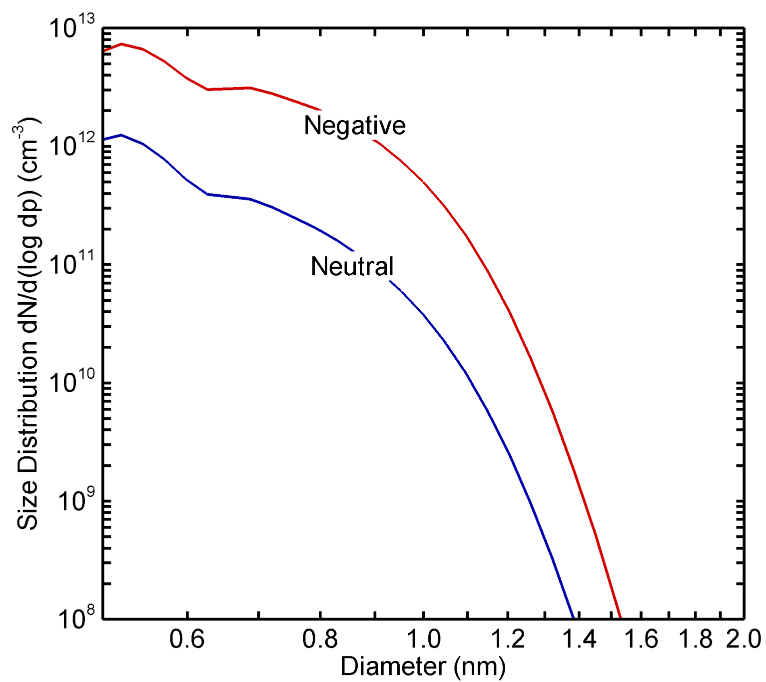

Figure 3.11: Size distributions for negatively charged and neutral nanoparticles at 11 cm from the inlet on the centerline.

between negative and neutral nanoparticles. Each such coagulation event consumes one neutral nanoparticle, while creating a larger negative nanoparticle. The typical average sizes observed in similar experiments are 1-3 nm [49, 27], and so our predictions here somewhat underestimate those particle sizes.

These discrepancies between the model and the experiments can be explain due to the following uncertainties. Particle size is measured using TEM, which cannot see NPs smaller than 1 nm. The actual power deposition in the plasma that occurs in the experiment is not accurately known (the reflected power is not measured). There is also some uncertainties in the values of the sticking coefficient of radicals onto nanoparticle surface. The best available values for those coefficients were used in this investigation, and so there is likely room for improvement in those values.

3.5 Nanoparticle Temperature and Crystallization

Experiments can produce both amorphous and crystalline silicon nanoparticles by tuning plasma conditions [49, 27]. The temperatures at which nanoparticle crystallization occurs are a sensitive function of size − for example, 773 K for 4-nm and 1,273 K for 10-nm-diameter particles [80]. However, these temperatures are well above the gas temperatures, that remains near room temperature, not exceeding 500 K. Experimental and numerical studies have shown that exothermic surface processes (e.g. ion recombination and hydrogen reactions) on nanoparticle surfaces could be responsible for crystallization by heating nanoparticles above their crystallization temperature [26, 27, 92]. Nanoparticle temperature here is intended to represent the particle's internal or bulk temperature, and is distinct from the particle's translational temperature.

To investigate the spatial dependence of the internal temperature of nanoparticles, a Monte Carlo model similar to that developed by Mangolini and Kortshagen [26] was implemented. The rate of change of the nanoparticle temperature is given by

$$\frac{4}{3}\pi R^3 \rho_p C_p \frac{dT_p}{dt} = G - L, \tag{3.19}$$

where ρ_p is the silicon mass density, C_p is the heat capacity, G is the rate of heating due to all surface processes, and L is the rate of cooling by thermal conduction to the gas. Using molecular dynamics simulations, Endo *et al.* have reported the mass density and

heat capacity of bare silicon particles for 100 - 3000 K temperatures and both amorphous and crystalline particles [93]. They found that the density of amorphous silicon is greater than that of crystalline silicon at temperatures below 1000 K and that the heat capacity of amorphous silicon is smaller than that of crystalline silicon at temperatures below 800 K but greater above 800 K. However, in the simulation conducted in this work, we assumed ρ=2.33 g cm^{-3} and C_p=0.712 J g^{-1} K^{-1}. One of the heating processes is recombination of argon ions with electrons on the surface of the particle, which delivers 15.6 eV of energy to the particle (the ionization potential of Ar). Hydrogen surface reactions include H atom passivation of dangling bonds, depositing 3.1 eV (the energy of the Si-H bond) into the particle; H-induced abstraction through the Eley-Rideal mechanism, depositing 1.41 eV; and physical adsorption of H, depositing either 3.1 eV (recombination with a dangling bond) or 4.51 eV (recombination with an incoming radical) [26]. The internal energy of the particle is mostly dissipated by thermal conduction with the background gas, which is mainly argon in this work. Statistical averages for particle temperatures at each numerical mesh point were obtained by following over 10^5 collisions with ions and H atoms with a nanoparticle. Nanoparticle transport is neglected in the model as the conduction time scale is small compared to the time scale for nanoparticle transport.

Using the Monte Carlo model, local plasma properties provided by the plasma hydrodynamics model were used to predict the nanoparticle internal temperature. The gas temperature produced by the plasma transport model and the internal temperature for 2-nm diameter particles are shown in Fig. 3.12. The gas temperature is the mole fraction-weighted average of the individual temperatures of neutral argon, helium, and silicon hydride species. The gas temperature peaks between the electrodes, at 440 - 450 K, where ion densities are largest, as the major source of gas heating is charge exchange with the hotter ions. Although the gas temperature exceeds ambient by as much as 100 K (the wall temperature is 325 K), the gas temperature remains well below the required crystallization temperature. These results are consistent with temperatures reported in experiments. We found that the average internal temperature of 2-nm particles peaks between the two electrodes at 866 K. The contribution of ion-recombination on the surface of particles to the internal temperature is larger than heating by hydrogen surface reactions by a factor of 5. Similar modeling by Kramer *et al.* showed that the

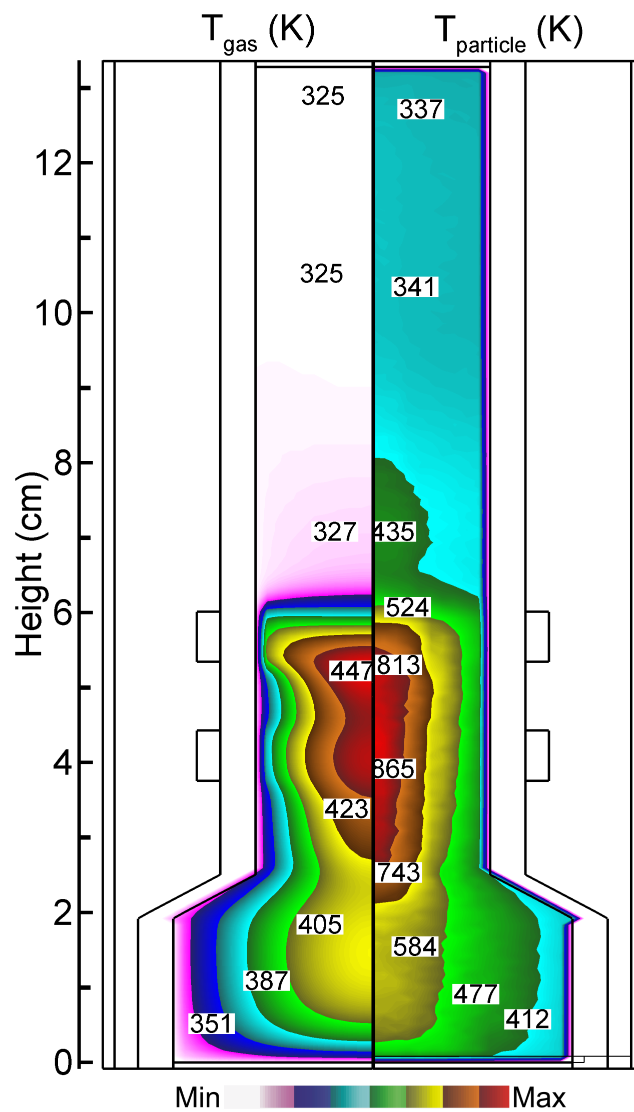

Figure 3.12: Temperatures for the base case conditions: (left) Gas temperature (325 K - 445 K) and (right) internal temperature (325 K - 866 K) for 2-nm diameter nanoparticles.

contribution of hydrogen reactions increases with nanoparticle size, because conditions that produce larger particles also generally produce larger H atom densities relative to ion densities [27]. For 3-nm diameter particles, they found that both mechanisms have similar contributions. In this work, the Ar^+ density (10^{12} cm^{-3}) is about an order of magnitude larger than indicated by electrostatic capacitive probe measurements, while the hydrogen density is comparable. Because of the high ion density, the electron-ion recombination rate on nanoparticle surface is greater than the hydrogen surface reaction rate. This explains the larger contribution of electron-ion recombination to internal temperature for 2-nm particles, which is more than 400 K higher than the gas temperature and exceeds the crystallization temperature. The results of the model therefore predict the possibility of synthesizing crystalline silicon nanoparticles under these conditions. The contribution of electron-ion and hydrogen processes on nanoparticle surface as function of the power deposition is shown in Fig. 3.13.

3.6 Concluding Remarks

In this investigation, we developed a two-dimensional numerical model of a capacitively-coupled RF plasma used for the synthesis of silicon nanoparticles. A sectional model was used to self-consistently calculate rates of nucleation and radical deposition on the surfaces of the nanoparticles. Coagulation processes were included with algorithms for the distribution of nanoparticle charge and transport.

We found that silane dissociation occurs dominantly by hydrogen abstraction above the electrode, and electron impact reactions around and below the powered electrode. The predominant anion for initiating nanoparticle nucleation was found to be Si_2H_5 reacting with disilane, the latter of which is produced by insertion of SiH_2 into SiH_4. The greatest contribution to surface growth is neutral radicals since the majority of nanoparticles are negatively charged, which precludes anion-anion interactions. Coagulation is a significant growth mechanism due to the existence of neutral NPs and to dipole interactions between charged and neutral NPs.

Electron temperatures are sufficiently high (3.5 eV) throughout the discharge to produce nanoparticles that are dominantly negatively charged. The wall potential is

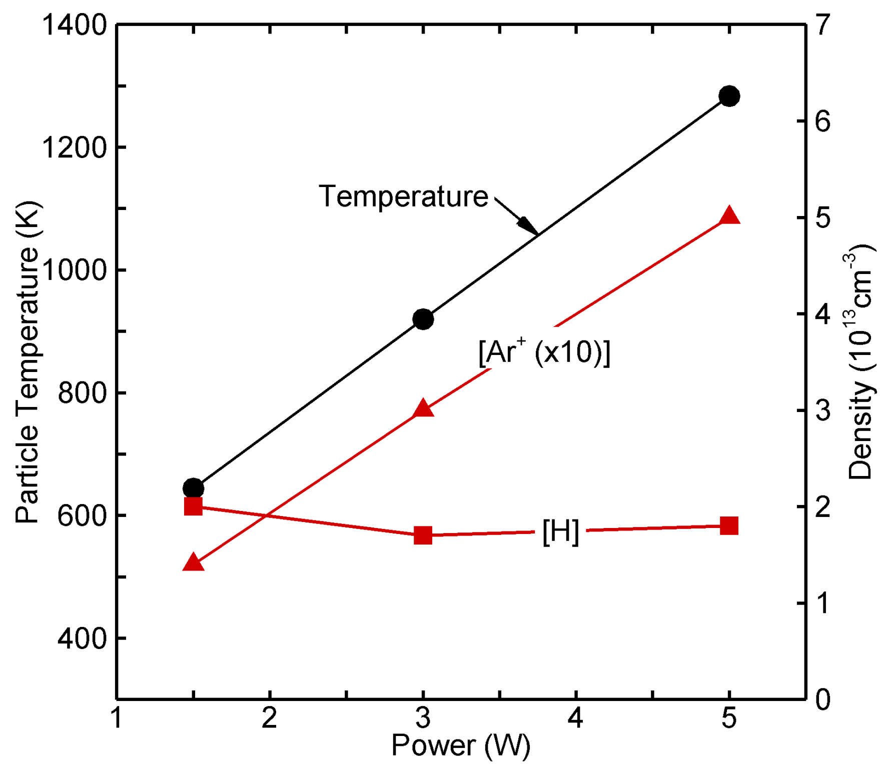

Figure 3.13: Particle temperature calculated from Monte Carlo simulations, and hydrogen and argon ion densities as function of power. Results are at 4 cm from the outlet on the centerline which is near where the particle temperature peaks.

lower than the plasma potential which radially traps negative particles, further increasing their density on the centerline compared to neutral nanoparticles, which can diffuse radially. However, the negative particles are not trapped in the axial direction. The model predicts that internal temperatures can be a few hundred Kelvin greater than the gas temperature and commensurate with or above the nanoparticles' crystallization temperatures.

The experiment produces particle size in the range 2-3 nm in diameter, while the model presented in this chapter predicts particle smaller than 1 nm in diameter. The discrepancies between the experiment and the model may be explained by computational limitations. Because of the large number of equations to solve at once, (e.g., continuity and momentum equations) one simulation took more than four months, and the steady-state solution was not fully reached. However, if we were to run the code for much longer, we would not expect significant qualitative differences with the current results, while the magnitude of certain variables (e.g., species and nanoparticle densities) may change.

Chapter 4

The Effect of Single-Particle Charge Limits on Charge Distributions in Dusty Plasmas

This chapter is based on R. Le Picard and S. L. Girshick, "The effect of single-particle charge limits on charge distributions in dusty plasmas," *Journal of Physics D: Applied Physics*, **49**(9):095201, 2016 [70].

The stochastic and discrete nature of particle charging becomes significant as particle size decreases. Particles exhibit a charge distribution with negative, neutral, and positive charge states, which have significant effects on particle growth mechanisms and transport. At small particle size, the maximum number of electrons that can coexist on a single particle is limited−referred to as its *charge limit*. In this chapter, we present the effect of single-particle charge limits on charge distributions. We first review the evidence of particle charge limits as well as some useful mathematical expressions. We derive an analytical expression for the charge distribution accounting for particle charge limits and validate it by comparison with a stochastic numerical charging model. Finally we present the effect of charge limits on charge distributions under typical low-pressure plasma conditions.

4.1 Introduction

The stochastic nature of particle charging in plasmas causes a population of dust particles of given size to exhibit a distribution of charge states. A number of previous investigators have analyzed the form of this distribution. However none of these studies accounted for the fact that the amount of charge a dust particle can hold is limited. On the other hand, several studies involving numerical modeling of particle formation and growth in plasmas did account for the existence of particle charge limits [7, 5, 12, 11, 13], but these studies did not address the more general question of how charge limits affect charge distributions.

The primary purpose in this chapter is thus to examine the effect of charge limits on particle charge distributions in dusty plasmas. Assuming that charging is dominated by collisional processes (i.e., attachment of electrons and ions by collisions with dust particles), the higher mobility of electrons than of ions causes dust particles in plasmas under most conditions to be predominantly negatively charged. Hence we here consider only negative charge limits, in particular the maximum number of electrons a particle can hold, and we focus on particles with sizes in the nanoscale regime, where stochastic charging is most important and the existence of charge limits is likely to be most consequential.

Cui and Goree used a Monte Carlo (MC) model to analyze charge fluctuations on dust particles in a plasma [71]. They showed that the root-mean-square charge fluctuation varies as $dq = 0.5(\bar{q})^{-1/2}$, where $\bar{q}$ is the mean charge, and that power spectra of the fluctuations are dominated by low ($\sim$kHz) frequencies. Stochastic charging in low-pressure plasmas was described by Matsoukas and Russell as a one-step Markov process whose continuous form could be cast as a Fokker-Planck differential equation where the convective and diffusive terms are functions of electron and ion currents to the particle [46, 94]. Assuming that particle charging follows orbital motion limited (OML) theory [8], they showed that in the stationary case, where electron and ion currents to dust particles balance each other, the charge distribution has a Gaussian form, provided that the average charge is not too small. Shotorban extended the analytical solution to the non-stationary case [95]. The dynamic behavior of particle charge fluctuations was studied by Khrapak *et al.*, who added the effects of thermionic emission and

photoemission processes from particles [96]. Gordiets and Ferreira studied the effect on charge distributions of secondary electron emission [97]. Draine and Sutin studied charge distributions on interstellar grains [98]. They noted the existence of charge limits due to electron field emission, but did not account for these in their analysis of charge distributions.

Here we derive an analytical expression for the stationary particle charge distribution that accounts for the existence of charge limits, and compare this expression with numerical simulations that employ an MC charging model. Results are shown for typical low-pressure plasma conditions. As a particle's charge limit depends only on its size and the material of which it is composed, rather than on the plasma environment, results can be extended to a variety of plasma conditions. We show that the extent to which the existence of charge limits affects charge distributions depends strongly on the ratio n_e/n_i. Additionally we consider the effect of ion mass on the importance of charge limits, and consider the effect of charge limits on the temporal behavior of particle charge distributions, including both the time required to reach a steady-state distribution and the power spectrum of charge fluctuations.

4.2 Review of Single-Particle Charge Limits

In this section, we briefly review expressions in the literature for the values of charge limits of solid particles due to various pertinent effects.

The finite surface tension of liquid droplets imposes a limit, known as the Rayleigh limit, to the number of charges that a droplet can hold [99]. As the charge increases, Coulomb repulsion finally becomes greater than the surface tension, causing the droplet to break up. Doyle *et al.* have conducted experiments on evaporating liquid charged particles ($60-200$ μm) [100]. As the droplet size decreased because of the evaporation, the electric charge density on its surface increased up to a critical value, producing smaller droplets with smaller number of electric charges. This observation was in good agreement with the Rayleigh limit. Here we focus on solid particles, for which the surface tension is much higher than for liquids, and other phenomena impose more stringent charge limits.

The main phenomena that limit the number of electrons that a solid particle can

hold are electron field emission, which is independent of particle material, and material dependent electron affinity.

Electron field emission is the spontaneous emission of electrons from a negatively-charged particle if the self-generated electric field at the particle surface exceeds a critical value. This value is on the order of $\sim 10^7$ V cm^{-1} [101], for which Draine and Sutin determined that the maximum number $|q_E|$ of negative charges a particle can hold is given by

$$|q_E| = 1 + 0.7\Big(\frac{R}{1\ \text{nm}}\Big)^2, \tag{4.1}$$

where R is the particle radius [98].

The work required to remove an electron from a particle, i.e., its electron affinity, is affected by surface curvature as well as by Coulomb repulsion due to pre-existing negative charges on the particle. Thus a charged spherical nanoparticle with $|q|$ electrons attached has an effective electron affinity that differs from the value for the bulk (flat) neutral material, and this imposes another charge limit, determined by the condition that for an additional electron to attach to the particle the effective electron affinity cannot be negative.

Accounting for these effects, the electron affinity A of a particle is given by

$$A = A_\infty - \frac{5}{8}\frac{e^2}{\pi\varepsilon_0 R} - \frac{(|q|-1)e^2}{4\pi\varepsilon_0 R}, \tag{4.2}$$

where A_∞ is the electron affinity of the bulk neutral material [18].

The corresponding charge limit $|q_A|$ is obtained by setting A to zero, giving

$$|q_A| = \Big(\frac{4\pi\varepsilon_0 A_\infty}{e^2}\Big)R + \frac{3}{8}. \tag{4.3}$$

More detailed models have been proposed in the literature for the effective electron affinity and corresponding charge limit of semiconductor nanoparticles, that introduce a dependence on the relative permittivity of the particle material [7, 18].

Fig. 4.1 shows negative charge limits for bare silicon nanoparticles (A_∞=4.05 eV) given by Eqs. (4.1) and (4.3) as well as by Gallagher's model for silicon [7], in which the charge limit is proportional to $R^{1/2}$. As charge is an integer quantity, these expressions are all converted here to integer form. That is,

$$\text{if} \quad Z \leq |q_{E,A}| < Z+1, \quad \text{then} \quad q_{lim} = Z, \tag{4.4}$$

where Z is a non-negative integer and $q_{E,A}$ is the magnitude of the charge limit given by Eqs. (4.1), (4.3), or other suitable expression.

Taking Eq. (4.3) as the governing expression, one notes that for particles of given size $q_{lim} \propto A_{\infty}$, except for cases where the charge limit is small enough that the term 3/8 contributes significantly. For example, the bulk electron affinity of SiO_2 equals 1.0 eV, approximately four times smaller than the value for pure Si. Therefore the charge limit of SiO_2 particles would be four times smaller (or corresponding integer value given by equation (4.4)) than for Si, for particles of the same size.

Bouchoule and coworkers reported the temporal evolution of electron temperature along with particle density, average diameter, and average charge at a pressure of 117 mTorr, flow rate of Ar/SiH_4 (with 4% SiH_4) at 31.2 sccm, and RF power of 10 W in a parallel-plate capacitively-coupled RF plasma reactor [102, 81]. After 5 s, particles grow up to 42 nm in diameter, the electron temperature is 5 eV, the particle average charge is -49, the particle density is 10^8 cm^{-3}, the ion density is 1.5×10^9 cm^{-3}, and the electron density is 5×10^8 cm^{-3}. Under these conditions, and using a Monte Carlo numerical charging model (as described in Section 4.3), we calculated the following particle average charge: -96.6 (without charge limit) and -58.4 (with charge limit). The average particle charge measured experimentally is similar to the charge limit calculated using Eq. (4.3).

4.3 Analytical Expression for Stationary Particle Charge Distribution Accounting for Existence of Charge Limits

We assume that dust particles are charged only by electron and ion attachment, and we apply OML theory, which assumes that dust particle radii are much smaller than the Debye length [8]. Such assumptions are particularly valid in low-pressure plasmas containing particles of a few nanometers in size. Additionally we assume that particles are electrically isolated from each other. Thus the work presented in this chapter can be taken as a correction to previous work that makes these same assumptions but which neglects the existence of particle charge limits. A more accurate description under some conditions will require that one accounts for additional charging mechanisms,

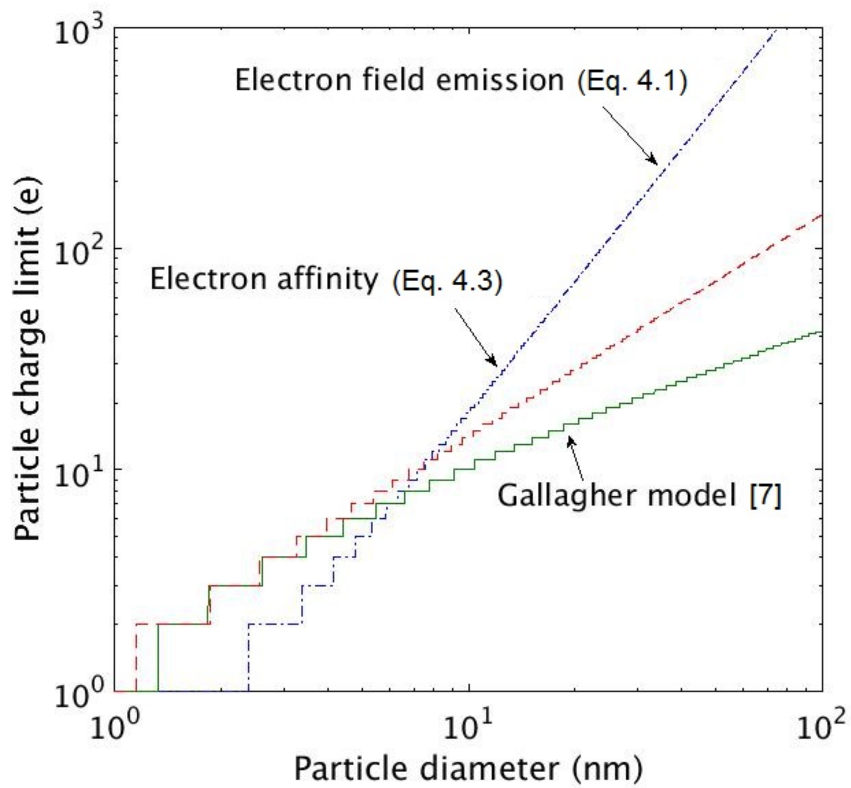

Figure 4.1: Charge limits for bare silicon nanoparticles based on electron field emission, Eq. (4.1), and particle electron affinity given by either Eq. (4.3) or [7], all shown in integer form.

deviations from OML theory for electron and ion currents to dust particles, electrostatic interactions of dust particles with each other, electron emission process, and ion collision with the background gas in the vicinity of the particle. Some of these processes are discussed in Chapter 5.

OML theory gives continuous expressions for electron (I_e) and ion (I_i) currents to particles as a function of particle charge q. In typical low-pressure plasmas, the thermal velocity of electrons is greater than of negative ions by a factor of $\sim$100, due to the higher electron mobility. Therefore the negative ion current to a particle is neglected here because its contribution to particle charging is smaller than that of electrons. For Maxwellian energy distributions, these currents are given by

$$I_x(q) = \left\{ \begin{array}{ll} I_{x0}\exp\left(\dfrac{q_x e^2}{4\pi\varepsilon_0 RkT_e}q\right), & q_x q \geq 0 \\ I_{x0}\left(1 - \dfrac{q_x e^2}{4\pi\varepsilon_0 RkT_e}q\right), & q_x q < 0 \end{array} \right\}, \tag{4.5}$$

where

$$I_{x0} = \pi R^2 s_x n_x \sqrt{\frac{8kT_x}{\pi m_x}}. \tag{4.6}$$

Here $x \equiv e, i$ for electrons and ions, respectively, with q_x representing the charge ($q_e = -1$, $q_i = +1$), s_x the sticking coefficient, T_x the temperature, m_x the mass, n_x the number density, k the Boltzmann constant, e the elementary charge, and ε_0 the vacuum permittivity [103].

Based on these currents, Matsoukas and Russell derived an analytical solution for the stationary particle charge distribution under the assumptions that $4\pi\varepsilon_0 R^2/e^2 \ll 1$ and that the average particle charge is not too small [46, 94]. They showed that the distribution function for particle charge can be approximated by a normalized Gaussian distribution,

$$n(q) = \frac{1}{\sigma\sqrt{2\pi}}\exp\Big[-\frac{1}{2}\Big(\frac{q-\bar{q}}{\sigma}\Big)^2\Big], \tag{4.7}$$

where $\bar{q}$ is the average particle charge, σ is the standard deviation of the distribution, and

$$\int_{-\infty}^{+\infty} n(q)dq = 1. \tag{4.8}$$

For Maxwellian electron and ion energy distributions,

$$\bar{q} = C\frac{4\pi\varepsilon_0 RkT_e}{e^2}\ln\Big[\frac{s_i n_i}{s_e n_e}\Big(\frac{m_e T_e}{m_i T_i}\Big)^{1/2}\Big], \tag{4.9}$$

and

$$\sigma^2 = \frac{4\pi\varepsilon_0 RkT_e}{e^2}\Big(1 - \frac{T_e}{T_e + T_i - \frac{e^2}{4\pi\varepsilon_0 Rk}\bar{q}}\Big), \tag{4.10}$$

σ^2 being the variance of the distribution. In Eq. (4.9), C is a constant that is weakly dependent on plasma parameters and independent of particle size. For argon plasmas over a wide range of temperatures, $C = 0.73$ [46].

The Gaussian particle charge distribution defined by Eqs. (4.7)−(4.9) does not account for the existence of particle charge limits, and thus it assigns a non-zero probability to a particle having a charge that is more negative than its charge limit ($-q_{lim}$). Here we propose a correction to Eqs. (4.7)−(4.9) to account for the existence of charge limits.

To obtain an expression for the corrected charge distribution $n^*(q)$, we normalize $n(q)$ with the negative charge limit as a lower bound on q. Let the correction factor ζ be defined by the relation

$$\zeta \int_{q'_{lim}}^{\infty} n(q)dq = 1, \tag{4.11}$$

where the lower limit of integration q'_{lim} is given by

$$q'_{lim} = -q_{lim} - 0.5, \tag{4.12}$$

and $n(q)$ is the uncorrected particle charge distribution function given by Eq. (4.7).

The term 0.5 in Eq. (4.12) corrects for the fact that the number of charges on a particle is treated in Eq. (4.11) as a continuous variable whereas in reality it is integer. Thus each integer charge Q is centered within a charge interval of width equal to unity, and the probability that a particle has charge Q is given by

$$\int_{Q-1/2}^{Q+1/2} n^*(q)dq. \tag{4.13}$$

Solving Eq. (4.11) using integral I_1 in Appendix A, the correction factor is found to be given by

$$\zeta = \frac{2}{1 + \mathrm{erf}(\frac{\bar{q}-q'_{lim}}{\sqrt{2}\sigma})}. \tag{4.14}$$

Thus the corrected particle charge distribution function, accounting for the existence of charge limits, can be written as

$$n^*(q) = \frac{2}{1 + \mathrm{erf}(\frac{\bar{q}-q'_{lim}}{\sqrt{2}\sigma})} H(q - q'_{lim})n(q), \tag{4.15}$$

where $n(q)$ is given by Eq. (4.7), $\bar{q}$ by Eq. (4.9), q'_{lim} by Eq. (4.12), σ is obtained from Eq. (4.10), and H is the Heaviside step function, where $H(x) = 1$ for $x \geq 0$ and $H(x) = 0$ for $x < 0$.

The corresponding average particle charge and variance, for the distribution accounting for the existence of charge limits, are then obtained from

$$\bar{q}^* = \int_{q'_{lim}}^{\infty} q n^*(q) dq \tag{4.16}$$

and

$$\bar{\sigma}^{*2} = \int_{q'_{lim}}^{\infty} (q - \bar{q}^*)^2 n^*(q) dq. \tag{4.17}$$

If the magnitude of the charge limit is much greater than the average number of negative charges in the absence of charge limits ($q_{lim} \gg |\bar{q}|$), then the existence of the charge limit barely constrains the charge distribution. This is confirmed by inspection of Eqs. (4.14) and (4.15), which indicates that in this regime the existence of charge limits has negligible effect: $\zeta \to 1$ and $n^*(q) \to n(q)$.

The average charge and variance in the case of charge limits can be written

$$\bar{q}^* = \bar{q} + \Delta q \tag{4.18}$$

and

$$\bar{\sigma}^{*2} = \sigma^2 + \Delta(\sigma^2), \tag{4.19}$$

where Δq and $\Delta(\sigma^2)$ are corrections that must be made to the average particle charge and variance to account for the existence of charge limits.

Using integrals I_2 and I_3 in Appendix A, respectively, we obtain

$$\Delta q = \frac{1}{\sqrt{2\pi}} \frac{2\sigma}{1 + \mathrm{erf}(\frac{\bar{q} - q'_{lim}}{\sqrt{2}\sigma})} \exp\Big[-\frac{1}{2}\Big(\frac{\bar{q} - q'_{lim}}{\sigma}\Big)^2\Big], \tag{4.20}$$

and

$$\Delta(\sigma^2) = (\Delta q)^2 + (\bar{q} - 2\bar{q}^* + q'_{lim})\Delta q. \tag{4.21}$$

In this derivation, we assume that it is impossible for an electron to attach to a particle that has reached its charge limit. This produces a sharp cutoff in the charge distribution at the charge limit as shown in Sec. 4.4. We assume that once the surface electric field is greater than the critical electric field for electron emission, an electron

is instantaneously emitted. This implies that the time scale for electron emission, τ_{em}, is much smaller than the time between two electron collisions with the particle τ_e (i.e., $\tau_{em} \ll \tau_e$). Under typical low-pressure plasma conditions, $\tau_e > 10^{-6}$ s. A second important assumption is that particles are perfectly spherical and uniform−because of non-uniformity, the effective electron affinity and surface electric field would vary at different locations on the particle surface. Accounting for such non-uniformity effects would probably smooth the charge distribution in the vicinity of the charge limit. Because of the complexity of such effects for semiconductor particles compared to metal particles, they were not considered in the current work.

4.4 Test of Validity of Analytical Expression

As a test of these analytical expressions, we conducted MC simulations for 5 and 10 nm-diameter particles in an argon plasma ($m_e/m_i = 1.37 \times 10^{-5}$) with $n_e/n_i = 1$, T_e =3 eV, and T_i =300 K. The MC model is the same as used by Cui and Goree [71], except that the electron sticking coefficient s_e is set to zero when the magnitude of the (negative) charge equals the charge limit. Particle composition was unspecified; instead the value of the charge limit was taken as a free parameter.

Figures 4.2 and 4.3 show comparisons of the analytical expression for the charge distribution, Eq. (4.15), with MC simulations that each involved 2×10^7 collisions of electrons and ions with a nanoparticle. Fig. 4.2 shows results for 5-nm-diameter particles and Fig. 4.3 for 10-nm-diameter particles. For particles of each sizes in Figs. 4.2 and 4.3 the top graph shows the case without charge limits (denoted $q_{lim} = \infty$), the middle graph shows the case where q_{lim} is somewhat greater than the magnitude of the average charge $\bar{q}$ without charge limits, and the bottom graph shows a case where q_{lim} is much smaller than the magnitude of $\bar{q}$. The analytical expression is seen to agree quite well with the MC simulations for all cases shown. Note that the results with charge limit do not represent a simple truncation of the Gaussian distribution without charge limits, but a truncation together with a redistribution of charge states, according to Eq. (4.15).

Another way to characterize the agreement between the analytical expression and the MC simulations is to compare the average charge and standard deviation predicted

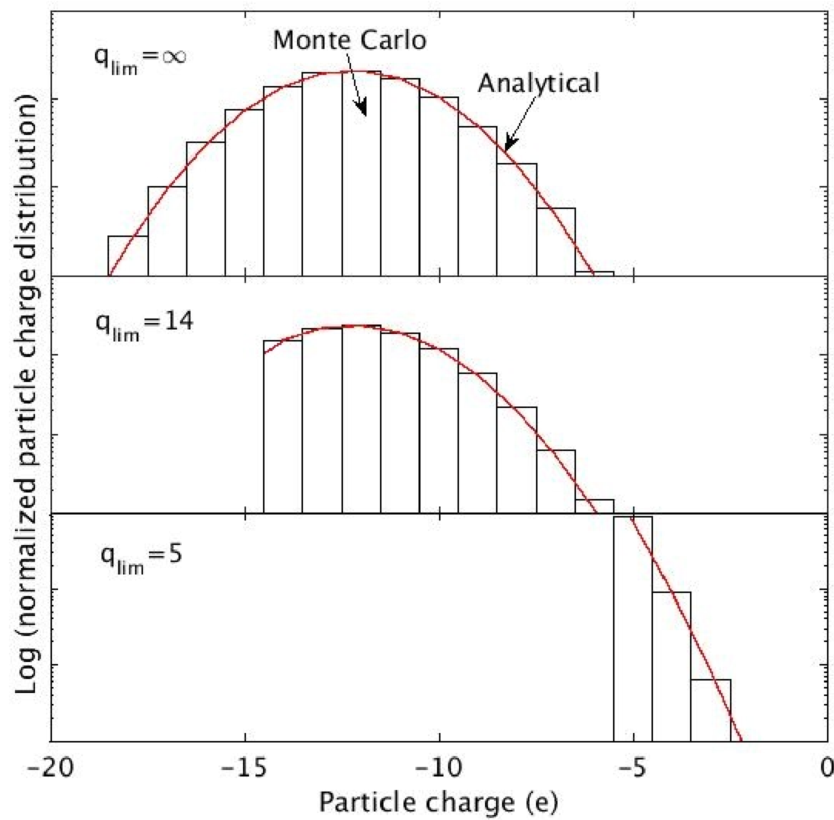

Figure 4.2: Comparison of analytical expression, Eq. (4.15) (solid lines), with Monte Carlo simulations (histograms) for three different values of charge limit, for argon plasma with $n_e/n_i = 1$, T_e =3 eV, and T_i =300 K. Particle diameter = 5 nm.

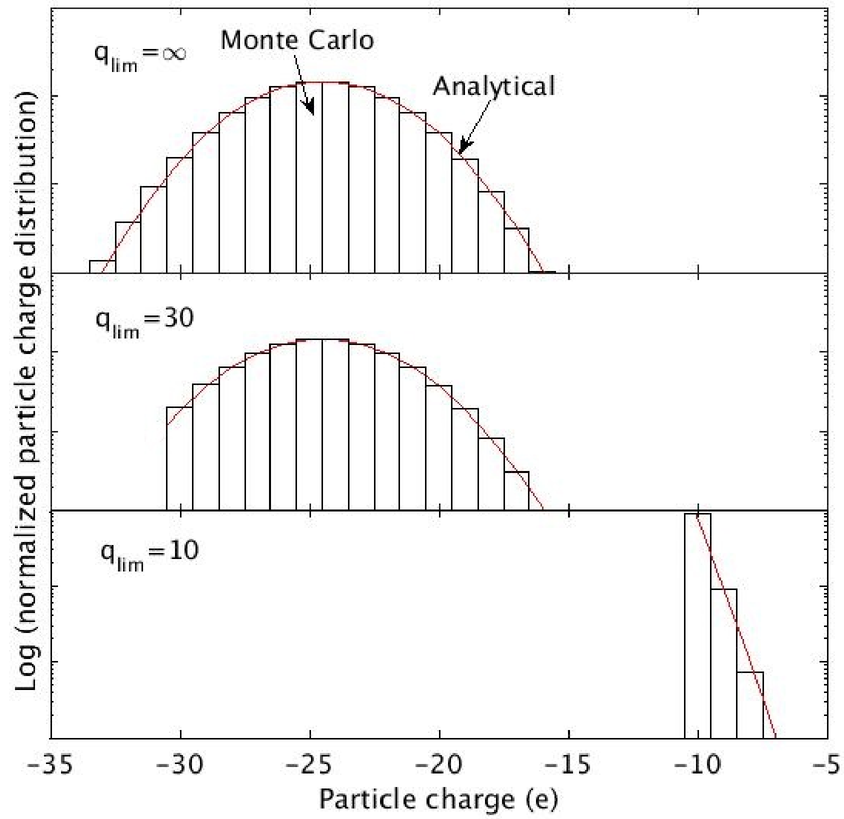

Figure 4.3: Comparison of analytical expression, Eq. (4.15) (solid lines), with Monte Carlo simulations (histograms) for three different values of charge limit, for argon plasma with $n_e/n_i = 1$, T_e =3 eV, and T_i =300 K. Particle diameter = 10 nm.

by the two methods. These comparisons, for 10-nm-diameter particles, for which the average charge $\bar{q}$ without charge limits equals -24.5, are shown in Fig. 4.4. Accounting for the existence of charge limits the results for average charge (Fig. 4.4 (top)) show excellent agreement between the analytical expression and MC simulations over the entire range of values of charge limit shown.

Fig. 4.4 also shows that for values of q_{lim} greater, in this case, than about 30, the average charge and standard deviation become independent of the value of the charge limit. In this regime, where the charge limit is significantly greater than the average charge $\bar{q}$ without charge limits, the existence of charge limits has only a small effect on the charge distribution−both average charge and standard deviation are virtually unaffected by the existence of charge limits. However, as the value of q_{lim} is reduced so that it is of the same order or smaller than $\bar{q}$, the effect of charge limits becomes increasingly apparent.

With respect to the standard deviation of the charge distribution, Fig. 4.4 (bottom), the analytical expression agrees well with the MC simulations for values of q_{lim} greater than about 20, but then deviates increasingly as q_{lim} is decreased. This discrepancy, while small in absolute terms−it is much less than the elementary charge e−results from the fact that as the average charge approaches zero the assumptions underlying the derivation of Eq. (4.7) are violated, and the charge distribution is expected to deviate from a Gaussian form, as discussed in appendix B of [46]. The MC simulations, of course, make no assumption regarding the form of the charge distribution.

4.5 Effect of Electron Depletion

The attachment of electrons to dust particles can cause the electron density to become much lower than the positive ion density. For example, recent experiments measured a three-fold depletion in electron density relative to ion density in an argon-silane plasma [82], and recent self-consistent numerical simulations of dusty plasmas indicate that under some circumstances the positive ion density in the bulk plasma can exceed the electron density by up to a factor of several hundred [11]. The use of electronegative gases (e.g., SiH_4, SF_6, and O_2 are widely used in the semiconductor industry) can also induce low electron density. Interestingly, this feature can mitigate the extent to which

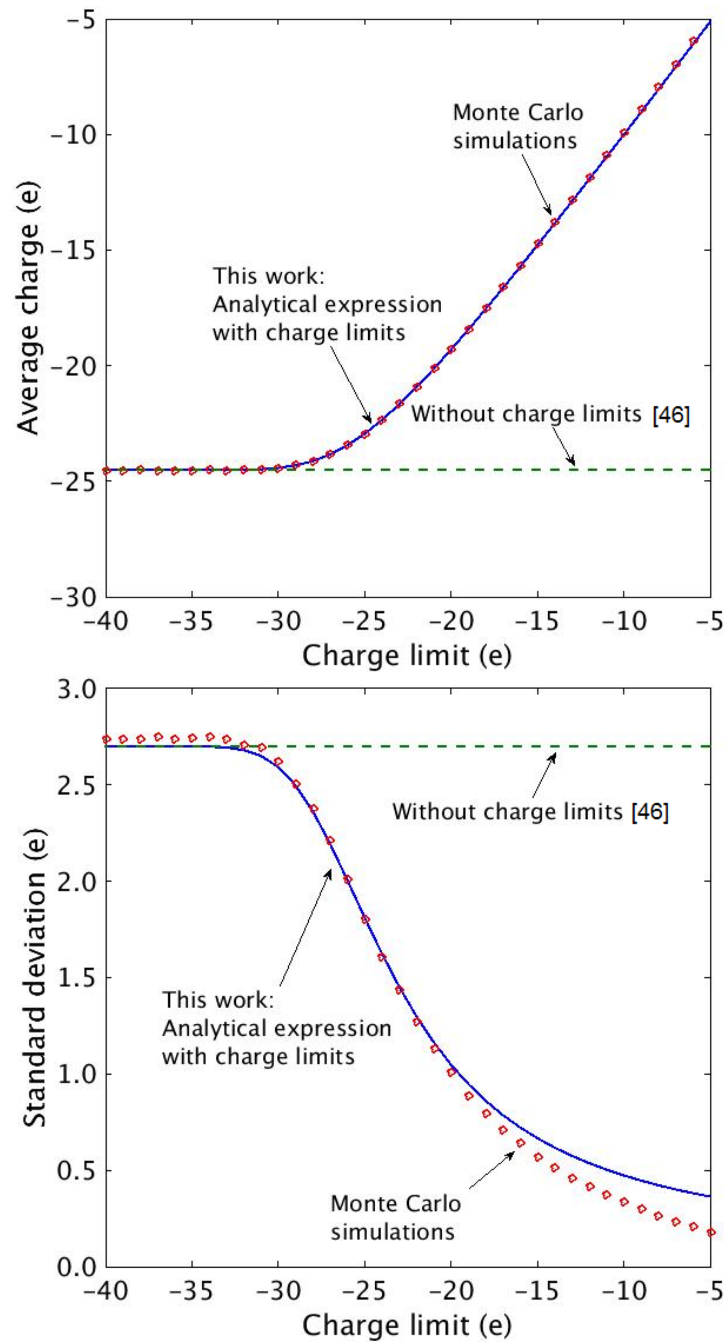

Figure 4.4: Charge distribution as a function of charge limit for 10-nm-diameter particles in an argon plasma with $n_e/n_i = 1$, T_e =3 eV, and T_i =300 K. (Top) average charge, (bottom) standard deviation.

the existence of charge limits perturbs particle charge distributions, because the relative paucity of free electrons acts to limit particle charge even in the absence of inherent charge limits.

To explore this effect we conducted MC simulations for various values of n_e/n_i. Fig. 4.5 shows results for 10 nm-diameter silicon particles for the same conditions as in Fig. 4.3, except n_e/n_i is allowed to vary, and the charge limit is set equal to 14, as given by Eq. (4.3). We consider three values of n_e/n_i: 1, 0.25, and 0.01.

For the case $n_e = n_i$, without charge limits, the charge distribution is well represented by the Matsoukas and Russell expression [46, 94], with an average charge of -24.5. However, accounting for the charge limit, which here equals -14, the true charge distribution must obviously be completely different. With electrons as abundant here as positive ions, particles bunch into the charge state given by $-q_{lim}$. In this case, the simulation indicates that 80.4% of the particles exist in this charge state, with the other 19.6% of particles distributed into charge states that are less negative.

For the case $n_e/n_i = 0.25$, the reduced abundance of electrons relative to ions causes the distribution without charge limits to become less negative. The peak in this distribution is seen to be located at a charge of -15, close to the charge limit of -14. The distribution with charge limits is now seen to be rather close to that without charge limits, except that the former is truncated at the value of the charge limit. The bunching of particles into the charge state given by $-q_{lim}$ is now less pronounced, with only 36.2% of the particles located in this charge state, according to the MC simulation results.

When electrons are more severely depleted, the existence of charge limits begins to make little difference in the charge distribution, because there are not enough electrons per positive ion to charge particles to their limit. Thus, for the case $n_e/n_i = 0.01$, the distributions with and without charge limits are seen to be virtually identical. Even without charge limits the distribution is shifted far toward positive values−indeed, a non-negligible fraction of the particles are neutral or positively charged−and effectively no particles are charged to their limit. Therefore the existence of charge limits in this case makes negligible difference in the charge distribution. However, it is worth noting that in this case the charge distribution deviates from a Gaussian distribution, with or without charge limits, because the assumptions involved in the derivation of Eq. (4.7)

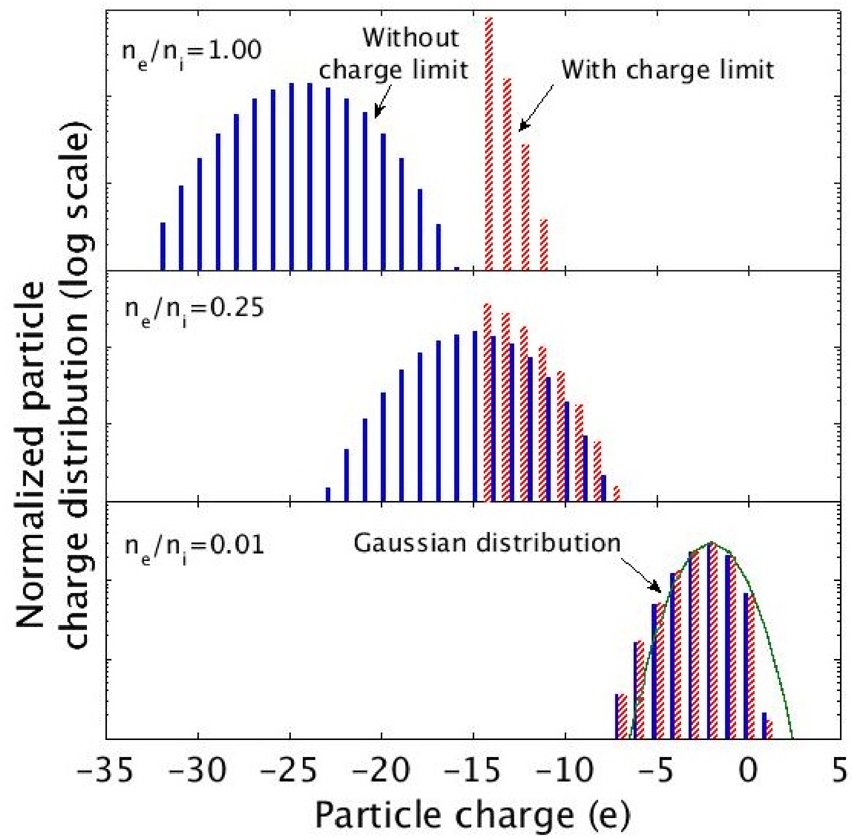

Figure 4.5: Results of Monte Carlo simulations for 10 nm-diameter silicon particles, with or without charge limits, for the same plasma conditions as in Fig. 4.2 except that n_e/n_i is varied. The solid line in the bottom graph shows Gaussian distribution predicted without charge limits, Eq. (4.7).

are no longer satisfied [46]. Additionally it should be noted that in this case, where the requirement of overall charge quasi-neutrality implies that the density of negative charge carried by dust particles is almost as large as the positive ion density, the assumption that particles are electrically isolated from each other is likely to be violated, leading to particles being less negatively charged, on average, than the isolated-particle case [18].

4.6 Effect of Ion Mass

From Eq. (4.9), without accounting for the existence of charge limits, the average particle charge $\bar{q} \propto \ln(m_e/m_i)^{1/2}$. Therefore, even though the ion mass makes no difference in the value of the charge limit, it can make a difference in the extent to which the existence of charge limits perturbs the charge distribution. For example, Fig. 4.6 shows stationary particle charge distributions calculated for 10-nm-diameter silicon particles ($q_{lim} = 14$), with either Ar^+ or H^+ as the positive ion. Conditions: $n_e/n_i = 1$, T_e =3 eV, and T_i =300 K. The higher mobility of H^+ compared to Ar^+ causes the charge distribution to be shifted toward positive values in the hydrogen case. As seen in Fig. 4.6, both distributions are truncated at the charge limit, but the truncation is more severe in the argon case. The two distributions are still dissimilar, but the existence of the charge limit at -14 now causes the average charge to be much closer in the two cases than if the limit did not exist.

4.7 Effect of Charge Limits on Temporal Evolution of Charge Distribution

To this point we have considered the effect of charge limits only on the stationary distribution of particle charge. We now consider two aspects of the effect of charge limits on the temporal behavior of the particle charge distribution: the time required to reach a steady-state distribution, and the power spectrum of charge fluctuations.

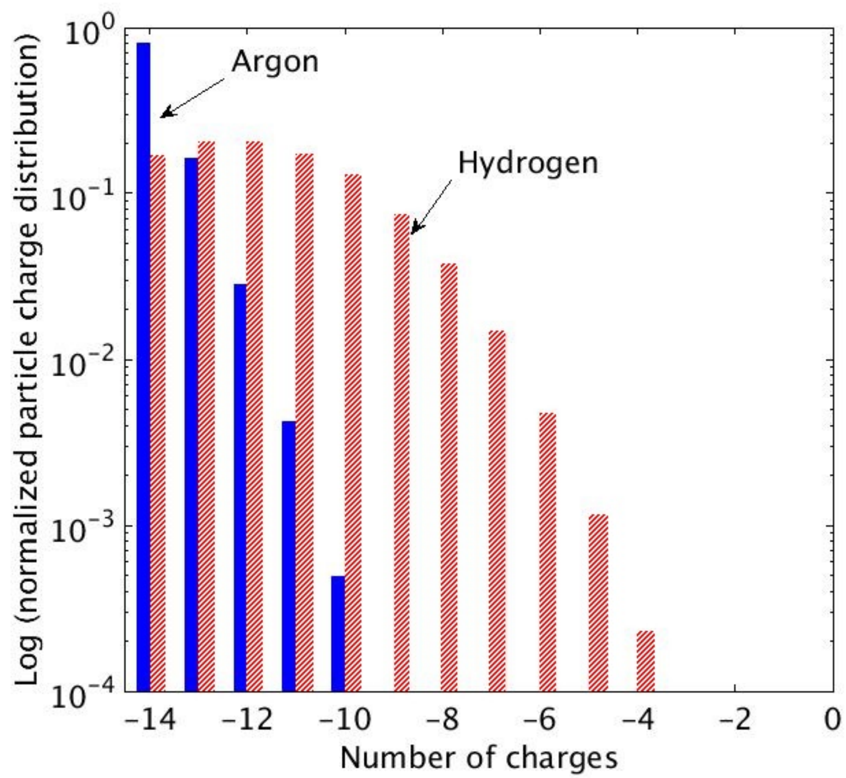

Figure 4.6: Particle charge distributions for 10 nm-diameter silicon particles ($q_{lim} = 14$), with either Ar^+ or H^+ as the positive ion. Conditions: $n_e/n_i = 1$, T_e =3 eV, and T_i =300 K.

4.7.1 Effect of Charge Limits on Time Required to Reach Steady-State Charge Distribution

The existence of charge limits reduces the time required to reach a stationary charge distribution. To explore this effect we used MC simulations assuming various charge limits, with the initial condition that all particles are neutral. Fig. 4.7 shows the temporal variation of average charge for charge limits of 5, 15, and ∞ (no charge limit), assuming the same conditions as in Fig. 4.2. The time required for the average charge to reach steady state is one measure of the time required for the charge distribution to reach steady state. From Fig. 4.7, we see that this time equals $\sim$100 ms for the case without charge limits, but only $\sim$1 ms if the charge limit equals 15 and 0.1 ms if the charge limit equals 5. This behavior is straightforward to understand, as the more severe the charge limit the higher the fraction of particles that bunch into the charge state given by the limit, and the more closely, and rapidly, the average charge is given by the value of the limit itself. Indeed, aside from the much more rapid approach to steady-state, charge limits are seen to strongly reduce fluctuations in average charge, which persist up to long times for the case without charge limits.

4.7.2 Effect of Charge Limits on Power Spectrum of Charge Fluctuations

To characterize the nature of charge fluctuations in the presence of charge limits, we calculated the power spectrum of the fluctuations, defined by

$$P(\omega) = |F[q(t)]|^2, \tag{4.22}$$

where ω is the fluctuation frequency, and F is the Fourier transform of $q(t)$, given by

$$F(\omega) = \int_{-\infty}^{+\infty} q(t)\exp(-i2\pi\omega t)dt. \tag{4.23}$$

Fig. 4.8 shows the charge fluctuation power spectrum for 5-nm-diameter particles both without charge limits (top) and with a charge limit of -5 (bottom). In both cases we calculate the power spectrum after the charge distribution has reached steady state, so that the change in the frequency spectrum is due to the difference in charge distributions not the difference in charging times between the two cases. The existence

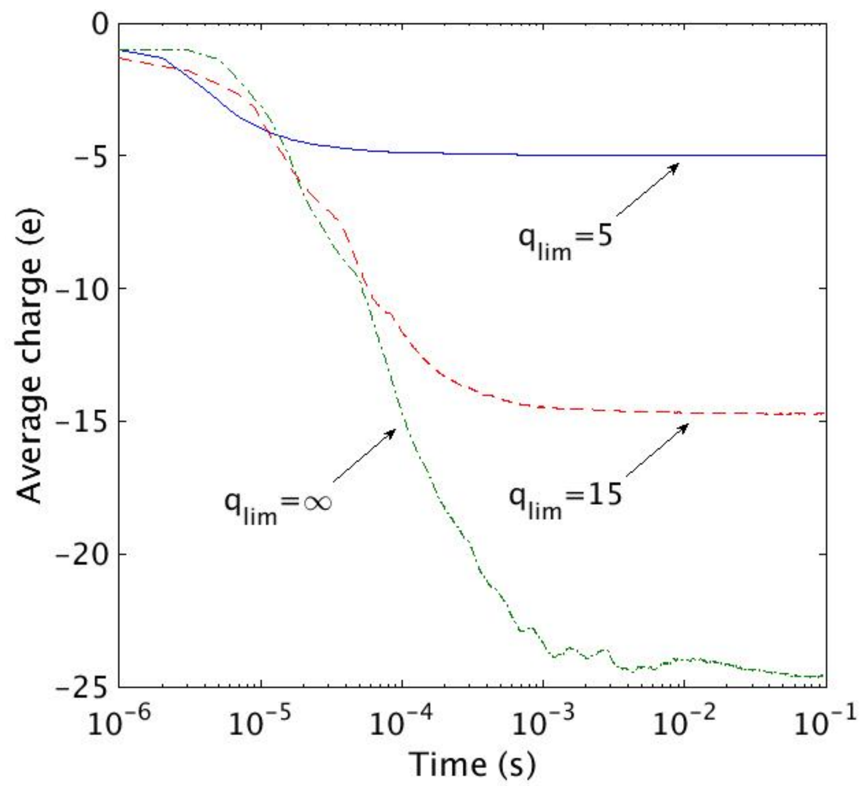

Figure 4.7: Temporal evolution of average charge for 10 nm-diameter particles in an argon with $n_e/n_i = 1$, T_e =3 eV, and T_i =300 K.

of a charge limit is seen to greatly increase the relative importance of high-frequency versus low-frequency fluctuations. This contrasts with the study of Cui and Goree [71], who neglected charge limits and found that the charge fluctuation power spectrum is dominated by low frequencies, and that higher frequency fluctuations decay as ω^{-2}. It should be noted that this effect is particularly pronounced for very small values of the charge limit, and becomes less pronounced at larger values of charge limits.

4.8 Conclusion

Previous studies that have derived expressions for the stationary particle charge distribution in dusty plasmas have neglected the fact that the amount of charge a dust particle can hold is limited. In this chapter we derived an analytical expression for the stationary charge distribution that accounts for the existence of charge limits. This derivation was obtained by suitably modifying the Matsoukas and Russell expression for the charge distribution without charge limits [46]. Values of average charge and variance of the distribution with charge limits were also obtained. The validity of the analytical expression was tested using MC simulations of particle charging. Agreement between the analytical expression and numerical simulations was found to be excellent over a wide range of charge limits, except for the value of the standard deviation of the distribution in cases where the charge limit is very small. In this regime, the assumptions of the Matsoukas and Russell expression that lead to Gaussian charge distributions are known to be violated. Even here, however, the analytical expression produces a quite reasonable approximation to the 'true' distribution predicted by the MC simulations.

For cases where electron depletion by attachment to dust particles causes n_e/n_i to become small, it was shown that the existence of charge limits becomes less important, because the paucity of electrons relative to ions can cause particles to become much less negatively charged than their charge limit allows. It was also shown that ion mass plays an important role in the relative importance of the existence of charge limits, as lighter ions cause the charge distribution to shift toward less negative values.

The effect of charge limits on the temporal behavior of the charge distribution was examined. It was shown that the existence of charge limits can have a strong effect on the time required to achieve a steady-state charge distribution, with smaller charge

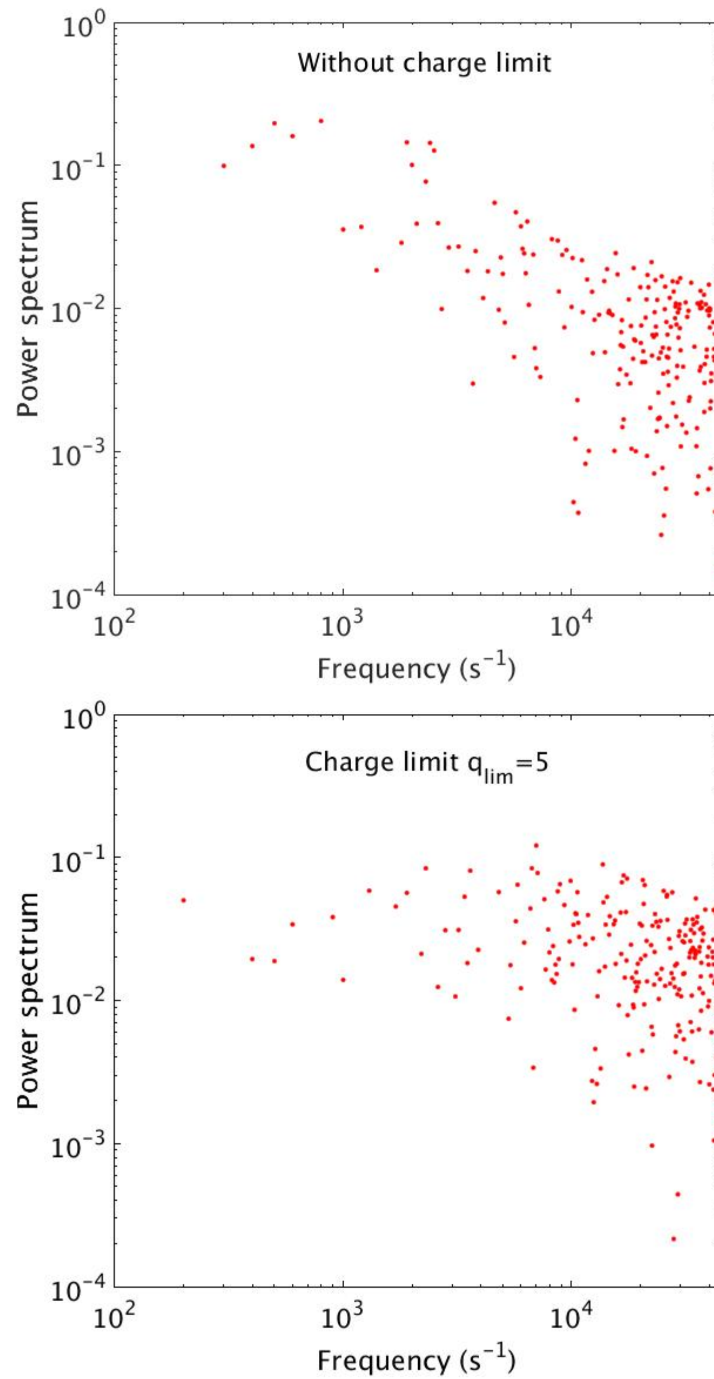

Figure 4.8: Power spectrum of charge fluctuations for 5 nm-diameter particles in an argon plasma with $n_e/n_i = 1$, T_e =3 eV, and T_i =300 K. (top) Without charge limits, (bottom) with a charge limit of -5.

limits promoting a more rapid approach to steady state. Additionally, examination of the power spectrum of charge fluctuations indicates that the existence of charge limits increases the relative importance of high-frequency versus low-frequency charge fluctuations, especially when the charge limit is very small.

It should be noted that the theory and numerical simulations presented here consider only electron and ion attachment, following OML theory, with a sharp cutoff at the particle charge limit. Thus, while electron field emission is discussed as one mechanism that limits particle charge, it is not otherwise taken into consideration as affecting the charge distribution. In principle electron field emission could be included in the MC simulations. However this would require knowledge of the particle-charge-dependent field emission current, which would likely be material-dependent as well. Regrettably this effect remains poorly understood, and quantitative models are lacking. Nevertheless, one can anticipate that the emission current would be greatest at the charge limit itself, and would decrease for smaller negative charge values. Similarly, as a particle's electron affinity decreases as the particle charge approaches the charge limit, it is possible that the electron sticking coefficient would become smaller than unity even though attaching an electron does not exceed the charge limit. Either of these effects, if important, could qualitatively alter the results presented here, as the charge distribution would not bunch as strongly into the charge state corresponding to the charge limit. This therefore suggests possible future work on charge distributions with particle charge limits.

Chapter 5

Stochastic Charging: Non-Negatively Charged Dust in Cold Plasmas

The work presented in this chapter was done in collaboration with Dr. Meenakshi Mamunuru and Dr. Yukinori Sakiyama at Lam Research Corporation.

In the semiconductor industry, the presence of dust particles on wafer surfaces is observed during plasma-enhanced chemical vapor deposition (PECVD) and plasma etching processes. Such particles can lead to defects in the substrate. In a typical parallel-plate capacitively-coupled RF plasma reactor, dust particles are mostly negatively charged and confined at the center of the discharge by the electric field. However, a fraction of these dust particles can be neutral or even positively charged due to stochastic charging. In this chapter, we present the charging mechanisms that cause a large fraction of particles to be non-negatively charged in the pressure range $0.1-100$ Torr. The mechanisms include electron and ion attachment, the effect of pressure on ion current to the particle, electron depletion, secondary electron emission, photoemission, and the single-particle charge limit. We found that under typical plasma processing conditions, electron depletion and the effect of pressure on the ion current significantly reduce the particle charge, hence increasing the fraction of non-negatively charged particles.

5.1 Introduction

Plasmas have unique features that are widely used in the semiconductor industry for surface modification, thin film deposition, and etching, at very small length scale (<20 nm) [104]. Material properties, e.g., hardness and electrical and thermal conductivity, can be modified by varying the plasma conditions and gas mixture. The deposition of silicon nitride (Si_3N_4) thin films can be used for passivation, and Si_3N_4 has the advantage of being a hard material. Silicon nitride can be prepared from silane (SiH_4) and ammonia (NH_3) which usually results in the presence of hydrogen in the film, which is undesirable as it modifies the physical, chemical, and mechanical properties of the film. Silicon dioxide (SiO_2) can be used as an interlayer dielectric film between metallization layers and can be prepared in a gas mixture of silane and nitrous oxide (NO_2). Silane is a well known precursor for the formation of dust particles and therefore it is common to observe dust particle deposition on the substrate under silicon oxide and silicon nitride film deposition [18]. Such dust particles are defects for the process and techniques have been developed to avoid and remove them from reactors [105].

During plasma deposition and plasma etching processes, particle charging plays a significant role in particle transport to the substrate as charged particles respond to the electric field. Various phenomena can affect particle charging, but their independent contribution depends on plasma conditions and particle material properties.

The electron density can be strongly depleted due to the loss of electrons to dust particles in the discharge [4, 11] and when using electronegative gases [106], e.g., sulfur hexafluoride (SF_6) and oxygen (O_2). Under the plasma conditions studied in this work, negative particle charging is dominated by electrons over negative ions, due to the higher electron mobility. The depletion of electrons in such plasmas may play a significant role in particle charging by reducing the overall particle charge and allowing a fraction of particles to be either neutral or positively charged.

Electron and ion attachment plays a dominant role in particle charging. At low pressure, since the ion mean free path is greater than the Debye length, the ballistic motion of ions around the particle can be used to express the ion current to the particle as described by OML theory [8]. As the pressure increases, the ion mean free path decreases ($\propto 1/p$) and the effect of ion-neutral charge-exchange collisions in the vicinity

of the dust has to be added into the expression for the ion current. The new ion produced may not have enough kinetic energy to escape the particle potential and get collected by the particle [68]. The ion capture radius was first proposed by Khrapak *et al.* [107] and was used later by Gatti and Kortshagen to derive an analytical expression for the ion current to a dust particle over a wide range of pressure [9].

Electron emission processes can affect particle charging by producing particles that are less negatively charged. Secondary electron emission (SEE) can occur when a highly energetic electron collides with the particle and emits one or more electrons from the particle surface, hence reducing particle charge [97]. The SEE yield is dependent on the energy of the incoming electron and it is therefore important to consider the effects of the EEDF. Similarly, energetic photons can also emit electrons from the particle surface by the process of photoemission [108].

A particle can only hold a limited number of electrons that depends on its size and material properties (referred as charge limit) [70]. Charge limits can strongly affect particle charge distributions by producing less negatively charged particles. This mechanism is discussed in Chapter 4. Other effects such as thermoemission can also influence particle charging [109]. This mechanism is not included in this study as it is relevant for only particle temperatures much greater than room temperature.

In this chapter, we investigate particle charge distributions in plasmas by developing a Monte Carlo charging model that includes electron and ion attachment, the effect of pressure on the ion current, electron emission processes, and charge limit. Under typical plasma processing conditions, we show that a non-negligible fraction of neutral and positive particles can exist even at large particle sizes (>50 nm). This could explain particle deposition on wafer surfaces.

5.2 Particle Charging Mechanisms

In this section, we review the most pertinent mechanisms that can affect particle charge distributions under the conditions used in typical plasma processing reactors and give a detailed description of the Monte Carlo charging model.

5.2.1 Pressure Effect on Positive Ion Current to a Particle

The background gas pressure can have a significant effect on the ion current to the particle. At low pressure, an ion does not collide with neutral species in the vicinity of the particle, therefore the ballistic motion of the ion is used to estimate the ion current to the particle. An ion that has enough kinetic energy to overcome the Coulomb interaction with a negatively charged particle will not be collected. As the pressure increases, an ion that results from a charge-exchange collision may not have enough kinetic energy and get trapped by the particle potential. This induces an increase in the ion current to the particle and reduces the particle negative charge. As the pressure increases further, ion-neutral collisions become dominant, reducing the ion current to the particle and therefore increasing the particle negative charge. These three regimes are the free molecular regime (OML), the collisional-enhanced regime (CE), and the hydrodynamic regime (HY). Gatti and Kortshagen expressed the ion current to the particle over a wide range of pressure as a weighted function of the three regimes [9],

$$I_i = P_0 I_i^{OML} + P_1 I_i^{CE} + P_{>1} I_i^{HY}, \tag{5.1}$$

where I_i^{OML}, I_i^{CE}, and I_i^{HY} are the ion currents to the particle. P_0, P_1, and $P_{>1}$ are the collision probabilities given by

$$P_0 = \exp\Big(-\frac{1}{\mathrm{Kn}_{R_0}}\Big), \tag{5.2a}$$

$$P_1 = \frac{1}{\mathrm{Kn}_{R_0}} \exp\Big(-\frac{1}{\mathrm{Kn}_{R_0}}\Big), \tag{5.2b}$$

$$P_{>1} = 1 - (P_0 + P_1), \tag{5.2c}$$

where Kn_{R_0} is the capture radius Knudsen number, that is defined so that the minimum particle potential occurs at $\mathrm{Kn}_{R_0} \approx 1$. Ion currents to the particle are given by

$$I_i^{OML} = \pi R^2 v_{i,th} n_i \Big(1 - \frac{e\phi_p}{kT_i}\Big), \tag{5.3a}$$

$$I_i^{CE} = \pi(\alpha R_0)^2 n_i v_{i,th}, \tag{5.3b}$$

Table 5.1: Secondary electron emission coefficients for different bulk materials [1].

Material	δ_M	E_M (eV)
Fe	1.3	350
C (graphite)	1.0	250
SiO_2	2.1−4.0	400
Mica	2.4	350
Al_2O_3	2.0−9.0	350−1300
CaO	2.2	500
MgO	3.0−25	400−1500

$$I_i^{HY} = 4\pi R n_i \mu_i |\phi_p|, \tag{5.3c}$$

where R_0 is the capture radius, R is the particle radius, α is a constant equal to 1.22 when assuming a Maxwellian for the ion energy, and μ_i is the pressure-dependent mobility of the ion. The mobility of the positive ion Ar^+ in Ar plasma is estimated to be 0.145 m^2 V^{-1} s^{-1} Torr [110]. The capture radius depends on the ion mean free path that itself depends on the ion-neutral cross section. The mean free path of the positive ion Ar^+ in Ar plasma follows [111]

$$\lambda_i = \frac{1}{330p}, \tag{5.4}$$

where λ_i is in units of cm and the pressure p is in units of Torr.

5.2.2 Secondary Electron Emission

Secondary electron emission occurs when a highly energetic electron hits the particle and transfers enough of its energy to electrons on the particle to emit them from the particle surface. The secondary electron impact yield δ is defined as the ratio of the secondary electron current I_{see} to the electron current to the particle I_e and is given for monoenergetic electrons by [1, 108]

$$\delta(E) = 7.4\delta_M \Big(\frac{E}{E_M}\Big) \exp\Big[-2\Big(\frac{E}{E_M}\Big)^{1/2}\Big]. \tag{5.5}$$

where E is the electron energy and δ_M and E_M are material-dependent constants. Table 5.1 gives the constant values for different materials.

Because electrons in plasmas are not monoenergetic, the effective yield is found by integrating Eq. (5.5) over the electron energy distribution function (EEDF). Assuming a

Maxwellian distribution for the energy of electrons, Meyer-Vernet derived an expression for the yield emission [1],

$$\delta(T_e) = 3.7\delta_M F_N\Big(\frac{E_M}{4kT_e}\Big) \quad \text{for} \;\; \phi_p < 0, \tag{5.6a}$$

$$\delta(T_e) = 3.7\delta_M \text{exp}\Big[-\frac{\phi_p}{(kT_s - kT_e)}\Big] \times F_P\Big(\frac{E_M}{4kT_e}\Big) \quad \text{for} \;\; \phi_p > 0, \tag{5.6b}$$

where

$$F_N(x) = x^2 \int_0^\infty t^5 \text{exp}[-(xt^2 + t)]dt, \tag{5.7a}$$

$$F_P(x) = x^2 \int_B^\infty t^5 \text{exp}[-(xt^2 + t)]dt, \tag{5.7b}$$

$$B = \Big(\frac{4e\phi_p}{E_M}\Big)^{1/2}. \tag{5.7c}$$

T_s is the temperature of the emitted electron and is typically $1 < T_s < 5$ eV [112]. The exponential term in Eq. (5.6b) is there to account for the fact that electrons that do not have enough kinetic energy to overcome the attractive particle potential would not be emitted.

5.2.3 Photoemission

Photoemission occurs when an incoming photon has enough energy to remove an electron from the particle surface. This mechanism is strongly dependent on the dust material properties and the particle potential. The photoemission current from the particle is given by [108]

$$I_\nu = 4\pi R^2 \mu \Gamma_\nu \quad \text{for} \;\; \phi_p < 0, \tag{5.8a}$$

$$I_\nu = 4\pi R^2 \mu \Gamma_\nu \text{exp}\Big(-\frac{e\phi_p}{kT_p}\Big) \quad \text{for} \;\; \phi_p > 0, \tag{5.8b}$$

where μ is the photoemission efficiency, Γ_ν is the photon flux, and T_p is the photon temperature (assuming that the photoelectrons have a Maxwellian energy distribution). The photoemission efficiency is estimated to be $\mu \approx 1$ for metals and $\mu \approx 0.1$

for dielectrics−note that these values are rough estimations and should also be dependent on the particle size. The exponential term in Eq. (6.17b) is due to the Coulomb attraction between an emitted electron and the positive particle surface potential.

Photoemission has been extensively studied in space plasmas where UV radiation is important. In plasma processing reactors, photoemission effects are most probably less significant, and the uncertainty is on estimating the proper photon flux.

5.2.4 Single-Particle Charge Limits

The maximum number of electrons that can coexist on a single particle is called *charge limit*. The effect of particle charge limits on charge distributions is discussed in Chapter 4 and Ref. [70]. It has been shown that such effects may contribute to particle growth [7, 72]. The charge limit is material-dependent and its magnitude is therefore different for Si, SiO_2, and Si_3N_4 particles. It was found that charge limit effects are significant at electron-to-ion density ratio n_e/n_i close to unity. In electronegative plasmas, where $n_e/n_i < 0.1$ and therefore the reduce availability of electrons for charging, charge limits may not be the dominant effect on reducing the overall particle charge, and producing a high fraction of positive and neutral particles.

5.3 Description of the Monte Carlo Charging Model

The Monte Carlo charging model used in this work is based on Ref. [68], a model originally developed to calculate charge distributions accounting for electron and ion attachment only in low-pressure plasmas. We extended the code by adding other mechanisms: particle charge limits, electron emission processes, and the effect of pressure on ion current to a particle. Electron-ion recombination reactions and hydrogen surface reactions were also included to follow particle temperature fluctuations, as described in Chapter 3.

A flow chart of the Monte Carlo charging code is shown in Fig. 5.1. The model calculates the transient evolution of particle charge, starting from a neutral state at $t = 0$ s. The next time a charging event occurs is randomly determined based on the time scale for the different charging mechanisms. The typical collision/emission time scale is $\sim \mu$s and the overall time of a simulation is set to ∼10 s, which represents

$>10^6$ collision/emission events and gives relevant statistical data. The time step of the simulation is chosen to be much smaller than the greatest frequency ($\Delta t = 10^{-9}$s).

5.4 The Existence of Neutral and Positive Particles

Under plasma processing conditions, dust particles can nucleate and grow in the reactor. A detailed description of the particle deposition mechanisms on wafer surfaces would require multidimensional models that would account for particle growth, charging, transport, and coupling between the particle cloud and the plasma. The hypothesis in this chapter is that under some conditions particle deposition may be due to the existence of neutral and positive particles that would be able to escape the plasma electric field and transport to the substrate. In this section, we show that under typical plasma processing conditions (e.g., PECVD), along with the stochastic nature of particle charging, a large fraction of neutral and positive particles can exist. All the results presented in this section are based on Monte Carlo simulations.

5.4.1 Reduction in Particle Charge

In plasma processing systems, the electron mobility is typically much higher than that of negative ions, so that electrons are the dominant negative species for particle charging. Negative ions are ignored in the rest of this section and the ion density n_i refers to that of positive ion only. Under some conditions, negative ions do play an important role in particle charging, such as in the plasma afterglow where electrons are quickly lost by diffusion and recombination.

The electron density can be significantly reduced compared to the positive ion density, either due to electron attachment to the particle, or because of the plasma electronegativity. Either way, because of the lower electron density, the particle charge reduces as the electron-to-ion density ratio decreases. At low pressure, and using OML currents to the particle, the average charge varies as $\bar{q} \propto \ln(n_i/n_e)$. Fig. 5.2 shows particle charge distributions for (left) n_e/n_i=0.1, (middle) n_e/n_i=0.01, (right) n_e/n_i=0.001 for a 10 nm diameter particle under typical low-pressure plasma conditions. As the negative particle charge reduces, the fraction of particles is neutral and positive charge

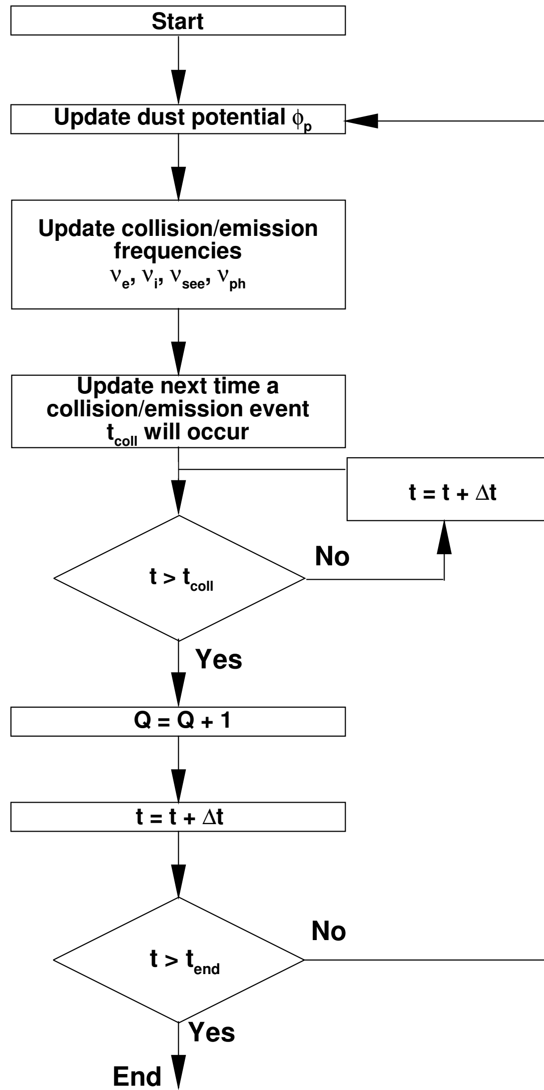

Figure 5.1: Flow chart of the Monte Carlo charging code: t is the instantaneous time, ϕ_p is the particle potential, ν_e is the electron collision frequency, ν_i is the ion collision frequency, ν_{see} is the frequency of secondary electron emission, ν_{ph} is the frequency of photoemission, t_{coll} is the next time a collision/emission event occurs, Q is the instantaneous particle charge, Δt is the time step of the simulation, and t_{end} is the total simulation time.

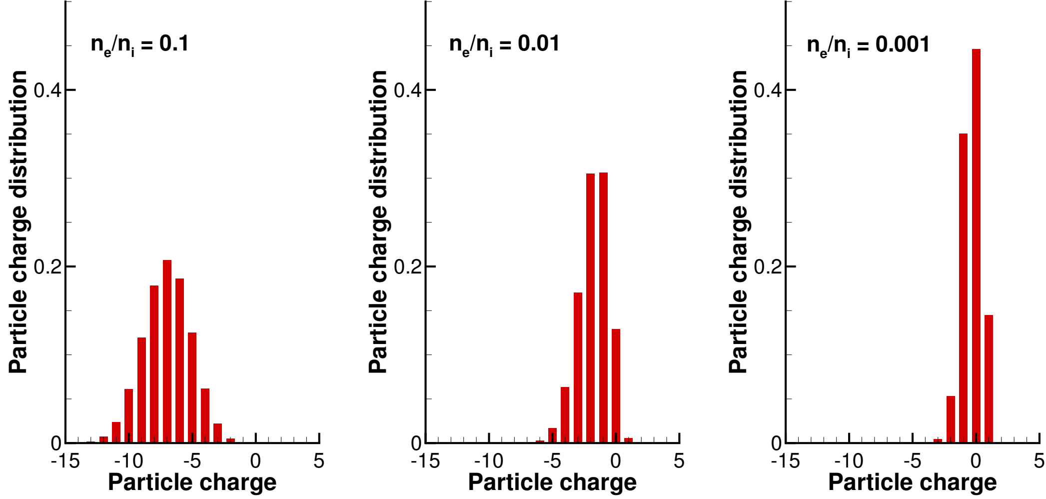

Figure 5.2: Particle charge distribution obtained by MC simulations for different electron-to-ion density ratio (left) $n_e/n_i = 0.1$, (middle) $n_e/n_i = 0.01$, and (right) $n_e/n_i = 0.001$, for a 10-nm-diameter particle at T_e =2 eV, T_i =300 K, O_2^+ ion, n_i=10^9 cm^{-3}, and the ion current is given by OML theory [8]. Charge limits and emission processes are not included. The electron energy distribution is assumed to be Maxwellian.

states increases. It has been shown that large particle size or high particle density can deplete the electron density by over two orders of magnitude [11]. At low pressure, and using the OML theory, the ion density magnitude does not affect the steady-state charge distribution (the ratio n_e/n_i does), but only the time required to reach this steady-state. An increase in electron temperature would increase the electron flux to the particle, hence resulting in more negatively charged particles, and therefore producing less non-negatively charged particles. The ion temperature is assumed to be at the background gas temperature ($\approx$ 300 K). An increase in ion temperature would produce particles that are more negatively charged as more energetic positive ions can overcome the Coulomb attraction between a positive ion and a negatively charged particle, therefore not attaching to the particle.

While the OML theory [8] is satisfactory for expressing the ion current to the particle for small particle size and in low-pressure plasmas, it cannot be used as the gas pressure increases. Because of inelastic ion-neutral collisions in the vicinity of the particle, the ion current to the particle may increase or decrease. Fig. 5.3 shows the average particle

charge for a (left) 10-nm and (right) 100-nm-diameter particle for the pressure range 0.1−100 Torr at $n_e/n_i = 1$. The capture radius Knudsen number is given by [9]

$$\mathrm{Kn}_{R_0} = \frac{\lambda_i}{2\alpha R_0}. \tag{5.9}$$

It is defined so that $\mathrm{Kn}_{R0} \approx 1$ corresponds to the maximum ion current to the particle (or the minimum in particle charge). For a 10-nm-diameter particle, the average particle charge decreases monotonically with pressure, from $\bar{q} = -16$ at 0.1 Torr to $\bar{q} = -4$ at 100 Torr. At such sizes, the ion current is in the collision-enhanced regime, i.e., ion-neutral collisions increase the ion current to the particle. For a 100-nm-diameter particle, the average particle size decreases with pressure from $\bar{q} = -105$ at 0.1 Torr to $\bar{q} = -40$ at 10 Torr, and then increases with pressure to $\bar{q} = -85$ at 100 Torr. The difference in behavior for 10 and 100-nm-diameter particles is explained by the smaller Knudsen number at larger particle size. It is worth noting that the minimum particle charge for a 100 nm diameter particle is at 10 Torr, which corresponds to typical PECVD conditions (1−10 Torr). Pressure effects in this regime seem to be significant on particle charging.

Electrons play a dominant role in particle charging in the plasma conditions considered in this work. Fig. 5.4 shows the average particle charge for particles of (left) 10 nm and (right) 100 nm in diameter in the pressure range 0.1−100 Torr and n_e/n_i =0.01, 0.1. and 1.0 (same plasma conditions as Fig. 5.3). As expected, the average particle charge decreases as n_e/n_i decreases. At low pressure and using OML theory for the currents to particles, since $\bar{q} \propto \ln\,(n_i/n_e)$, the average particle charge decreases by a factor of ≈ 4 from n_e/n_i =1 to 0.01. For a 100 nm diameter particle at 0.1 Torr, $\bar{q} = -110$ at $n_e/n_i = 1$ and $\bar{q} = -25$ at $n_e/n_i = 0.01$. At 10 Torr and $n_e/n_i = 0.01$, the average charge is −8.4, which is much less than in electropositive plasma where the electron-to-ion density ratio is closer to unity. Considering charge fluctuations, we can expect a fraction of particles to be non-negatively charged.

In typical PECVD reactors, negatively charged particles are trapped at the center of the discharge by the electric field. Therefore, it is important to estimate the fraction of particles that are neutral or positively charged, as they are able to escape the plasma and transport to the substrate. Fig. 5.5(left) shows the fraction of particles

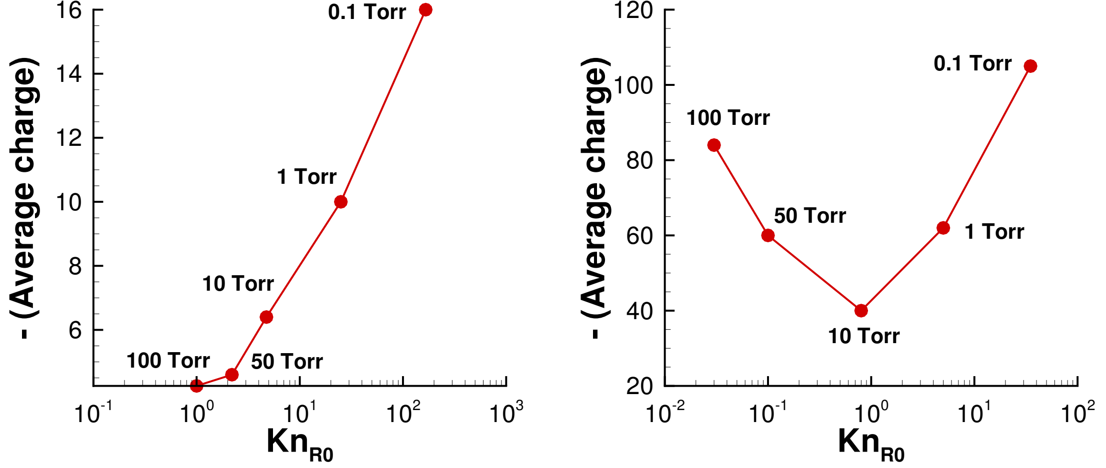

Figure 5.3: Average particle charge obtained by MC simulations for pressures 0.1−100 Torr for a (left) 10-nm and (right) 100-nm-diameter particle, T_e =2 eV, T_i =300 K, Ar^+ ion, and $n_e = n_i$=10^9 cm^{-3}. The capture radius Knudsen number is given in Ref. [9] and the ion current is given by Eq. (5.1). Charge limits and emission processes are not included. The electron energy distribution is assumed to be Maxwellian.

that are non-negative (i.e., neutral + positive) for 10 nm-diameter particles in the pressure range 1−100 Torr and n_e/n_i =0.01−1. The model includes particle charge limits for SiO_2 particles (q_{lim} = 3 for 10 nm diameter particle [70]). A pressure increases, the particle charge distribution for a 10 nm diameter particle monotonically shifts to less negatively-charged particles as shown in Fig. 5.3(left). Therefore the fraction of non-negatively charged particle increases with pressure. Similarly, the fraction of non-negatively charged particles significantly increases as n_e/n_i decreases. At 10 Torr, the fraction of non-negatively charged particles is increased by more than 4 orders of magnitude, from 3×10^{-6} at n_e/n_i = 1 to 7×10^{-2} at n_e/n_i = 0.01. It is shown in Chapter 4 that charge limit effects are negligible at low n_e/n_i since the average particle charge due to electron and ion attachment is smaller than the charge limit value. Fig. 5.5(left) shows that charge limits slightly increase the fraction of neutral and positive particles, by less than an order of magnitude. This value is material dependent and we would expect the effects of charge limits to be even less important for Si particles, due to its larger electron affinity.

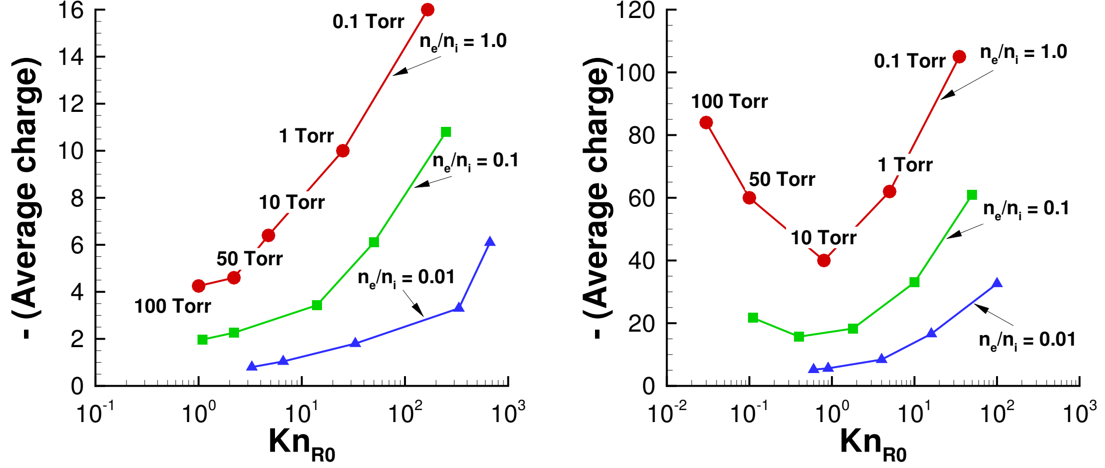

Figure 5.4: Average particle charge obtained by MC simulations for pressures 0.1−100 Torr and electron-to-ion density ratio $n_e/n_i = 0.01 - 1$ for a (left) 10-nm and (right) 100-nm-diameter particle, T_e =2 eV, T_i =300 K, Ar^+ ion, and n_i=10^9 cm^{-3}. The capture radius Knudsen number is given in Ref. [9] and the ion current is given by Eq. (5.1). Charge limits and emission processes are not included. The electron energy distribution is assumed to be Maxwellian.

A positive particle can be transported outside the plasma and be accelerated in the sheath formed between the bulk plasma and the substrate, and may possibly damage it if its kinetic energy is large enough. At low pressure, the particle gain in kinetic energy equals the potential drop in the sheath, typically ∼20 V. As the pressure increases, the gain in kinetic energy is less than the potential drop due to losses during collision events with the background gas. This is discussed in more detailed in Chapter 6. Fig. 5.5(right) shows the fraction of neutral and positively charged particles for a 10 nm diameter particle and pressure 5 Torr for n_e/n_i ranging from 0.01 to 0.1. At $n_e/n_i = 0.1$, the fraction of non-negatively charged particles is $\sim 10^{-4}$ at 10 Torr and increases above 10^{-2} at 100 Torr. Under such conditions, the neutral fraction is always orders of magnitude greater than for the positive fraction. At $n_e/n_i = 0.1$, the fraction of neutral particles is greater than that of positive particles by a factor of ∼133.

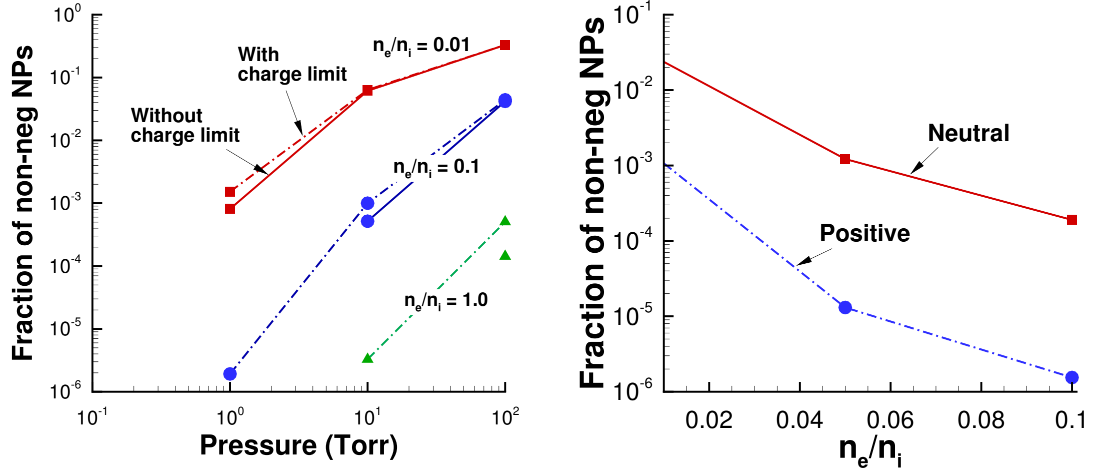

Figure 5.5: Fraction of non-negatively charged particles obtained by MC simulations for a 10-nm-diameter particle (left) as function of pressure and (right) as function of electron-to-ion density ratio at T_e =2 eV, T_i =300 K, Ar^+ ion, n_i=10^9 cm^{-3}. Particle charge limit is included−for 10 nm SiO_2 particle, q_{lim}=3. Emission processes are not included. The electron energy distribution is assumed to be Maxwellian.

5.4.2 Electron Emission Processes

In the previous section, the effects of pressure, electron depletion, and charge limits have been discussed. It was shown that the particle charge distribution can be significantly shifted to less negatively-charged particles and increasing the fraction of neutral and positive particles. In this section, we investigate electron emission processes as they can reduce the negative particle charge even further.

Secondary Electron Emission

Secondary electron emission (SEE) occurs when an electron hitting a particle transfers enough energy to one or more electrons on the particle, given them enough kinetic energy to escape the particle−resulting in an electron current out of the particle. Secondary electron emission yield is material-dependent as shown in table 5.1. Fig. 5.6(left) shows particle charge distributions for SiO_2 particles with and without secondary electron emission for δ_M = 2.1 and δ_M = 4.0. The particle size is 100 nm, the pressure is

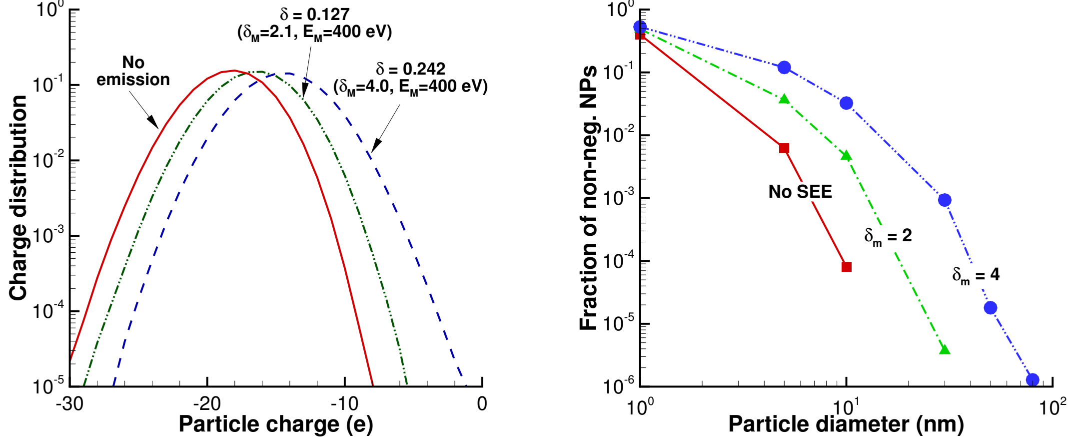

Figure 5.6: Results are obtained by MC simulations. (Left) Particle charge distribution for SiO_2 particles using different values for secondary electron emission coefficients, δ_M=2.1−4 and E_M=400 eV [1], (right) fraction of non-negatively charged particles for SiO_2 of 1−100 nm in diameter, T_e =2 eV, T_i =300 K, p = 10 Torr, Ar^+ ion, n_i=10^9 cm^{-3} and $n_e/n_i = 0.1$. Charge limits and photoemission are not included. The electron energy distribution is assumed to be Maxwellian.

10 Torr, and $n_e/n_i = 0.1$. As the parameter δ_M increases, the charge distribution shifts to less negative values, since the secondary electron emission increases. The charge distributions show that under these conditions the fraction of neutral or positive particles is less than 10^{-5} due to secondary electron emission. However, by changing some parameters (e.g., plasma conditions and material properties), secondary electron emission would produce non-negatively charged particles.

Under the same conditions, Fig. 5.6(right) shows the fraction of non-negatively charged particles for δ_M=2.1−4 for particles ranging from 1 to 100 nm in diameter. Without accounting for secondary electron emission, the fraction of non-negatively charged particles greater than 10 nm in diameter is less than 10^{-4}. This observation is different when including secondary electron emission. For $\delta_M = 2.0$, the fraction of non-negative particles is above 3×10^{-5} up to 30 nm diameter, and 2×10^{-6} 80 nm for $\delta_M = 4.0$. The magnitude of this fraction increases with secondary electron emission for particles of a given size. For a 10 nm-diameter particle, the fraction of non-negatively

charged particles is 10^{-4} when secondary electron emission is not included and 5×10^{-2} when it is included and $\delta_M = 4.0$. For a 1 nm-diameter particle, the fraction is 0.4 when secondary electron emission is not included and 0.5 when it is included and $\delta_M = 4.0$. Under these conditions, the effect of secondary electron emission at small particle size is small because a high fraction of non-negatively charged particles already exist even without including it. Electrons on the surface of the particle need a kinetic energy greater than the particle potential to be able to escape the particles, and therefore secondary electron emission is less significant for positive particles.

Effect of electron energy distribution function

Experimental and theoretical studies have shown that the presence of large dust particles in plasmas could strongly affect the electron energy distribution function (EEDF) [4, 54, 82]. Electron currents to particles and secondary electron emission are strongly dependent on the EEDF. Fig. 5.7(left) shows two EEDFs with the same average electron temperature of 4 eV. The non-Maxwellian distribution was calculated in dusty plasmas using Bolsig+ [10] and provided to us by Dr. Meenakshi Mamunuru at Lam Research Corporation. The EEDF was calculated for 500-nm-diameter particle at a density of 10^6 cm^{-3} in Ar at a density of 10^{10} cm^{-3}, the gas temperature is 300 K, and the reduced electric field is 140 Td. Particle background gas and particle size may differ from the range of conditions this work focuses one, but the depletion of the high electron energy is observed in plasma processing systems, and therefore the EEDF in Fig. 5.7(left) can be used for this study. The non-Maxwellian distribution has fewer highly energetic electrons because of inelastic collisions with the gas species (e.g., ionization and excitation) and electron attachment to the particles. Fig. 5.7(right) shows the steady-state charge distributions without SEE for both EEDFs. The results show that the distributions are not significantly changed by the form of the EEDF. This is because typical particle potentials under these conditions are less that 1 eV, which is much less than the typical electron energy, so only a small fraction of electrons are unable to attach to particles. Note that as a particle gets larger, it can collect more electrons on its surface, $\bar{q} \propto R$, but the particle potential varies as $\phi_p \propto \bar{q}/R$, so that the particle potential remains small even at larger sizes. At first, it can seem surprising that the charge distribution in the Maxwellian case is less negative than the for non-Maxwellian distribution, since

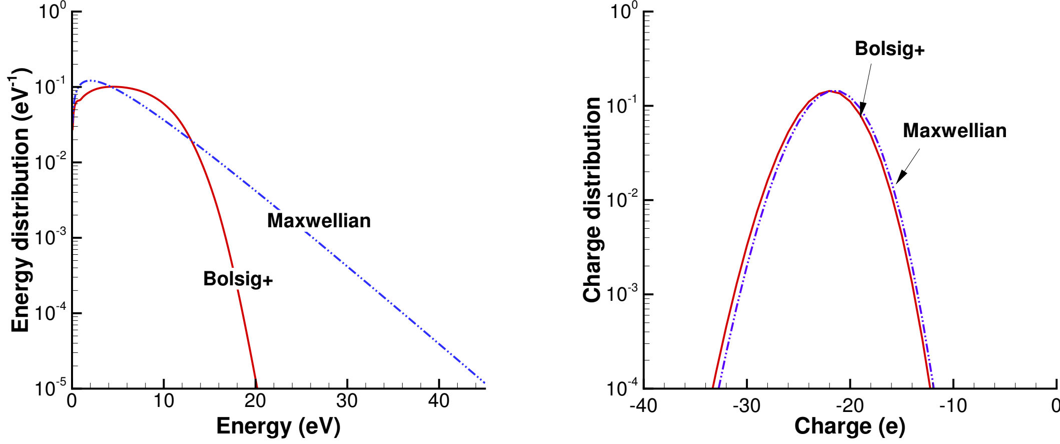

Figure 5.7: (Left) Maxwellian and non-Maxwellian electron energy distribution functions (EEDFs) at the same effective electron temperature, $T_e = 4$ eV. The non-Maxwellian distribution was calculated using Bolsig+ [10]. (Right) Charge distribution obtained by MC simulations using Maxwellian and non-Maxwellian EEDFs to calculate the electron current to particle for a 80 nm diameter particle at $T_i = 300$ K, $p = 5$ Torr, $n_e/n_i = 0.1$, and $n_i = 10^9$ cm^{-3}. Charge limits and photoemission are not included.

the Maxwellian has more highly energetic electrons. The reason is that the Maxwellian distribution has more low energy electrons that are not able to overcome the particle negative potential.

The impact yield for secondary electron emission is strongly dependent on the electron energy as shown in Eq. (5.5) for monoenergetic electrons. To account for the distribution in energy, the yield has to be integrated over the EEDF. For Maxwellian distributions and at given particle potential ϕ_p, this leads to Eqs. (5.6). Fig. 5.8(left) shows the effective secondary electron yield as a function of particle size for Maxwellian and non-Maxwellian EEDFs, and the charge distribution without including SEE. The particle charge varies in the range -35 to -15. The impact yield forthe case of Maxwellian EEDF is almost constant at 0.22 and decreases between 0.21 and 0.15 with particle charge for the non-Maxwellian case. The yield is almost constant for the Maxwellian EEDF as the particle potential is much lower than the highly energetic electrons.

Particle charge distributions for a 80 nm diameter particle at 5 Torr and $n_e/n_i = 0.1$

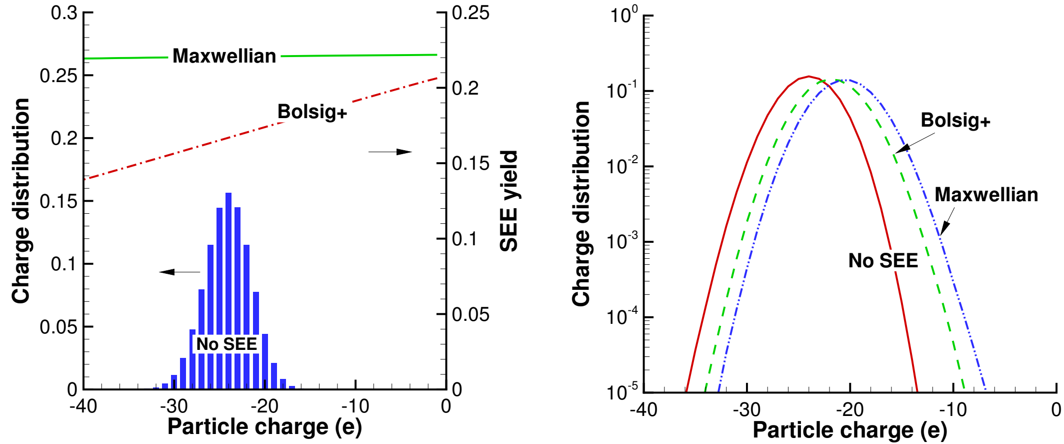

Figure 5.8: (Left) Effective secondary electron emission yield for the Maxwellian and non-Maxwellian distributions from Fig. 5.7(left) and charge distribution for a 80-nm-diameter particle without accounting for secondary electron emission. (Right) Charge distributions that account for secondary electron emission and using Maxwellian and non-Maxwellian EEDFs to calculate the electron current to particle for a 80 nm diameter particle at $T_i = 300$ K, $p = 5$ Torr, $n_e/n_i = 0.1$, and $n_i = 10^9$ cm^{-3}. Charge limits and photoemission are not included.

are shown in Fig. 5.8(right) for Maxwellian and non-Maxwellian EEDFs. As expected, the Maxwellian distribution increases the SEE and therefore produces less negatively charged particles compared to the non-Maxwellian. It is worth noting that an increase in electron temperature would tend to produce more negatively charged particles, but it also increases SEE which would reduce negatively charged particles. Neglecting SEE, the dependence of average particle charge on electron temperature at low pressure is $\bar{q} \propto T_e \ln{(T_e^{1/2})}$.

Photoemission

Fig. 5.9 shows particle charge distribution without photoemission and with photoemission with photon fluxes of 10^{16} cm^{-2} s^{-1} and 10^{17} cm^{-2} s^{-1}. The particle is 100 nm in diameter, the pressure 10 Torr, $n_e/n_i = 0.1$, and the efficiency is $\mu = 0.1$ for semiconductor particles. As the flux increases to 10^{17} cm^{-2} s^{-1}, particles have a higher fraction

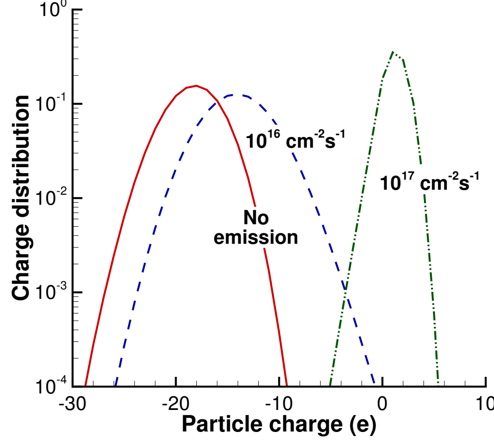

Figure 5.9: Particle charge distribution obtained by MC simulations for different photon fluxes to a 100-nm-diameter particle at T_e =2 eV, T_i =300 K, Ar$^+$ ion, n_i=10^9 cm^{-3}, n_e/n_i = 0.1, and p = 10 Torr. Charge limits and secondary electron emission are not included. The electron energy distribution is assumed to be Maxwellian.

of positively-charged particles compared to neutral and negatively charged particles. Such photon fluxes are observed in space [96].

To estimate the photon flux to particles in typical PECVD conditions, measurements were conducted by Dr. Yukinori Sakiyama at Lam Research Corporation in a parallel-plate system, N_2 plasma at 2 Torr and 200 W input power. An optical fiber was inserted in the plasma and the photon flux was found from the current measurement using a photodiode as

$$\Gamma_\nu = \Big(\frac{1}{\alpha_{PD}\alpha_{fib}} \times \frac{V_{PD}}{R_{gnd}}\Big) \times \frac{1}{\pi R_{fib}^2} \times \frac{\lambda_\nu}{hc}, \tag{5.10}$$

where $\alpha_{PD} = 0.4$ is the photodiode responsivity, $\alpha_{fib} = 1$ is the fiber loss, the ratio V_{PD}/R_{gnd} is the photocurrent with $V_{PD} = 5 - 50$ mV and $R_{gnd} = 1\text{M}\Omega$, $R_{fib} = 300$ μm is the fiber radius, $\lambda_\nu = 300 - 800$ nm is the photon wavelength, $h = 6.63 \times 10^{-34}$ J s is the Planck constant, and $c = 3 \times 10^8$ m s^{-1} is the speed of light. Under these conditions, the photon flux measured varies in the range 10^{13} cm^{-2} s^{-1} and 10^{14} cm^{-2} s^{-1}. By comparing this flux with Fig. 5.9, it shows that photoemission effects under these conditions may not play a significant role in particle charging. Some uncertainties remain on the efficiency which is based on particle material properties and

should account for particle geometry as well, mostly at small particle sizes.

5.5 Conclusion

Dust particle deposition on wafer surfaces under typical plasma processing conditions can be partly explained by particle charging. Due to the stochastic nature of charging, a fraction of particles can be neutral or even positively charged. In typical parallel-plate reactors, non-negatively charged particles are not trapped in the discharge and can be transported to the substrate.

In this chapter, we developed a Monte Carlo charging model that includes the dominant mechanisms that affect particle charging, i.e., electron and ion attachment, effect of pressure on the ion current to the particle, particle charge limits, secondary electron emission, and photoemission. Plasma conditions were based on typical plasma processing conditions in which dust particles (10−100 nm in diameter) were observed during the plasma ON phase. Plasma conditions and material properties were found in the literature or experimental measurements done at Lam Research Corporation.

We showed that electron depletion and the effect of pressure on the ion current to the particle are the dominant mechanisms to reduce particle charge, which can result in a high fraction of non-negatively charged particles. The ion current to the particle is in the collision-enhanced regime in the pressure range 1−10 Torr, which is the minimum particle potential.

Particle charge limits reduce particle charge since they impose a limit on the number of electrons that can coexist on a particle. The effects of charge limits are material dependent and depend on the particle material properties (see Chapter 4). Since the electron affinity of Si (4.05 eV) is greater than for SiO_2 (1.0 eV), the latter has more significant effects on charge distributions. However, as the ratio n_e/n_i decreases to less than 0.1, the particle charge may often be smaller than the charge limit so that charge limit effects become negligible.

To get more insight on the mechanisms leading to particle deposition on walls, future work should consider spatial variations (similar to Chapter 3) as particle transport plays a major role in the process.

Chapter 6

Silicon Nanoparticle Transport to a Substrate in Hydrogen-Silane Pulsed Plasma Discharges

In typical parallel-plate capacitively-coupled RF plasmas, most of the dust particles are negatively charged due to the higher mobility of electrons compared to positive ions. Because the substrate potential is generally less than the plasma potential, negatively charged particles are trapped at the center of the discharge. When the plasma is turned off, these particles will eventually deposit on the substrate. In this work, we studied the transport, the flux, and the impact energy of these negatively charged particles in a H_2/SiH_4 gas mixture at a constant pressure of 2 Torr. Using a one-dimensional fluid model for the plasma and coupling the nanoparticle cloud to the plasma, we studied the behavior of the chemical species and dust particles in the afterglow. Electron energy relaxation occurs on the time scale of $\sim \mu$s while the electron density relaxes over $\sim$ 100s μs. In the afterglow, we applied a positive DC bias to the substrate to attract the negatively charged particles. We found that even though the flux and the impact energy can be tailored by varying the DC bias, the surface electric field at the substrate is affected by the changing density profiles of ions and nanoparticles. This work focuses on preliminary work exploring system behavior during the first cycle of such a pulsed plasma.

6.1 Introduction

Pulsed plasmas have been extensively used as they offer unique advantages compared to continuous wave plasmas. During plasma etching processes, it has been shown that pulsed plasmas can improve etch selectivity [113], improve deposition rate [114], and reduce dust particle formation [115] by modifying negative species density profiles across the discharge.

As soon as the power generator is turned off, the electron temperature and density decay, recombination processes occur, and neutral and charged species diffuse to the wall. All these transient processes happen in time scales that typically range between μs to s. The mechanisms that occur in the plasma afterglow have been studied quite extensively [116, 117]. The presence of charged dust particles in plasmas can have significant effects on the plasma behavior in the afterglow. Berndt *et al.* showed that the electron density could increase right after turning off the plasma [118]. Schweigert and Alexandrov developed a numerical model and attributed this electron density increase to electron emission from the dust particle surface, along with metastable-metastable ionization processes [119].

The control of nanoparticle size in plasma discharges is of great interest due to potential applications that are particle-size dependent [120]. Controlling the particle residence time in plasmas can be achieved in flowing plasmas by varying the background gas flowrate [49] (see Chapter 3). Pulsed plasmas present an alternative way to control the particle size as shown experimentally [121] and numerically [14].

Roca i Cabarrocas *et al.* observed epitaxial growth of crystalline silicon films by PECVD at low-substrate temperature ($\sim$ 175°C) [122]. This observation has been attributed to the formation of small nanocrystals ($\sim$1 nm) that would be accelerated by the potential drop in the sheath formed at the substrate. Energetic nanoparticles would impact the substrate and melt, which could provide enough energy to the atoms to rearrange themselves and enable a crystalline film growth. The possibility of such a scenario was corroborated by Molecular Dynamics simulations for both large Mo and Cu clusters impacting Mo(001) and Cu(111) surfaces respectively [123, 124].

Larriba and Girshick used a numerical model to show the possibility of tuning the flux and the impact energy (eV/atom) of small nanoparticles to a substrate by varying

the plasma parameters (e.g., RF voltage, pressure, pulse frequency, and duty cycle) in an Ar/SiH_4 discharge at ∼100 mTorr [14]. While their results predict sufficiently high impact energy at the substrate, i.e., ∼1 eV/atom, they cannot fully explain the observation in Ref. [122] since the gas composition and plasma parameters are different.

In this chapter, we study the nanoparticle transport mechanisms in the afterglow of a capacitively-coupled RF pulsed plasma in H_2/SiH_4 at 2 Torr (as in Ref. [122]). When the plasma is turned off, a positive DC bias is applied at the substrate to attract the negatively charged particles. We show the possibility of accelerating the nanoparticles to the substrate by adjusting the value of the DC bias, but that the surface electric field by more than an order of magnitude, due to the coupling between the charged species and the field. We also discuss the spatiotemporal evolution of the nanoparticle cloud in the afterglow, based on preliminary work exploring system behavior during the first pulse cycle. Therefore, simulations have not reached a quasi-periodic steady-state.

6.2 Description of the Model

6.2.1 Plasma-Aerosol Code

The Plasma-Aerosol code used in this work was first developed by Warthesen and Girshick [5]. It is a one-dimensional fluid model that solves for Poisson's equation for the electric field, the continuity equation and energy equation for electrons and the continuity equation for heavy species. Dust particle nucleation, growth, charging, and transport are implemented within a sectional model framework. Ravi and Girshick [12] added the effects of the induced dipole between a charged and a neutral particle and found that this could increase the overall coagulation rate by up to two orders of magnitude [12]. Agarwal and Girshick implemented a chemistry module and a pulsed plasma module [13, 48]. Larriba and Girshick studied the effects of external plasma parameters on the flux and the impact energy of dust particles to a substrate in Ar/SiH_4 pulsed plasmas [14]. A detailed description of the code can be found in Refs. [11, 13].

The code is divided into three modules: plasma module, chemistry module, and aerosol module. Each module calculates different variables that are shared with the other modules, as shown in Fig. 6.1. To manage the computational demand, the code uses a time slicing method, meaning that time step is different in each module and

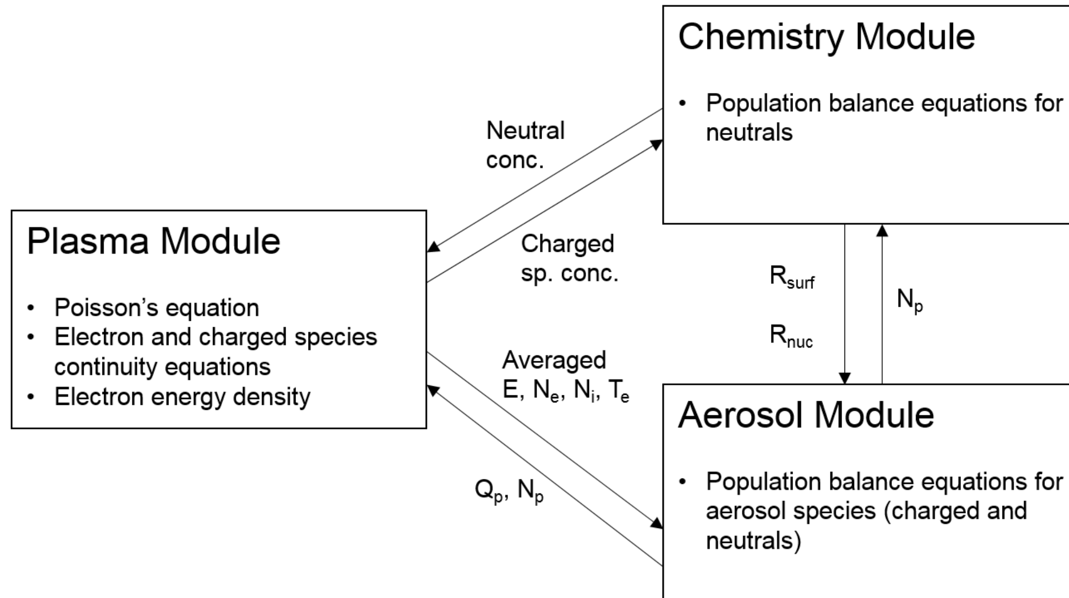

Figure 6.1: Schematic of the Plasma-Aerosol code developed by Girshick and coworkers [5, 11, 12, 13, 14]. Each module calculates and returns some set of variables that are used by the other modules. R_{surf} is the surface growth rate, R_{nuc} is the nucleation rate, Q_p is the dust particle space charge, N_p is the dust particle density, E is the electric field, N_e is the electron density, N_i is the density of the species i, and T_e is the electron temperature. The code uses a time slicing method, meaning that the time step in each module is different, and depends on the plasma conditions.

depends on the plasma parameters and the time scale of the processes computed. In the plasma module, the time step equals a small fraction of the RF cycle−for an RF frequency of 13.56 MHz, the time step used is 9.2×10^{-11} s. The time step in the aerosol module is typically 10^{-7} s, and is 10^{-5} s in the chemistry module.

The criteria to switch from one module to another are as follows. The code starts with the plasma module and looks for the steady-state solution based on the initial conditions. When it is reached, the cycle averaged electric field, the electron and ion density, and the electron temperature are sent to the aerosol module. The aerosol module solves for the continuity equations of each size-charge combination until the change in the aerosol net charge Q_p varies by no more than 1% before sending back the aerosol space charge and the aerosol density variables to the aerosol module. Every

certain number of time steps, the neutral species densities are updated in the chemistry module.

In the afterglow, the time step is the same in all modules since the charging and transport phenomena are in the same time scale order of magnitude. Therefore, each module is called one at a time.

The governing equations for particles in such plasmas are discussed in Chapters 2 and 3. Therefore in the following section, we only highlight the key differences in the Plasma-Aerosol model that have not been previously presented.

6.2.2 Plasma Module

The fluid plasma module solves for Poisson's equation, the electron continuity equation, the electron energy density equation, and positive and negative ion continuity equations.

Poisson's Equation

The Poisson's equation for the electric field is given by

$$\nabla^2 V = -\frac{e}{\varepsilon_0}\Big(\sum_i n_{i+} - \sum_i n_{i-} + Q_{NCP}\Big), \tag{6.1}$$

where V is the plasma electric potential, n_{i+} is the density of positively charged ions, n_{i-} is the density of negatively charged species (ions + electrons), and Q_{NCP} is the net charge density on dust particles.

Governing Equations for Electrons

The continuity equation for electron is given by

$$\frac{\partial n_e}{\partial t} = -\nabla \cdot \Gamma_e + S_e, \tag{6.2}$$

where S_e is the net source term due to electron attachment to particles and inelastic electron impact reactions. Γ_e is the electron flux using the drift-diffusion approximation,

$$\Gamma_e = -\mu_e n_e E - D_e \nabla n_e, \tag{6.3}$$

where E is the instantaneous electric field calculated by Poisson's equation, Eq. (6.1).

The electron energy distribution is assumed to be Maxwellian. The electron energy density equation is given by

$$\frac{\partial}{\partial t}\Big(\frac{3}{2}n_e kT_e\Big) + \nabla q_e = -e\Gamma_e E + S_{qe} - \sum_{size}\sum_{charge}\Big(N_{i,k}\nu_{e(i,k)}\phi_{i,k}\Big), \tag{6.4}$$

where q_e is the electron energy flux, S_{qe} represents the loss of electron energy in electron impact collisions with heavy species (not including aerosol particles), and q_e is the electron energy flux,

$$q_e = \frac{5}{2}kT_e\Gamma_e - \frac{5}{2}D_e n_e \nabla(kT_e). \tag{6.5}$$

The last term in Eq. (6.4) corresponds to the electron collisions with the nanoparticles where ν_e is the electron collision frequency and $\phi_{i,k}$ is the particle potential.

Governing Equations for Ions

Similar to electrons, the continuity equation for positive or negative ions is given by

$$\frac{\partial n_i}{\partial t} = -\nabla \cdot \Gamma_i + S_i. \tag{6.6}$$

The flux Γ_i uses the drift-diffusion approximation,

$$\Gamma_i = -\mu_i n_i \tilde{E} - D_i \nabla n_i, \tag{6.7}$$

where $\tilde{E}$ is the effective electric field. The reason for using an effective electric field for heavier species is that the drift-diffusion flux is derived by assuming that the inertial effects in the momentum equation are negligible−see Eq. (2.5) in chapter 2. In the RF frequency regime, this assumption is only valid for electrons, which have a small mass. For larger species, and to account for the inertia, an effective electric field was derived by Richards *et al.* [125] and given by

$$\frac{\partial \tilde{E}}{\partial t} = \frac{e}{\mu_i m_i}\Big(E - \tilde{E}\Big). \tag{6.8}$$

6.2.3 Aerosol Module

The aerosol module solves for the continuity equation of each size-charge combination. The sectional model is described in detail in Chapter 2. In Chapter 3, the particle flux is calculated by solving the momentum equation for each particles of each size-section

combination. In this model, since the drift-diffusion approximation is made, the particle flux is given by

$$\Gamma_{j,k} = \mu_{j,k}\tilde{E} - D_j \nabla N_{j,k} + \Gamma_F, \tag{6.9}$$

where the subscripts j and k represent section and charge states respectively, $\tilde{E}$ is the cycle averaged electric field when the plasma is ON and the effective electric field (Eq. (6.8)) in the afterglow when the plasma is OFF. The diffusion coefficient D_j is given by

$$D_j = \frac{1}{R^2 n_g}\sqrt{\frac{kT}{2\pi m_g}}\Big(\frac{3}{8}\Big)\Big(1+\frac{\pi}{8}\Big)^{-1} \tag{6.10}$$

and related to the mobility $\mu_{j,k}$ by the Einstein relation,

$$\mu_{j,k} = \frac{q_k D_j}{kT}, \tag{6.11}$$

where q_k is the particle charge. The last term of Eq. (6.9), Γ_F, is the flux due to the external forces and is given by

$$\Gamma_F = (F_{ID} + F_{ND})\Big(\frac{\mu_{j,k}}{e}\Big)N_{j,k}. \tag{6.12}$$

The ion drag force F_{ID} is the sum of the collection force (momentum transfer by ion-dust collisions) and the orbit force (momentum transfer by ion deflection due to the Coulomb potential). The collection force is given by [126]

$$F_c = \pi R^2 N_i m_i v_T \mathbf{v_i}\Big[1 - \frac{2e\phi_i}{m_i v_T^2}\Big], \tag{6.13}$$

where $\mathbf{v_i}$ is the ion drift velocity and the orbit force is given by [127]

$$F_0 = N_i m_i \sigma_0 v_T \mathbf{v_i}, \tag{6.14}$$

where σ_0 is the orbit momentum cross section for the cut off Coulomb potential,

$$\sigma_0 = 2\pi b_{\pi/2}^2 \ln\Big(\frac{\lambda_L^2 + b_{\pi/2}^2}{b_c^2 + b_{\pi/2}^2}\Big), \tag{6.15}$$

where b_c and $b_{\pi/2}$ represent the collection impact parameter and the impact parameter for ions whose asymptotic orbit angle is $\pi/2$.

Thermophoresis and gravitational forces are not included in this work.

Table 6.1: Hydrogen and silicon hydride species included in the chemistry model for silicon particle formation in H_2/SiH_4 plasmas.

Hydrogen species	
H	H^-
H_2	H^+
	H_2^+
	H_3^+
Silicon hydride species	
SiH	SiH^-
SiH_2	SiH_2^-
SiH_3	SiH_3^-
SiH_4	SiH_3^+

6.2.4 Chemistry Module

The formation of silicon nanoparticles in low-pressure plasmas occurs from chemical reactions that involve silicon hydride species. A set of reactions for hydrogen and silicon hydride chemistry is implemented. The species included in the model are in Table 6.1. There are 6 hydrogen and 8 silicon hydride species. It was shown that the vibrational states for hydrogen and silicon hydride could have a significant effect on the plasma chemistry and particle nucleation [89, 128, 129]. In the current work, vibrational states are not included in the model.

Electron impact and hydrogen species reactions are shown in Table 6.2 for a total number of 23 reactions. Electron impact and silicon hydride species reactions are shown in Table 6.3 for a total number of 26 reactions. All reaction rate constants are expressed in the Arrhenius form where the electron temperature is used for electron reactions and the gas temperature is used for heavy species reactions. Only the forward reactions are included in the chemistry model for electron and heavy species reactions.

The nucleation rate is defined a the sum of the rates of reaction 24−26 in Table 6.3. All reactions involve the negative ion SiH_3^- as it is expected to be the dominant anion in the system [129]. A silicon hydride species that contains 2 or more Si atoms is assumed to be a nanoparticle, which corresponds to a section 0.42 nm in diameter. The model also includes radicals for nanoparticle surface growth: SiH, SiH_2, SiH_3, SiH_3^+, and SiH_4.

Table 6.2: Electron impact and hydrogen species reactions included in the chemistry model for silicon particle formation in H_2/SiH_4 plasmas. Reaction rate constants are expressed in the Arrhenius form: $AT^{\beta}\exp(-E_a/T)$.

	Reaction	A (cm^3 s^{-1})	β	E_a (eV)	Ref.
Electron impact reactions					
1.	$e + H_2 \rightarrow H_2^+ + 2e$	1.10×10^{-08}	0.42	16.05	[130]
2.	$e + H_2 \rightarrow 2H + e$	4.73×10^{-08}	-0.23	10.09	[130]
3.	$e + H_2 \rightarrow H + H^-$	2.05×10^{-11}	-1.04	9.04	[130]
4.	$e + H \rightarrow H^+ + 2e$	7.89×10^{-09}	0.41	14.23	[130]
5.	$e + H_3^+ \rightarrow H_2^+ + H^-$	1.93×10^{-10}	-1.07	2.70	[130]
6.	$e + H^- \rightarrow H + 2e$	1.24×10^{-06}	0.03	10.44	[130]
7.	$e + H_3^+ \rightarrow 2H + H^+$	1.00×10^{-07}	0.37	14.46	[130]
8.	$e + H_2^+ \rightarrow 2H$	2.35×10^{-08}	0.40	00.00	[130]
9.	$e + H_3^+ \rightarrow 3H$	2.19×10^{-09}	0.80	00.00	[130]
10.	$e + H_3^+ \rightarrow H + H_2$	7.30×10^{-10}	0.80	00.00	[130]
11.	$e + H_2^+ \rightarrow H + H^+ + e$	1.88×10^{-07}	0.39	28.82	[130]
12.	$e + H_2 \rightarrow H + H^+ + e$	2.99×10^{-08}	0.44	37.73	[131]
13.	$e + H_2^+ \rightarrow 2H^+ + e$	2.12×10^{-09}	0.31	23.30	[131]
14.	$e + H_3^+ \rightarrow H_2^+ + H + e$	4.84×10^{-07}	-0.05	19.16	[131]
16.	$e + H_3^+ \rightarrow 2H + H^+ + e$	1.00×10^{-07}	0.37	14.46	[130]
Heavy species reactions					
17.	$H_2^+ + H \rightarrow H^+ + H_2$	5.08×10^{-10}	0.0	0.0	[130]
18.	$H^+ + H_2 \rightarrow H_2^+ + H$	3.32×10^{-10}	0.0	0.0	[131]
19.	$H_2^+ + H_2 \rightarrow H_3^+ + H$	2.10×10^{-09}	0.0	0.0	[130]
20.	$H^- + H^+ \rightarrow 2H$	3.00×10^{-07}	0.0	0.0	[128]
21.	$H^+ + 2H_2 \rightarrow H_3^+ + H_2$	3.20×10^{-10}	0.0	0.0	[128]
22.	$H^- + H_2^+ \rightarrow H + H_2$	3.50×10^{-06}	0.0	0.0	[128]
23.	$H^- + H_3^+ \rightarrow 2H_2$	3.50×10^{-06}	0.0	0.0	[128]

6.3 Charged Particle Transport in Pulsed Plasmas

6.3.1 Model Schematic

The schematic of the set up modeled in this work is shown in Fig. 6.2. It is a parallel-plate capacitively-coupled RF plasma system separated by a 2-cm gap. The plasma conditions are a pressure of 2 Torr, a constant gas temperature at 300 K, and a gas mixture of H_2/SiH_4=95/5, The gas flow rate is 30 sccm, which corresponds to an inlet gas velocity is 1.7 cm s^{-1} for 12-cm-diameter electrodes.

When the plasma is ON (see Fig. 6.2(top)), the plasma is powered at the top

Table 6.3: Electron impact reactions, silicon hydride species reactions, and nucleation reactions included in the chemistry model for silicon particle formation in H_2/SiH_4 plasmas. Reaction rate constants are expressed in the Arrhenius form: $AT^{\beta}\exp(-E_a/T)$.

	Reaction	A (cm^3 s^{-1})	β	E_a (eV)	Ref.
Electron impact reactions					
1.	$e + SiH_4 \rightarrow SiH_3 + H + e$	1.83×10^{-03}	-1.0	10.68	[132]
2.	$e + SiH_4 \rightarrow SiH_2 + 2H + e$	8.97×10^{-03}	-1.0	10.68	[132]
3.	$e + SiH_4 \rightarrow SiH_3^- + H + e$	3.77×10^{-03}	-1.63	8.29	[44]
4.	$e + SiH_4 \rightarrow SiH_2^- + 2H + e$	3.77×10^{-03}	-1.63	8.29	[44]
5.	$e + SiH_3 \rightarrow SiH_2^- + H + e$	5.71×10^{-03}	-0.5	1.94	[132]
6.	$e + SiH_2^- \rightarrow SiH_2 + 2e$	3.15×10^{-10}	0.5	1.16	[85]
7.	$e + SiH_3^- \rightarrow SiH_3 + 2e$	3.15×10^{-10}	0.5	1.16	[85]
8.	$e + SiH_2 \rightarrow SiH_2^-$	5.71×10^{-10}	-0.5	0.0	[132]
9.	$e + SiH_3 \rightarrow SiH_3^-$	5.71×10^{-10}	-0.5	0.0	[132]
10.	$e + SiH_4 \rightarrow SiH_3^+ + H + 2e$	$2.50\times10^{+08}$	-2.93	24.1	[132]
11.	$e + SiH_3 \rightarrow SiH_3^+ + 2e$	2.26×10^{-10}	0.5	1.30	[132]
12.	$e + SiH \rightarrow SiH^-$	5.71×10^{-09}	-0.5	0.0	[85]
13.	$e + SiH^- \rightarrow SiH + 2e$	3.16×10^{-10}	0.5	1.25	[85]
Heavy species reactions					
14.	$SiH_2^- + SiH_3 \rightarrow SiH_2 + SiH_3$	1.27×10^{-10}	0.0	0.0	[44]
15.	$SiH_2 + H_2 \rightarrow SiH_4$	1.00×10^{-14}	0.0	0.0	[133]
16.	$SiH_4 + H \rightarrow H_2 + SiH_3$	2.44×10^{-16}	1.9	0.09	[132]
17.	$SiH_3 + H \rightarrow SiH_2 + H_2$	2.49×10^{-11}	0.0	0.11	[132]
18.	$SiH_2^- + H_2^+ \rightarrow SiH_2 + H_2$	5.55×10^{-06}	-0.5	0.0	[44]
19.	$SiH_3^- + H_2^+ \rightarrow SiH_3 + H_2$	5.55×10^{-06}	-0.5	0.0	[44]
20.	$SiH_2^- + SiH_3 \rightarrow SiH_2 + SiH_3^-$	1.27×10^{-10}	0.0	0.0	[44]
21.	$SiH_2 + H \rightarrow SiH + H_2$	2.31×10^{-11}	0.0	0.0	[132]
22.	$SiH_2^- + SiH \rightarrow SiH_2 + SiH^-$	2.31×10^{-11}	0.0	0.0	[44]
23.	$SiH^- + H_2^+ \rightarrow SiH + H_2$	3.21×10^{-07}	0.0	0.0	[44]
Nucleation reactions*					
24.	$SiH_3^- + SiH_3 \rightarrow NP + H_2$	5.27×10^{-11}	0.0	0.0	calc.**
25.	$SiH_2^- + SiH_4 \rightarrow NP + H_2$	5.27×10^{-11}	0.0	0.0	calc.**
26.	$SiH_3^- + SiH_3^+ \rightarrow NP + H_2$	4.87×10^{-07}	-0.5	0.00	[44]

* NP represents a nanoparticle

** Rate coefficients are estimated to be 0.1 of the Langevin rate.

electrode with a RF voltage V_{RF}=100V at 13.56 MHz while the bottom electrode is grounded. The self-induced DC bias at the top electrode is self-consistently calculated by the model. When the plasma is OFF, V_{RF}=0 V and a DC bias is applied at the bottom electrode. To attract the negatively charged particles, a positive DC bias V_B=400 V is applied. The pulse period is 3 ms and the duty cycle is 0.75, so that the plasma is ON for 2.25 ms and OFF for 0.75 ms. To avoid numerical issues, the DC bias is only applied 0.1 ms after the plasma is turned off, at 2.35 ms for these simulations. All results presented in this chapter are for this set of plasma conditions. We examined the system behavior during the first cycle of the pulsed plasma only. During the first pulse, the plasma has not reached its quasi-periodic steady-state yet and therefore quantitative results may be different than the solution at longer times.

To describe the spatiotemporal evolution of the nanoparticles in the afterglow, most of the results shown start when the DC bias is applied at 2.35 ms. In figures, if not specified, this time is defined as t=0 μs. In figures, the powered-electrode position is at 2 cm and the grounded electrode at 0 cm.

6.3.2 Plasma ON: Particle Growth and Transport

The plasma is sustained due to the ionization of the background gas by energetic electrons that gain their energy through ohmic heating. When the simulation starts, the H_2 density is initialized so that the background gas is at 2 Torr, while electron, charged, and neutral species have an initial density of 0 cm^{-3}. At the inlet, the initial density of H_2 and SiH_4 is chosen to be H_2/SiH_4=95/5. Then the spatiotemporal evolution of all species is calculated by solving their continuity equations, along with the Poisson's equation for the electric field. The ionization rate peaks in the sheath where most of the power is dissipated and the electron temperature is the highest [134]. The plasma is ON from 0 to 2.25 ms and the species densities, as well as the nanoparticle densities, increase as the ionization rate increases, producing more radicals available for chemical reactions to occur. Electron impact dissociation of silane produces silicon hydride species that can react with each other and leads to the nucleation of small nanoparticles. Fig. 6.3 shows the spatial distribution of (left) charged and (right) neutral gas-phase densities for hydrogen and silicon hydride species at 2.25 ms, just before turning off the plasma. At the center of the discharge (1 cm), the electron density is 1.1×10^{10} cm^{-3}, the density

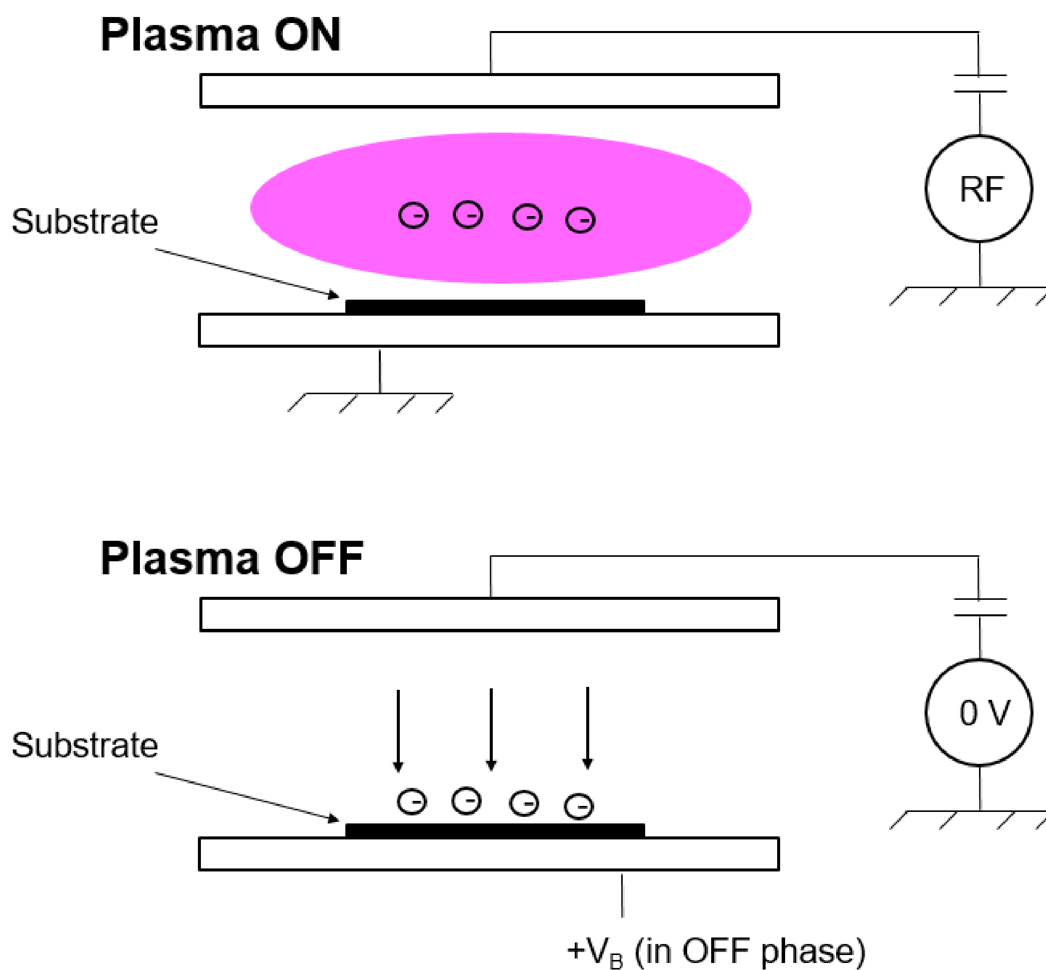

Figure 6.2: Schematic of the parallel-plate capacitively-coupled RF plasma system. When the plasma is ON, the electric field traps the negatively charged particles at the center of the discharge. When the plasma is turned OFF, a positive DC bias V_B is applied at the substrate to accelerate the negative nanoparticles. By changing the plasma conditions and V_B, the nanoparticle flux and impact energy can be tuned.

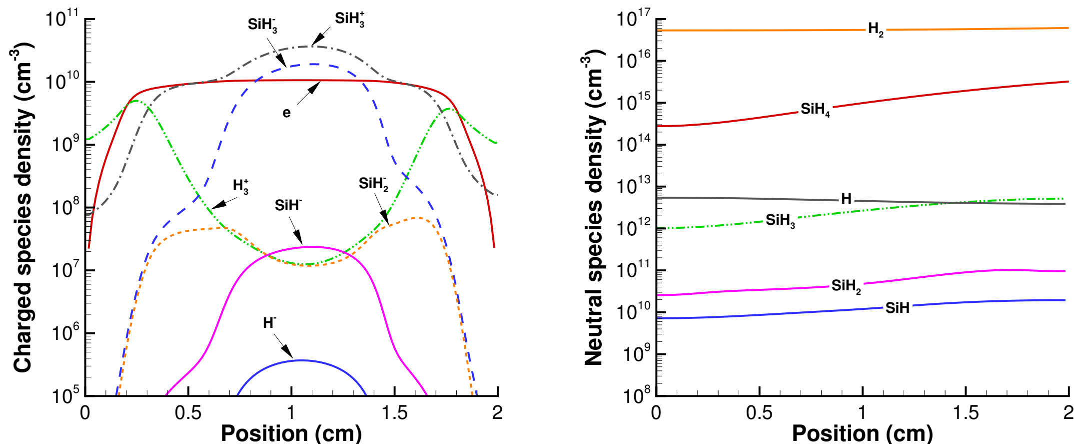

Figure 6.3: Species densities just before turning off the plasma for (left) electron, positive and negative ions, (right) neutrals.

of SiH_3^+ is 3.5×10^{10} cm^{-3}, and the density of SiH_3^- is 1.8×10^{10} cm^{-3}, corresponding to an electron-to-ion density ratio of n_e/n_i=0.31, and therefore the plasma is electronegative. It is important to remember that because the simulation has not reached the quasi-periodic steady-state, the species densities are lower than their expected values in the long run. As a matter of fact, we ran a pristine plasma case up to steady-steady state under the same set of plasma conditions, and found that both SiH_3^- and SiH_3^+ were an order of magnitude greater than the electron density.

In hydrogen plasma discharges and under similar conditions, Novikova and coworkers showed that H_3^+ was the dominant positive ion [134, 128]. To benchmark our model, we conducted simulations under the same conditions as their work and arrived at the same conclusion. The effects of pressure, RF potential, and RF frequency were also studied to make sure that the model behaved properly.

When adding silane to hydrogen in the reactor, the spatial distributions of the species are strongly different than for the pure hydrogen plasma. At the center of the discharge, SiH_3^+ becomes the dominant positive ion and the H_3^+ density is 1.3×10^7 cm^{-3} which is negligible compared to SiH_3^+. However in the sheath, H_3^+ is the dominant ion−at 0.2 cm from the substrate, the density of H_3^+ is 4.2×10^9 cm^{-3} and the density of SiH_3^+ is

5.6×10^8 cm^{-3}. This observation is explained by chemical reactions between hydrogen and silicon hydride species. The dominant reaction for H_3^+ production is

$$H_2^+ + H_2 \rightarrow H_3^+ + H, \tag{6.16}$$

where H_2^+ is mostly produced by electron impact reaction with hydrogen. The species H_2^+ is highly reactive with the negative species SiH_2^- and SiH_3^-,

$$SiH_2^- + H_2^+ \rightarrow SiH_2 + H_2, \tag{6.17a}$$

$$SiH_3^- + H_2^+ \rightarrow SiH_3 + H_2, \tag{6.17b}$$

that peak in densities at the center of the discharge. Because they are negatively charged, their densities in the sheath are negligible and H_3^+ has a higher density.

The favorable pathway to nucleation occurs through the negative and positive ions SiH_3^- and SiH_3^+ since they are the dominant species in the system. This conclusion was discussed by De Bleecker *et al.* in silane plasmas under similar conditions [129]. In such plasma reactors, particles that are negatively charged are trapped at the center of the discharge by the electric field. Their residence time is much larger than that of neutral and positive nanoparticles. Therefore, negatively charged particles grow to higher sizes. Because of Coulomb repulsion, only neutral and positively charged species can deposit on surfaces of negatively charged nanoparticles. Fig. 6.3(right) shows the spatial distribution of the neutral species. The density of SiH_3 is almost two order of magnitude greater than SiH_2 so that SiH_3 is the dominant species for surface growth. The density of SiH_4 decreases with the distance from the inlet as it gets dissociated while flowing through the discharge.

In the plasma ON phase, particles grow to sizes that would depend on the plasma conditions and the plasma ON time. Fig. 6.4 shows the spatial distribution of (left) the particle size distribution and (right) the density of positive, neutral, and negative nanoparticles. The particle diameter distribution peaks at ~1 nm at the center of the discharge. The negatively charged particle density is greater compared to neutral and positive particles at the center of the discharge. Because of the electric field, negatively charged particles are trapped at the center of the discharge and the neutral particle density is larger than that of negative nanoparticles in the sheath.

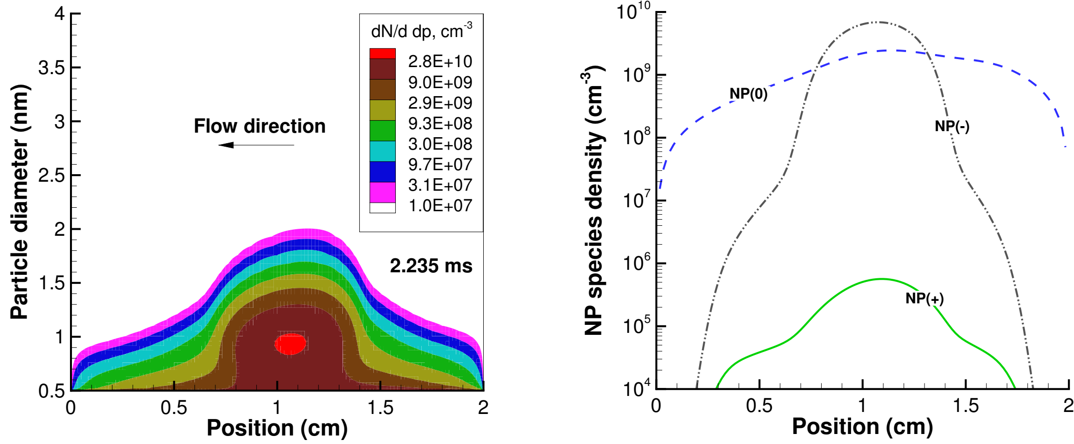

Figure 6.4: Nanoparticle spatial distribution just before turning off the plasma for (left) nanoparticle size distribution, (right) positive, negative, and neutral nanoparticles.

During the first pulse, particle size and particle density are not high enough to deplete the electron density by electron attachment. In fact, the nanoparticle cloud is strongly coupled to the plasma for particle sizes that are much larger than the ones considered in this work, as shown by Agarwal and Girshick [11].

6.3.3 Plasma OFF: Particle Dynamics in the Afterglow

In these simulations, the pulse period is set so that the plasma is ON for 2.25 ms, OFF for 0.1 ms, and then a DC bias V_B=400 V is applied at the substrate for 0.65 ms. Fig. 6.5 shows the spatiotemporal evolution of the densities of positive, neutral, and negative nanoparticles, along with the total positive and negative ions at 0, 50, 150 and 200 μs. The time 0 μs corresponds to the time when V_B is applied. At this time, charged species have not fully diffused to the wall or recombined and their densities are still high ($>10^6$ cm^{-3}) since the time scale for diffusion and recombination can be over 100 μs [135] at this pressure. We conducted simulations that show that under these plasma conditions, the electron density becomes negligible within 150 μs. Because the electron density at 0 μs is still high, the sheaths remain near the electrodes. As soon as the positive DC bias is applied at the substrate, the potential in the plasma changes and tends to accelerate

the negative species (i.e., electron, negative ions, and negative nanoparticles) towards the substrate. Fig. 6.5 shows that even a high fraction of positively charged species are directed to the substrate as a result of ambipolar diffusion. There is a wave-like movement of the negative nanoparticles and anions that propagates to the substrate, from 1 cm at 50 μs to 0.25 cm at 200 μs, after which all negatively charged species have been collected. On the right size of this ambipolar field, a positive space charge forms producing a high electric field. The speed with which all particles are collected should vary with the external parameters, including the gas pressure and the DC bias applied. It is expected that the higher the DC bias, the faster the collection process would be [14]. Using plasma conditions at the center of the discharge, the time scale for SiH_3^+ collision with a 1-nm-diameter singly-charged negative particle is roughly ~500 μs, when the time required to collect all negatively charged particle at the substrate is ~200 μs. Therefore, charge fluctuation does not play a significant role during the particle collection process.

As mentioned, when the DC bias is applied at the substrate, the electron density is still substantially high. Fig. 6.6 shows the spatiotemporal evolution of (left) the electron density and (right) the electron temperature from 0 to 5 μs after the DC bias is applied. At 3 μs, the electron density peaks at 0.25 cm from the substrate before most electrons have been collected at 5 μs. When the plasma is turned off at 2.25 ms, the electron temperature decreases down to room temperature within a few μs. However, because of the high electron density remaining in the plasma when the DC bias is applied, a current of electrons occurs in the discharge and the electron temperature rises up to 1 eV at 1 μs and 3 eV at 5 μs near the substrate.

During these 5 μs, the presence of electrons guides the plasma behavior. The spatiotemporal evolution of (left) total negative ions and (right) total positive ions are shown in Fig. 6.7 from 0 to 5 μs. The total negative ion density is increased from 7.8×10^3 cm^{-3} at 0 μs to 7.4×10^8 cm^{-3} at 5 μs at 0.2 cm from the substrate. The reason for the increase is merely due to the positive DC bias that attract the negative species. However, this observation is the opposite for the positive ion density. From 0 to 1 μs, the density increases from 1.1×10^8 cm^{-3} at 0 μs to 2.1×10^9 cm^{-3} at 1 μs at 0.2 cm from the substrate. Then at the same location, the density decreases to 7.8×10^8 cm^{-3} at 5 μs. The increase in positive ion density in this 1 μs is due to the fast increase

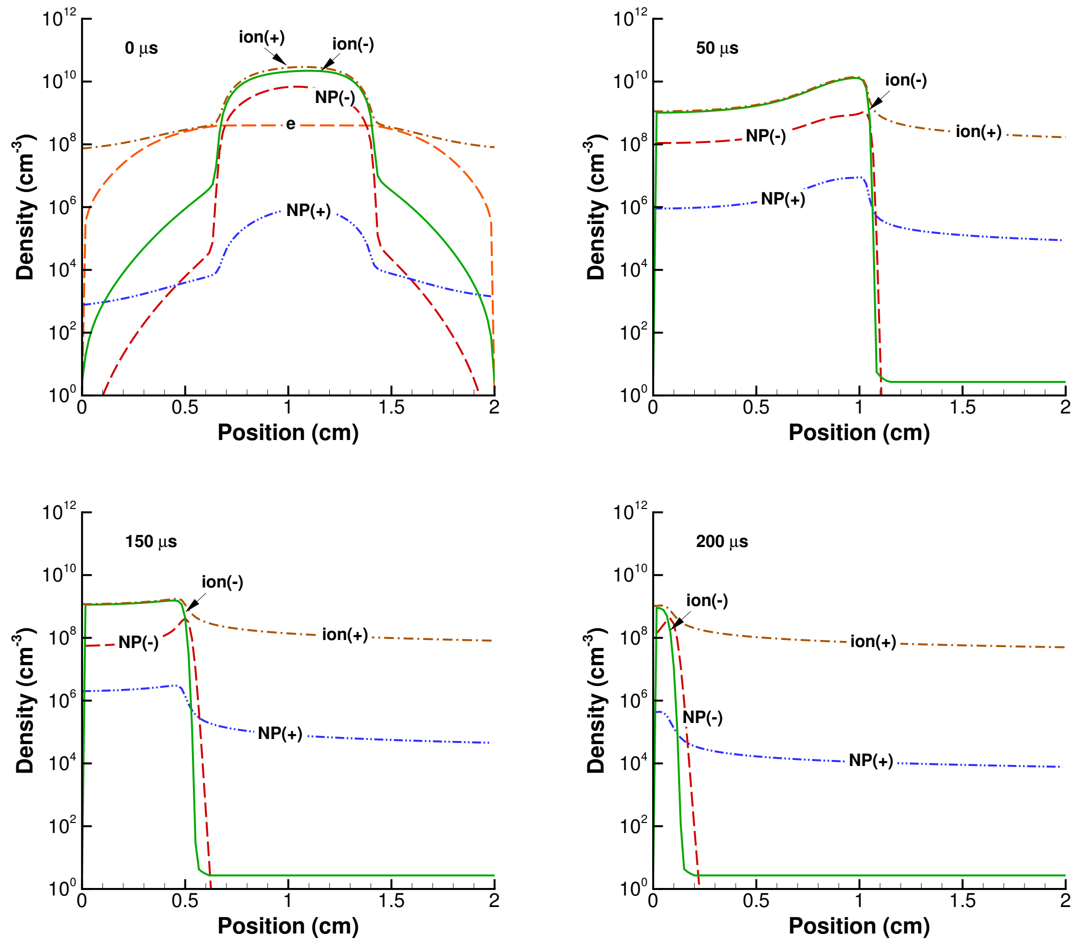

Figure 6.5: Spatiotemporal evolution of positive and negative ions and nanoparticles in the plasma OFF phase when the DC bias is applied at the substrate with V_B=400V. The time 0 μs corresponds to the moment V_B is applied.

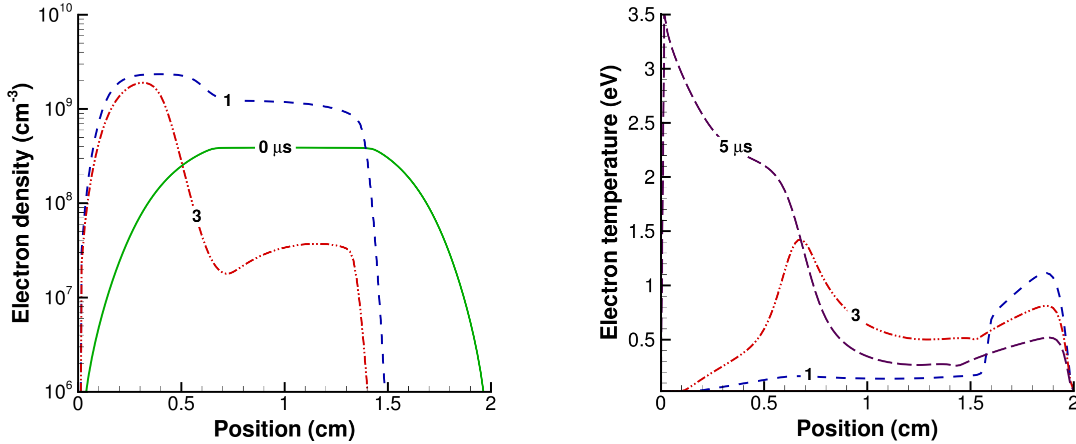

Figure 6.6: Spatiotemporal (0−5 μs) evolution of (left) electron density and (right) electron temperature in the plasma OFF phase when the DC bias is applied at the substrate with V_B=400V. The time 0 μs corresponds to the moment V_B is applied.

in electron density and temperature in this region of the discharge. This increases the ionization of H_2, hence producing more H_2^+ and H_3^+. Once the electrons are removed from the reactor, ionization ceases and the positive ion density decreases. Note that during the period 0−1 μs, the density of SiH_3^+ decreases so that the overall increase in positive ion density is due to H_3^+.

The DC bias is chosen to be positive to accelerate negative nanoparticle to the substrate. To understand the mechanisms of nanoparticle transport, it is therefore instructive to look at the plasma electric potential and the plasma electric field across the discharge, as shown in Fig. 6.8 up to 50 μs after the DC potential is applied. While V_B=+400 V, the potential is screened by the presence of charged species in the plasma. From 0 to 5 μs, the electron density and temperature is high and a sheath can be observed at the substrate during this time interval−the potential drop is ∼15 V. When the electrons are out of the reactor (>5 μs), the sheath disappears and the substrate potential is greater than the plasma potential. However, in the region where the negative ion density is significant, and because of the quasi-neutrality forced by the Poisson's equation, the electric potential is relatively constant.

The same conclusions can be observed from the electric field behavior shown in Fig.

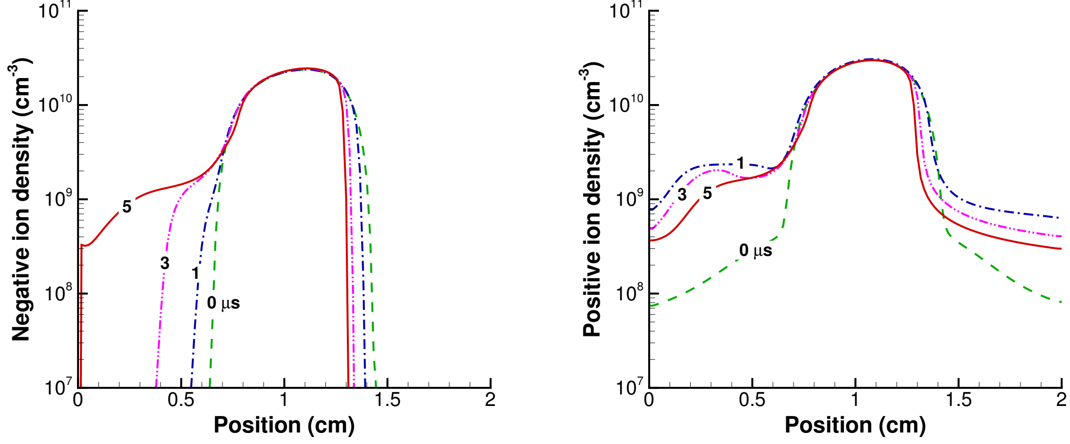

Figure 6.7: Spatiotemporal (0−5 μs) evolution of (left) negative and (right) positive ions in the plasma OFF phase when the DC bias is applied at the substrate with V_B=400V. The time 0 μs corresponds to the moment V_B is applied.

6.8(right). From 0 to 5 μs, the electric field at the surface is negative and negatively charged particles would not be collected at the substrate. The surface electric field is -200 V/cm at 0 μs and increases to +150 V/cm at 10 μs when all the electrons are out of the system. As the sheath disappears, negative ions and negatively charged particles transport toward the substrate, and the forced quasi-neutrality reduces the electric field to lower values $\sim$ +50 V/cm. This value is much smaller than the expected value of +200 V/cm (i.e. +400 V in a 2-cm gap reactor).

6.3.4 Particle Impact Energy on Substrate

The particle impact energy can be tailored by varying the plasma conditions as well as the applied DC bias V_B at the substrate [14]. A higher impact energy is expected as the bias voltage increases. At low pressure, the nanoparticle gain in kinetic energy is proportional to V_B, but as the pressure increases, the collision with the background gas produces less energetic particles. The impact energy distribution F_{np} is calculated from the flux of negative nanoparticle to the substrate as

$$F_{np}(\varepsilon) = \frac{1}{T}\int_0^T \frac{\Gamma(t,\varepsilon)}{\Gamma_T}dt, \tag{6.18}$$

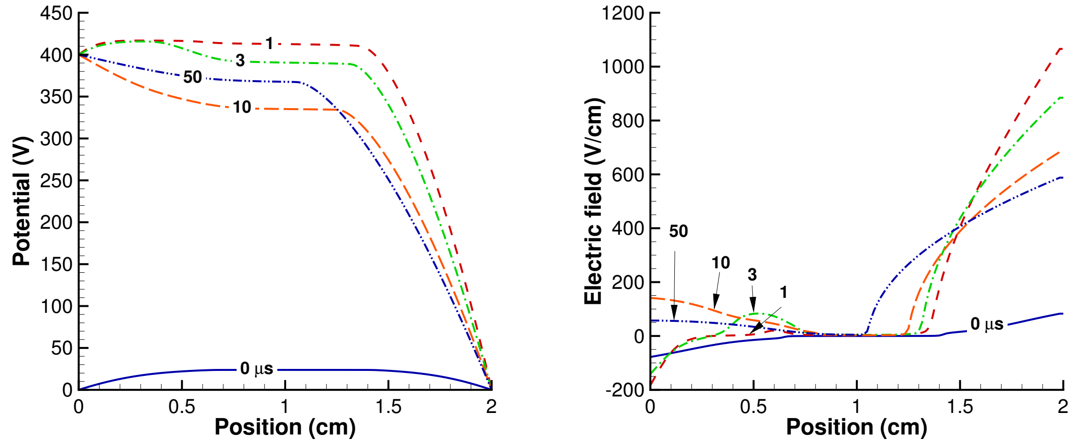

Figure 6.8: Spatiotemporal (0−50 μs) evolution of (left) plasma potential and (right) electric field in the plasma OFF phase when the DC bias is applied at the substrate with V_B=400V. The time 0 μs corresponds to the moment V_B is applied.

where T is the afterglow period, ε is the impact energy per atom, Γ is the instantaneous particle flux at the substrate, and Γ_T is the overall particle deposition per unit area at the substrate that is integrated over the entire afterglow period as

$$\Gamma_T = \int_0^T \int_0^\infty \Gamma(t,\varepsilon) d\varepsilon dt. \quad (6.19)$$

The particle flux is expressed using the electric field at the surface and the particle mobility as

$$\Gamma_{i,k} = \mu_{i,k} N_{i,k}(t) \tilde{E}_s(t,\varepsilon), \quad (6.20)$$

In Fig. 6.9(right), the negative nanoparticle flux and the effective electric field for a 1.27-nm-diameter particle are compared. The flux is the highest from 5 to 60 μs when the electric field is above 50 V/cm. In this short time period, nanoparticles of this size are singly charged and hit the substrate with an impact energy greater than 2 eV, and then the electric field decreases, leading to lower nanoparticle impact energy.

The impact energy distribution averaged over the entire afterglow for all particle size and charge state is shown in Fig. 6.10. Only negatively charged particles that

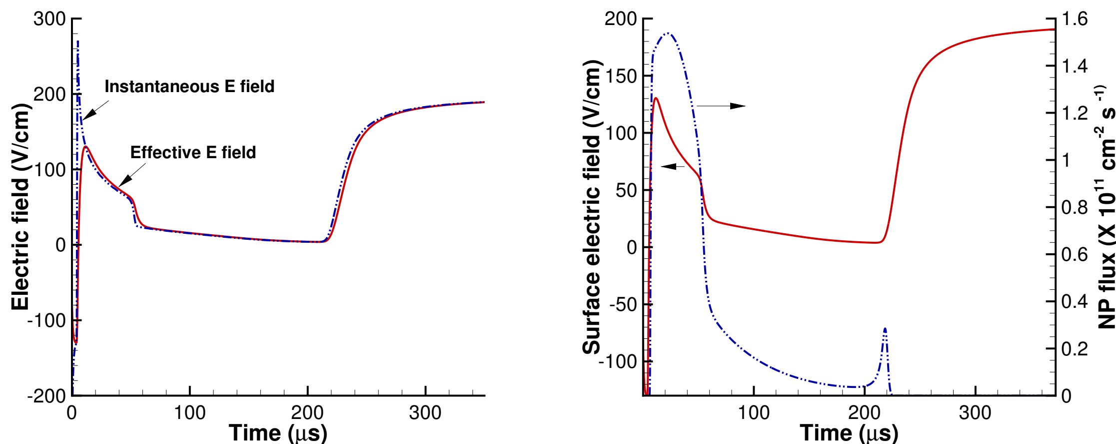

Figure 6.9: Temporal evolution at the substrate of (left) instantaneous and effective electric fields and (right) effective electric field and negative nanoparticle flux in the plasma OFF phase for a 1.27-nm-diameter particle when the DC bias is applied at the substrate with V_B=+400V. The time 0 μs corresponds to the moment V_B is applied.

are larger than 1 nm diameter are used to produce the impact energy distribution. Most nanoparticles have low energy because of the low surface electric field. The peaks correspond to the different discrete charge states (physical meaning), as well as the discrete nature of the sectional model (numerical approximation).

6.4 Conclusion

In this chapter, a one-dimensional fluid model of a parallel-plate capacitively-coupled RF plasma was developed in H_2/SiH_4 at 2 Torr. The model was based on the Aerosol-Plasma code developed by Girshick and coworkers.

A hydrogen and silicon hydride chemistry was implemented and the nucleation rate of small nanoparticles was self-consistently calculated from the chemical reactions, assuming SiH_3^- as the precursor species for nucleation. Positive and neutral silicon hydride species were allowed to deposit on nanoparticle surfaces. Nanoparticle transport, charging, and growth processes, were included and the nanoparticle cloud was coupled to the plasma.

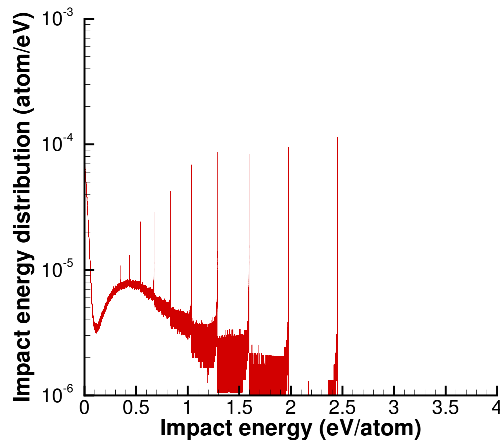

Figure 6.10: Impact energy distribution (atom/eV) at the substrate when the DC bias is applied at the substrate with V_B=400V. The distribution is averaged over the entire plasma OFF phase period.

Using pulsed plasmas, we studied plasma behavior and nanoparticle transport in the afterglow. In the OFF phase, a positive DC bias of 400 V was applied to the substrate to attract. Negative nanoparticles have a larger density compared to positive and neutral nanoparticles, due to the larger electron mobility compared to ions that would charge particle negatively. We found that because of the strong coupling between the charged species densities and the field, the applied bias potential was screened leading to a relatively low electric field in the plasma and at the substrate. Therefore the nanoparticle did not get a significant kinetic energy when hitting the substrate (<1 eV/atom). Under these plasma conditions, particles are all collected to the substrate in ∼200 μs, while the time between a positive ion and a negatively-charged particle is ∼500 μs. Therefore, charge fluctuations does not play a significant role during the particle collection time.

This work examined plasma and particle transport behavior in the first pulse only, when the plasma has not reached its quasi-periodic steady-state solution. Therefore these results presented in this work are only preliminary and may differ quantitatively from the solution at longer times. Impact energy distribution considers particle that are negatively charged and larger than 1 nm in diameter. When running the code for

more than one pulse, particles do grow to larger sizes as their residence time in the plasma increases, and lower impact energy are expected, since larger particles contain more atoms.

As future work, simulations should be run for a few pulses to reach a quasi-periodic steady-state. A more detailed set of reactions should be implemented to better estimate the spatial distribution of silicon hydride species as they play a significant role in nucleation and surface growth reactions. In this work, the assumptions on plasma chemistry were based on the work by Bhandarkar *et al.* that studied silicon hydride reactions in low-pressure plasmas [44]. The pressure for their base case conditions was 100 mTorr, while a pressure of 2 Torr is used in this chapter. Therefore the pathway to nucleation may be different in this work.

Finally, a parametric study on pressure, DC bias, and time of the period ON and OFF phase should be conducted to fully understand the set-up and to be able to use the model as a predictive tool. The set of reactions could be improved to obtain more quantitative results and compare them with ongoing experiments in the group of Roca i Cabarrocas at Ecole Polytechnique (Paris, France).

Chapter 7

Conclusion

In this work, dust particle formation, growth, charging, and transport were studied by developing numerical models.

In chapter 3, a numerical model was developed to study the mechanisms of silicon particle formation in a capacitively-coupled RF flowing plasma, following the experimental setup designed by Kortshagen and coworkers. An aerosol module was added into the 2-dimensional fluid code developed by Kushner and coworkers, the Hybrid Plasma Equipment Model (HPEM). The aerosol module calculates the rate coefficients for particle growth (i.e., coagulation and radical deposition on particle surface) and particle charging. The continuity and momentum equation is solved for all particle size-charge combinations within a sectional model framework. This model returns the size and charge distribution at every single mesh point. A detailed set of reactions for $Ar/He/SiH_4$ was implemented and coupled to the nanoparticle cloud. The results show that particles grow as they flow without being trapped in the axial direction. Nucleation and surface growth rates peak between the two electrodes where the production of radicals is the greatest. The internal nanoparticle temperature is not in thermal equilibrium with the background gas and can reach values that are a few hundred Kelvin higher than the gas temperature. Solving for nanoparticle temperature fluctuations at every mesh point, we show that their temperature can be above the crystallization temperature and therefore we show the possibility of producing silicon nanocrystals in this setup, as observed experimentally.

Particle growth and transport are strongly coupled to particle charge. In typical cold

plasmas, particles are mostly negatively charged due to the greater electron mobility compared to that of ions, while a fraction of particles can be neutral or positively charged due to charge fluctuations. The number of electrons that a particle can hold is limited by its material composition and its size. We derived an analytical expression for steady-state charge distributions in low-pressure plasmas accounting for particle charge limits. In chapter 4, we presented the particle-charge-limited regime where the effects of charge limits on charge distributions are the most important. We found that charge limits effects are largest when the electron-to-ion density ratio is $0.1 < n_e/n_i < 1$.

Particle deposition on wafer surfaces during plasma processing is often observed. In Chapter 5, we developed a 0-dimensional Monte Carlo charging model to calculate particle charge distributions under given plasma conditions. The model includes electron and ion currents to particles, effect of pressure on the ion current, electron emission processes, and particle charge limit. Under typical plasma deposition conditions, we found that the pressure regime $1 - 10$ Torr produces the highest fraction of neutral and positive particles up to 100 nm in diameter. Electronegative plasmas are often used and therefore the electron-to-ion density ratio can be much less than unity, which causes the fraction of non-negative particles to increase. Charge limits have less significant effects in electronegative plasmas.

The Aerosol-Plasma code was originally developed by Girshick and coworkers to model a parallel-plate capacitively-coupled RF plasma in Ar/SiH_4 at low pressure (< 100 mTorr). In chapter 6, we modified the code and chemistry to study silicon particle formation, growth, charging, and transport, in H_2/SiH_4 pulsed plasma at 2 Torr. We studied the transport of particles in the afterglow and show that there is a strong coupling between positive and negative particles. In the plasma region, where the particle density is high, the electric field is relatively low (< 50 V/cm) and almost independent of the DC bias applied at the substrate. Therefore, even though negative particles are accelerated by the positive DC bias, the electric force produces mostly low per-atom impact energies at the substrate (1 eV). The chapter reports a preliminary study, exploring the very first pulse for a given set of conditions. Further simulations are conducted to reach a quasi steady-state solution after a few pulses.

While developing a numerical model, assumptions are made to overcome computational limitations. For example in Chapter 3, even by using the best resources available at the Minnesota Supercomputing Institute [39], each simulation took around four months of calculations. Many assumptions had to be made, such as on the numerical mesh, the number of species and reactions to include, and the number of size-charge combinations that could be computed in the sectional model.

Particle size distribution can be calculated within a sectional framework, as done in this work, with the main advantage that the form of the distribution does not need to be known *a priori*. This method is more effective than a discrete model as the number of equations can be significantly reduced. In systems where size distribution are expected to be known (e.g. normal distribution), the method of moments can be used in plasmas [61, 136]. This method has the advantage of being very fast since it requires to solve only a few equations simultaneously. Even though particle charging has significant effects on plasma behavior, we are not aware of any work that include particle charging within the method of moment. Such a method would be of great interest where nanoparticle nucleate and grow in plasmas.

In typical low-pressure plasma conditions, the formation of nanoparticles occurs through a polymerization chain of reactions producing small clusters. The assumptions made on the plasma chemistry in Chapters 3 and 6 were based on the work by Bhandarkar *et al.* that studied silicon hydride reactions in low-pressure plasmas [44]. Model and results of their work was for a silane plasma at 100 mTorr, while the pressure is around 2 Torr in our studies. This difference in pressure, along with reactor geometry effects, the leading reactions and pathway to nucleation may differ from their results. Future models of similar set-up to Chapters 3 and 6 should implement a more detailed chemistry. Recently, reaction mechanisms at an atomistic level of anion-neutral silicon hydride reactions responsible for nucleation were studied by means of *ab initio* calculations [45]. They found that important chemical reactions do occur in three steps while many work assume a one-step process. Additional intermediate species should be added to plasma chemistry to account for multi-step processes.

The radical sticking coefficients on particle surface used in this work were found in the literature. They were either measured experimentally for bulk material on flat surfaces or estimated. The effects of particle curvature and material properties at small

particle sizes may cause sticking coefficients to significantly differ from its bulk properties. Future work should focus on finding better estimates of sticking coefficients. A possible approach would be to use Molecular Dynamics simulations [137].

Experiments should be conducted to improve the models and use them as predictive tools. Possible measurements include optical emission spectroscopy and electrostatic probe to measure electron temperature, electron density, and ion density.

References

[1] N Meyer-Vernet. Flip-flop of electric potential of dust grains in space. *Astronomy and Astrophysics*, 105:98–106, 1982.

[2] X Gao, Y Cui, RM Levenson, LWK Chung, and S Nie. In vivo cancer targeting and imaging with semiconductor quantum dots. *Nature biotechnology*, 22(8):969–976, 2004.

[3] S Askari, I Levchenko, K Ostrikov, P Maguire, and D Mariotti. Crystalline si nanoparticles below crystallization threshold: effects of collisional heating in non-thermal atmospheric-pressure microplasmas. *Applied Physics Letters*, 104(16):163103, 2014.

[4] I Denysenko, MY Yu, K Ostrikov, and A Smolyakov. Spatially averaged model of complex-plasma discharge with self-consistent electron energy distribution. *Physical Review E*, 70(4):046403, 2004.

[5] SJ Warthesen and SL Girshick. Numerical simulation of the spatiotemporal evolution of a nanoparticle–plasma system. *Plasma Chemistry and Plasma Processing*, 27(3):292–310, 2007.

[6] MJ Kushner. Hybrid modelling of low temperature plasmas for fundamental investigations and equipment design. *Journal of Physics D: Applied Physics*, 42(19):194013, 2009.

[7] A Gallagher. Model of particle growth in silane discharges. *Physical Review E*, 62(2):2690, 2000.

[8] JE Allen. Probe theory-the orbital motion approach. *Physica Scripta*, 45(5):497, 1992.

[9] M Gatti and U Kortshagen. Analytical model of particle charging in plasmas over a wide range of collisionality. *Physical Review E*, 78(4):046402, 2008.

[10] GJM Hagelaar. Bolsig+: User-friendly solver for electron boltzmann equation. *Download available at http://www. laplace. univ-tlse. fr*, 2008.

[11] P Agarwal and SL Girshick. Sectional modeling of nanoparticle size and charge distributions in dusty plasmas. *Plasma Sources Science and Technology*, 21(5):055023, 2012.

[12] L Ravi and SL Girshick. Coagulation of nanoparticles in a plasma. *Physical Review E*, 79(2):026408, 2009.

[13] P Agarwal and SL Girshick. Numerical modeling of an rf argon–silane plasma with dust particle nucleation and growth. *Plasma Chemistry and Plasma Processing*, 34(3):489–503, 2014.

[14] C Larriba and SL Girshick. Controlled fluxes of silicon nanoparticles to a substrate in pulsed radio-frequency argon-silane plasmas. *In preparation*.

[15] JC Metcalfe and MBC Quigley. Heat transfer in plasma-arc welding. *Welding Journal*, 54(3):99–103, 1975.

[16] S Ramakrishnan and MW Rogozinski. Properties of electric arc plasma for metal cutting. *Journal of Physics D: Applied Physics*, 30(4):636, 1997.

[17] VRT Narayanan. *Numerical modeling of post current-zero dielectric breakdown in a low voltage circuit breaker*. PhD thesis, University of Minnesota, 2014.

[18] A Bouchoule. *Dusty plasmas: physics, chemistry, and technological impacts in plasma processing*. John Wiley & Sons Inc, 1999.

[19] GS Selwyn. A phenomenlogical study of particulates in plasma tools and processes. *Japanese journal of applied physics*, 32(6S):3068, 1993.

[20] NJ Kramer. *Synthesis and Doping of Silicon Nanocrystals for Versatile Nanocrystal Inks*. PhD thesis, University of Minnesota, 2015.

[21] CB Murray, DJ Norris, and MG Bawendi. Synthesis and characterization of nearly monodisperse cde (e= sulfur, selenium, tellurium) semiconductor nanocrystallites. *Journal of the American Chemical Society*, 115(19):8706–8715, 1993.

[22] KA Littau, PJ Szajowski, AJ Muller, AR Kortan, and LE Brus. A luminescent silicon nanocrystal colloid via a high-temperature aerosol reaction. *The Journal of Physical Chemistry*, 97(6):1224–1230, 1993.

[23] PE Batson and JR Heath. Electron energy loss spectroscopy of single silicon nanocrystals: the conduction band. *Physical review letters*, 71(6):911, 1993.

[24] M Ehbrecht and F Huisken. Gas-phase characterization of silicon nanoclusters produced by laser pyrolysis of silane. *Physical Review B*, 59(4):2975, 1999.

[25] K Lee and T Matsoukas. Can charge fluctuations explain particle growth in low-pressure plasmas? *Journal of applied physics*, 85(4):2085–2092, 1999.

[26] L Mangolini and U Kortshagen. Selective nanoparticle heating: another form of nonequilibrium in dusty plasmas. *Physical Review E*, 79(2):026405, 2009.

[27] NJ Kramer, RJ Anthony, Meenakshi Mamunuru, ES Aydil, and UR Kortshagen. Plasma-induced crystallization of silicon nanoparticles. *Journal of Physics D: Applied Physics*, 47(7):075202, 2014.

[28] D Mariotti and RM Sankaran. Perspectives on atmospheric-pressure plasmas for nanofabrication. *Journal of Physics D: Applied Physics*, 44(17):174023, 2011.

[29] RM Sankaran, D Holunga, RC Flagan, and KP Giapis. Synthesis of blue luminescent si nanoparticles using atmospheric-pressure microdischarges. *Nano letters*, 5(3):537–541, 2005.

[30] D Smith and MKS Instruments. Using coupling variables to solve compressible flow, multiphase flow and plasma processing problems. In *COMSOL Users Conference*, 2006.

[31] M Schnick, M Fussel, and J Zscetzsche. Simulation of plasma and shielding gas flows in welding and cutting arcs with ansys cfx. In *International Scientific Colloquium, Modeling for Material Processing, June*, pages 8–9, 2006.

[32] J Van Dijk, K Peerenboom, M Jimenez, D Mihailova, and J Van der Mullen. The plasma modelling toolkit plasimo. *Journal of Physics D: Applied Physics*, 42(19):194012, 2009.

[33] NY Babaeva and MJ Kushner. Structure of positive streamers inside gaseous bubbles immersed in liquids. *Journal of Physics D: Applied Physics*, 42(13):132003, 2009.

[34] S Plimpton, P Crozier, and A Thompson. Lammps-large-scale atomic/molecular massively parallel simulator. *Sandia National Laboratories*, 18, 2007.

[35] AH Markosyan, A Luque, FJ Gordillo-Vázquez, and U Ebert. Pumpkin: A tool to find principal pathways in plasma chemical models. *Computer Physics Communications*, 185(10):2697–2702, 2014.

[36] RJ Kee, FM Rupley, and JA Miller. Chemkin-ii: A fortran chemical kinetics package for the analysis of gas-phase chemical kinetics. Technical report, Sandia National Labs., Livermore, CA (USA), 1989.

[37] S Pancheshnyi, B Eismann, G Hagelaar, and L Pitchford. Zdplaskin: a new tool for plasmachemical simulations. *Bulletin of the American Physical Society*, 53, 2008.

[38] WL Morgan and BM Penetrante. Elendif: A time-dependent boltzmann solver for partially ionized plasmas. *Computer Physics Communications*, 58(1):127–152, 1990.

[39] Minnesota supercomputing institute. `https://www.msi.umn.edu`.

[40] L Dagum and R Enon. Openmp: an industry standard api for shared-memory programming. *Computational Science & Engineering, IEEE*, 5(1):46–55, 1998.

[41] W Gropp, E Lusk, N Doss, and A Skjellum. A high-performance, portable implementation of the mpi message passing interface standard. *Parallel computing*, 22(6):789–828, 1996.

[42] L Boufendi and A Bouchoule. Particle nucleation and growth in a low-pressure argon-silane discharge. *Plasma Sources Science and Technology*, 3(3):262, 1994.

[43] MT Swihart and SL Girshick. Thermochemistry and kinetics of silicon hydride cluster formation during thermal decomposition of silane. *The Journal of Physical Chemistry B*, 103(1):64–76, 1999.

[44] UV Bhandarkar, MT Swihart, SL Girshick, and UR Kortshagen. Modelling of silicon hydride clustering in a low-pressure silane plasma. *Journal of Physics D: Applied Physics*, 33(21):2731, 2000.

[45] JL Bao, P Seal, and DG Truhlar. Nanodusty plasma chemistry: a mechanistic and variational transition state theory study of the initial steps of silyl anion–silane and silylene anion–silane polymerization reactions. *Physical Chemistry Chemical Physics*, 17(24):15928–15935, 2015.

[46] T Matsoukas and M Russell. Particle charging in low-pressure plasmas. *Journal of applied physics*, 77(9):4285–4292, 1995.

[47] K De Bleecker, A Bogaerts, and W Goedheer. Modelling of nanoparticle coagulation and transport dynamics in dusty silane discharges. *New Journal of Physics*, 8(9):178, 2006.

[48] P Agarwal. *Numerical modeling of plasmas in which nanoparticles nucleate and grow*. PhD thesis, University of Minnesota, 2012.

[49] L Mangolini, E Thimsen, and U Kortshagen. High-yield plasma synthesis of luminescent silicon nanocrystals. *Nano letters*, 5(4):655–659, 2005.

[50] S Pancheshnyi, S Biagi, MC Bordage, GJM Hagelaar, WL Morgan, AV Phelps, and LC Pitchford. The lxcat project: Electron scattering cross sections and swarm parameters for low temperature plasma modeling. *Chemical Physics*, 398:148–153, 2012.

[51] JP Boeuf and E Marode. A monte carlo analysis of an electron swarm in a nonuniform field: the cathode region of a glow discharge in helium. *Journal of Physics D: Applied Physics*, 15(11):2169, 1982.

[52] GJM Hagelaar and LC Pitchford. Solving the boltzmann equation to obtain electron transport coefficients and rate coefficients for fluid models. *Plasma Sources Science and Technology*, 14(4):722, 2005.

[53] U Kortshagen, C Busch, and LD Tsendin. On simplifying approaches to the solution of the boltzmann equation in spatially inhomogeneous plasmas. *Plasma Sources Science and Technology*, 5(1):1, 1996.

[54] I Denysenko, MY Yu, and S Xu. Effect of plasma nonuniformity on electron energy distribution in a dusty plasma. *Journal of Physics D: Applied Physics*, 38(3):403, 2005.

[55] PM Bellan. *Fundamentals of plasma physics*. Cambridge University Press, 2008.

[56] S Dujko, AH Markosyan, RD White, and U Ebert. High-order fluid model for streamer discharges: I. derivation of model and transport data. *Journal of Physics D: Applied Physics*, 46(47):475202, 2013.

[57] ER Whitby and PH McMurry. Modal aerosol dynamics modeling. *Aerosol Science and Technology*, 27(6):673–688, 1997.

[58] M Frenklach and SJ Harris. Aerosol dynamics modeling using the method of moments. *Journal of colloid and interface science*, 118(1):252–261, 1987.

[59] F Gelbard, Y Tambour, and JH Seinfeld. Sectional representations for simulating aerosol dynamics. *Journal of Colloid and Interface Science*, 76(2):541–556, 1980.

[60] VI Vishnyakov, SA Kiro, MV Oprya, and AA Ennan. Coagulation of charged particles in self-organizing thermal plasmas of welding fumes. *Journal of Aerosol Science*, 76:138–147, 2014.

[61] V Colombo, E Ghedini, M Gherardi, and P Sanibondi. Modelling for the optimization of the reaction chamber in silicon nanoparticle synthesis by a radio-frequency

induction thermal plasma. *Plasma Sources Science and Technology*, 21(5):055007, 2012.

[62] M Boselli, V Colombo, E Ghedini, M Gherardi, and P Sanibondi. Two-dimensional time-dependent modelling of fume formation in a pulsed gas metal arc welding process. *Journal of Physics D: Applied Physics*, 46(22):224006, 2013.

[63] SS Talukdar and MT Swihart. Aerosol dynamics modeling of silicon nanoparticle formation during silane pyrolysis: a comparison of three solution methods. *Journal of Aerosol Science*, 35(7):889–908, 2004.

[64] SK Friedlander. Smoke, dust and haze: Fundamentals of aerosol behavior. *New York, Wiley-Interscience, 1977. 333 p.*, 1, 1977.

[65] DD Huang, JH Seinfeld, and K Okuyama. Image potential between a charged particle and an uncharged particle in aerosol coagulationenhancement in all size regimes and interplay with van der waals forces. *Journal of colloid and interface science*, 141(1):191–198, 1991.

[66] DR Warren and JH Seinfeld. Simulation of aerosol size distribution evolution in systems with simultaneous nucleation, condensation, and coagulation. *Aerosol science and technology*, 4(1):31–43, 1985.

[67] JC Weingartner and BT Draine. Photoelectric emission from interstellar dust: Grain charging and gas heating. *The Astrophysical Journal Supplement Series*, 134(2):263, 2001.

[68] J Goree. Ion trapping by a charged dust grain in a plasma. *Physical review letters*, 69(2):277, 1992.

[69] VW Chow, DA Mendis, and M Rosenberg. Secondary emission from small dust grains at high electron energies. *Plasma Science, IEEE Transactions on*, 22(2):179–186, 1994.

[70] R Le Picard and SL Girshick. The effect of single-particle charge limits on charge distributions in dusty plasmas. *Journal of Physics D: Applied Physics*, 49(9):095201, 2016.

[71] C Cui and J Goree. Fluctuations of the charge on a dust grain in a plasma. *Plasma Science, IEEE Transactions on*, 22(2):151–158, 1994.

[72] R Le Picard, AH Markosyan, DH Porter, SL Girshick, and MJ Kushner. Synthesis of silicon nanoparticles in nonthermal capacitively-coupled flowing plasmas: Processes and transport. *Plasma Chemistry and Plasma Processing*, 36(4):941–972, 2016.

[73] D Moore, S Krishnamurthy, Y Chao, Q Wang, D Brabazon, and PJ McNally. Characteristics of silicon nanocrystals for photovoltaic applications. *physica status solidi (a)*, 208(3):604–607, 2011.

[74] S Weis, R Körmer, MPM Jank, M Lemberger, M Otto, H Ryssel, W Peukert, and L Frey. Conduction mechanisms and environmental sensitivity of solution-processed silicon nanoparticle layers for thin-film transistors. *Small*, 7(20):2853–2857, 2011.

[75] K Fujioka, M Hiruoka, K Sato, N Manabe, R Miyasaka, S Hanada, A Hoshino, RD Tilley, Y Manome, K Hirakuri, and K Yamamoto. Luminescent passive-oxidized silicon quantum dots as biological staining labels and their cytotoxicity effects at high concentration. *Nanotechnology*, 19(41):415102, 2008.

[76] N Shirahata. Colloidal si nanocrystals: a controlled organic–inorganic interface and its implications of color-tuning and chemical design toward sophisticated architectures. *Physical Chemistry Chemical Physics*, 13(16):7284–7294, 2011.

[77] I Doğan and M van de Sanden. Gas-phase plasma synthesis of free-standing silicon nanoparticles for future energy applications. *Plasma Processes and Polymers*, 2015.

[78] U Kortshagen. Nonthermal plasma synthesis of semiconductor nanocrystals. *Journal of Physics D: Applied Physics*, 42(11):113001, 2009.

[79] T Lopez and L Mangolini. On the nucleation and crystallization of nanoparticles in continuous-flow nonthermal plasma reactors. *Journal of Vacuum Science & Technology B*, 32(6):061802, 2014.

[80] M Hirasawa, T Orii, and T Seto. Size-dependent crystallization of si nanoparticles. *Applied physics letters*, 88(9):093119, 2006.

[81] L Boufendi, A Bouchoule, and T Hbid. Electrical characterization and modeling of a dust forming plasma in a radio frequency discharge. *Journal of Vacuum Science & Technology A*, 14(2):572–576, 1996.

[82] N Bilik, R Anthony, BA Merritt, ES Aydil, and UR Kortshagen. Langmuir probe measurements of electron energy probability functions in dusty plasmas. *Journal of Physics D: Applied Physics*, 48(10):105204, 2015.

[83] U Bhandarkar, U Kortshagen, and SL Girshick. Numerical study of the effect of gas temperature on the time for onset of particle nucleation in argon–silane low-pressure plasmas. *Journal of Physics D: Applied Physics*, 36(12):1399, 2003.

[84] R Gresback, Z Holman, and U Kortshagen. Nonthermal plasma synthesis of size-controlled, monodisperse, freestanding germanium nanocrystals. *Applied Physics Letters*, 91(9):093119, 2007.

[85] J Perrin, O Leroy, and MC Bordage. Cross-sections, rate constants and transport coefficients in silane plasma chemistry. *Contributions to Plasma Physics*, 36(1):3–49, 1996.

[86] P Ho, WG Breiland, and RJ Buss. Laser studies of the reactivity of sih with the surface of a depositing film. *The Journal of chemical physics*, 91(4):2627–2634, 1989.

[87] T Hawa and MR Zachariah. Coalescence kinetics of unequal sized nanoparticles. *Journal of Aerosol Science*, 37(1):1–15, 2006.

[88] DZ Wang and JQ Dong. Kinetics of low pressure rf discharges with dust particles. *Journal of applied physics*, 81(1):38–42, 1997.

[89] AA Fridman, L Boufendi, T Hbid, BV Potapkin, and A Bouchoule. Dusty plasma formation: Physics and critical phenomena. theoretical approach. *Journal of Applied Physics*, 79(3):1303–1314, 1996.

[90] P Seal and DG Truhlar. Large entropic effects on the thermochemistry of silicon nanodusty plasma constituents. *Journal of the American Chemical Society*, 136(7):2786–2799, 2014.

[91] H Tawara, Y Itikawa, H Nishimura, and Masatoshi Yoshino. Cross sections and related data for electron collisions with hydrogen molecules and molecular ions. *Journal of Physical and Chemical Reference Data*, 19(3):617–636, 1990.

[92] HR Maurer and H Kersten. On the heating of nano-and microparticles in process plasmas. *Journal of Physics D: Applied Physics*, 44(17):174029, 2011.

[93] RK Endo, Y Fujihara, and M Susa. Calculation of density and heat capacity of silicon by molecular dynamics simulation. *High Temp High Press*, 35(36):505–511, 2003.

[94] T Matsoukas and M Russell. Fokker-planck description of particle charging in ionized gases. *Physical Review E*, 55(1):991, 1997.

[95] B Shotorban. Nonstationary stochastic charge fluctuations of a dust particle in plasmas. *Physical Review E*, 83(6):066403, 2011.

[96] SA Khrapak, AP Nefedov, OF Petrov, and OS Vaulina. Dynamical properties of random charge fluctuations in a dusty plasma with different charging mechanisms. *Physical Review E*, 59(5):6017, 1999.

[97] BF Gordiets and CM Ferreira. Charge distribution function of plasma dust particles with secondary electron emission. *Journal of applied physics*, 86:4118–4123, 1999.

[98] BT Draine and B Sutin. Collisional charging of interstellar grains. *The Astrophysical Journal*, 320:803–817, 1987.

[99] L Rayleigh. Xx. on the equilibrium of liquid conducting masses charged with electricity. *The London, Edinburgh, and Dublin Philosophical Magazine and Journal of Science*, 14(87):184–186, 1882.

[100] A Doyle, DR Moffett, and B Vonnegut. Behavior of evaporating electrically charged droplets. *Journal of Colloid Science*, 19(2):136–143, 1964.

[101] R Gomer. *Field emission and field ionization*, volume 34. Harvard University Press Cambridge, MA, 1961.

[102] A Bouchoule and L Boufendi. Particulate formation and dusty plasma behaviour in argon-silane rf discharge. *Plasma Sources Science and Technology*, 2(3):204, 1993.

[103] EC Whipple, TG Northrop, and DA Mendis. The electrostatics of a dusty plasma. *Journal of Geophysical Research: Space Physics*, 90(A8):7405–7413, 1985.

[104] A Grill. *Cold plasma in materials fabrication*, volume 151. IEEE Press, New York, 1994.

[105] GS Selwyn. Plasma particulate contamination control. i. transport and process effects. *Journal of Vacuum Science & Technology B*, 9(6):3487–3492, 1991.

[106] E Stoffels, WW Stoffels, D Vender, M Kando, GMW Kroesen, and FJ De Hoog. Negative ions in a radio-frequency oxygen plasma. *Physical Review E*, 51(3):2425, 1995.

[107] SA Khrapak, Svetlana V Ratynskaia, AV Zobnin, AD Usachev, VV Yaroshenko, MH Thoma, M Kretschmer, H Höfner, GE Morfill, OF Petrov, et al. Particle charge in the bulk of gas discharges. *Physical Review E*, 72(1):016406, 2005.

[108] CK Goertz. Dusty plasmas in the solar system. *Reviews of Geophysics*, 27(2):271–292, 1989.

[109] VI Vishnyakov, GS Dragan, and AV Florko. The formation of negatively charged particles in thermoemission plasmas. *Journal of Experimental and Theoretical Physics*, 106(1):182–186, 2008.

[110] AD Richards, BE Thompson, KD Allen, and HH Sawin. Atomic chlorine concentration measurements in a plasma etching reactor. i. a comparison of infrared absorption and optical emission actinometry. *Journal of applied physics*, 62(3):792–798, 1987.

[111] MA Lieberman and AJ Lichtenberg. *Principles of plasma discharges and materials processing.* John Wiley & Sons, 2005.

[112] J Goree. Charging of particles in a plasma. *Plasma Sources Science and Technology*, 3(3):400, 1994.

[113] H Sugai, K Nakamura, Y Hikosaka, and M Nakamura. Diagnostics and control of radicals in an inductively coupled etching reactor. *Journal of Vacuum Science & Technology A*, 13(3):887–893, 1995.

[114] P Jiang, DJ Economou, and CB Shin. Effect of power modulation on radical concentration and uniformity in a single-wafer plasma reactor. *Plasma Chemistry and Plasma Processing*, 15(3):383–396, 1995.

[115] A Bouchoule, A Plain, L Boufendi, JP Blondeau, and C Laure. Particle generation and behavior in a silane-argon low-pressure discharge under continuous or pulsed radio-frequency excitation. *Journal of applied physics*, 70(4), 1991.

[116] P Subramonium and MJ Kushner. Two-dimensional modeling of long-term transients in inductively coupled plasmas using moderate computational parallelism. i. ar pulsed plasmas. *Journal of Vacuum Science & Technology A*, 20(2):313–324, 2002.

[117] B Ramamurthi and DJ Economou. Pulsed-power plasma reactors: two-dimensional electropositive discharge simulation in a gec reference cell. *Plasma Sources Science and Technology*, 11(3):324, 2002.

[118] J Berndt, E Kovačević, V Selenin, I Stefanović, and J Winter. Anomalous behaviour of the electron density in a pulsed complex plasma. *Plasma Sources Science and Technology*, 15(1):18, 2005.

[119] IV Schweigert and AL Alexandrov. Effect of nanoparticles on an rf discharge afterglow. *Journal of Physics D: Applied Physics*, 45(32):325201, 2012.

[120] L Pavesi and R Turan. *Silicon nanocrystals: fundamentals, synthesis and applications.* John Wiley & Sons, 2010.

[121] K Kim, JH Park, SG Doo, JD Nam, and T Kim. Generation of size and structure controlled si nanoparticles using pulse plasma for energy devices. *Thin Solid Films*, 517(14):4184–4187, 2009.

[122] PR i Cabarrocas, R Cariou, and M Labrune. Low temperature plasma deposition of silicon thin films: From amorphous to crystalline. *Journal of Non-Crystalline Solids*, 358(17):2000–2003, 2012.

[123] H Haberland, Z Insepov, and M Moseler. Molecular-dynamics simulation of thin-film growth by energetic cluster impact. *Physical Review B*, 51(16):11061, 1995.

[124] HP Cheng and U Landman. Controlled deposition and classification of copper nanoclusters. *The Journal of Physical Chemistry*, 98(13):3527–3537, 1994.

[125] AD Richards, BE Thompson, and HH Sawin. Continuum modeling of argon radio frequency glow discharges. *Applied physics letters*, 50(9):492–494, 1987.

[126] MS Barnes, JH Keller, JC Forster, JA ONeill, and DK Coultas. Transport of dust particles in glow-discharge plasmas. *Physical review letters*, 68(3):313, 1992.

[127] JA Bittencourt. *Fundamentals of plasma physics*. Springer Science & Business Media, 2013.

[128] B Kalache, T Novikova, AF i Morral, PR i Cabarrocas, W Morscheidt, and K Hassouni. Investigation of coupling between chemistry and discharge dynamics in radio frequency hydrogen plasmas in the torr regime. *Journal of Physics D: Applied Physics*, 37(13):1765, 2004.

[129] K De Bleecker, A Bogaerts, R Gijbels, and W Goedheer. Numerical investigation of particle formation mechanisms in silane discharges. *Physical Review E*, 69(5):056409, 2004.

[130] AT Hjartarson, EG Thorsteinsson, and JT Gudmundsson. Low pressure hydrogen discharges diluted with argon explored using a global model. *Plasma Sources Science and Technology*, 19(6):065008, 2010.

[131] I Méndez, FJ Gordillo-Vázquez, VJ Herrero, and I Tanarro. Atom and ion chemistry in low pressure hydrogen dc plasmas. *The Journal of Physical Chemistry A*, 110(18):6060–6066, 2006.

[132] E Meeks, RS Larson, P Ho, C Apblett, SM Han, E Edelberg, and ES Aydil. Modeling of sio2 deposition in high density plasma reactors and comparisons of

model predictions with experimental measurements. *Journal of Vacuum Science & Technology A*, 16(2):544–563, 1998.

[133] K de Bleecker. *Modeling of the formation and behavior of nanoparticles in dusty plasmas*. PhD thesis, Universiteit Antwerpen, Faculteit Wetenschappen, Departement Scheikunde, 2006.

[134] T Novikova, B Kalache, P Bulkin, K Hassouni, W Morscheidt, and PR i Cabarrocas. Numerical modeling of capacitively coupled hydrogen plasmas: Effects of frequency and pressure. *Journal of applied physics*, 93(6):3198–3206, 2003.

[135] S Ashida and MA Lieberman. Spatially averaged (global) model of time modulated high density chlorine plasmas. *Japanese journal of applied physics*, 36(2R):854, 1997.

[136] SL Girshick, C-P Chiu, R Muno, CY Wu, Li Yang, SK Singh, and PH McMurry. Thermal plasma synthesis of ultrafine iron particles. *Journal of aerosol science*, 24(3):367–382, 1993.

[137] L Schwaederlé, P Brault, C Rond, and A Gicquel. Molecular dynamics calculations of ch3 sticking coefficient onto diamond surfaces. *Plasma Processes and Polymers*, 12(8):764–770, 2015.

Appendix A

List of Integrals

All integrations needed in the derivation of particle charge distributions accounting for charge limits are calculated using the following integrals:

$$I_1 = \int \exp\Big[-\frac{(x-\bar{x})^2}{a}\Big]dx, \tag{A.1}$$

$$I_2 = \int x\exp\Big[-\frac{(x-\bar{x})^2}{a}\Big]dx, \tag{A.2}$$

$$I_3 = \int (x-b)^2\exp\Big[-\frac{(x-\bar{x})^2}{a}\Big]dx. \tag{A.3}$$

The values of these integrals are as follows:

$$I_1 = \frac{1}{2}(\pi a)^{1/2}\mathrm{erf}\Big(\frac{x-\bar{x}}{a^{1/2}}\Big) + C, \tag{A.4}$$

$$I_2 = I_1\bar{x} - \frac{1}{2}a\exp\Big[-\frac{(x-\bar{x})^2}{a}\Big] + C, \tag{A.5}$$

$$I_3 = I_1\Big[\frac{a+2(\bar{x}-b)^2}{2}\Big] - \frac{1}{2}a\exp\Big[-\frac{(x-\bar{x})^2}{a}\Big](\bar{x}-2b+x) + C, \tag{A.6}$$

where C is the constant of integration.